Title

Tunable Broad Light Emission from 3D âHollowâ Bromide Perovskites through Defect Engineering

Journal

Journal of the American Chemical Society, 143(18)

ISSN

0002-7863 1520-5126

Authors

Spanopoulos, Ioannis
Hadar, Ido
Ke, Weijun
et al.

Publication Date

2021-04-27

DOI

10.1021/jacs.1c01727

Peer reviewed

Tunable Broad Light Emission from 3D "Hollow" Bromide Perovskites through Defect Engineering

Ioannis Spanopoulos[1], Ido Hadar[1&], Weijun Ke[1§], Peijun Guo[2#], Eve M. Mozur,[3] Emily Morgan,[3] Shuxin Wang,[3] Ding Zheng,[1] Suyog Padgaonkar,[4] G. N. Manjunatha Reddy,[5] Emily A. Weiss,[4] Mark C. Hersam,[6] Ram Seshadri,[3] Richard D. Schaller[1], and Mercouri G. Kanatzidis*[,1]

[1]*Department of Chemistry, Northwestern University, Evanston, Illinois 60208, United States*
[2]*Center for Nanoscale Materials, Argonne National Laboratory, 9700 South Cass Avenue, Lemont, Illinois 60439, United States*
[3]*Materials Department and Materials Research Laboratory, University of California, Santa Barbara, California 93106, United States*
[4]*Department of Chemistry and the Materials Research Center, Applied Physics Program, and Department of Materials Science and Engineering and the Materials Research Center, Northwestern University, Evanston, Illinois 60208, United States*
[5]*Univ. Lille, CNRS, Centrale Lille Institut, Univ. Artois, UMR8181-UCCS-Unité de Catalyse et Chimie du Solide, F-59000 Lille, France.*
[6]*Department of Materials Science and Engineering, Department of Chemistry, Department of Electrical and Computer Engineering, and the Materials Research Center, Northwestern University, Evanston, Illinois 60208, United States*

ABSTRACT

Hybrid halide perovskites consisting of corner-sharing metal halide octahedra and small cuboctahedral cages filled with counter cations have proven to be prominent candidates for many high-performance optoelectronic devices. The stability limits of their three-dimensional perovskite framework are defined by the size range of the cations present in the cages of the structure. In some cases, the stability of the perovskite-type structure can be extended even when the counter ions violate the size and shape requirements, as is the case in the so-called "hollow" perovskites. In this work, we engineered a new family of 3D highly defective yet crystalline "hollow" bromide perovskites with general formula $(FA)_{1-x}(en)_x(Pb)_{1-0.7x}(Br)_{3-0.4x}$ (FA = formamidinium (FA^+), *en* = ethylenediammonium (en^{2+}), x = 0-0.44). Pair distribution function analysis shed light on the local structural coherence, revealing a wide distribution of Pb-Pb distances in the crystal structure as a consequence of the Pb/Br-deficient nature and *en* inclusion in the lattice. By manipulating the number of Pb/Br vacancies, we finely tune the optical properties of the pristine $FAPbBr_3$, by blue shifting the band gap from 2.20 eV to 2.60 eV for the 0.42 *en* sample. A most unexpected outcome was that at x> 0.33 *en* incorporation the material exhibits strong broad light

emission (1% PLQY) that is maintained after exposure to air for more than a year. This is the first example of strong broad light emission from a 3D hybrid halide perovskite, demonstrating that meticulous defect engineering is an excellent tool for customizing the optical properties of these semiconductors.

INTRODUCTION

Halide perovskites have the potential to be next-generation semiconductors[1-3] with exquisitely tunable optoelectronic properties[4-5] directly derived from their unique structural configuration and chemical versatility.[6-7] Currently, the most investigated 3D perovskite materials have the general formula AMX_3 (A = $CH_3NH_3^+$ (MA), $HC(NH_2)_2^+$ (FA), Cs^+; M = Ge^{2+}, Sn^{2+}, Pb^{2+}; X = Cl^-, Br^-, I^-).[8,9] The aristotype 3D perovskite structure consists of MX_6 corner sharing metal halide octahedra that span to three orthogonal directions, while A^+ cations reside in the formed cuboctahedral cavities charge balancing the structure.[10] Among the attractive features of this perovskite family are solution processability,[11] long carrier lifetimes[12] and diffusion lengths,[13-14] as well promising high tolerance for radiation damage.[15-17] Interestingly, many of these traits derive from the defect tolerant character of these materials.[18-21] Apparently, the majority of formed point defects are shallow, close to the band edges and do not act as significant traps for generated carriers.[22-23]

Defect engineering in perovskites could add extra handles in tailoring their optoelectronic properties and long-term environmental stability.[24] High defect content crystals have been recently reported such as the d-MAPI class of materials with general formula $(A)_{1-2.48x}(B)_{3.48x}[M_{1-x}I_{3-x}]$ (A = MA, FA; B = hydroxyethylammonium (HEA^+), thioethylammonium (TEA^+), 1,2,4-triazolium (TzH^+); M = Pb^{2+}, Sn^{2+})[25-28] and the "hollow" halide perovskites with general formula $(A)_{1-x}(B)_x(M)_{1-0.7x}(I)_{3-0.4x}$ (A = MA, FA; B = ethylenediammonium (*en*), propylenediammonium (PN) and trimethylenediammonium (TN); M = Pb^{2+}, Sn^{2+}).[29-32] In both of these families, the introduction of A site cations longer than MA and FA, such as *en*, HEA, and TEA, cause the removal of metal halide moieties from the crystal lattice generating vacancy defects in the 3D framework. In the case of d-MAPI materials, the structure consists of a 3D corner sharing perovskite $Pb_{1-x}I_{3-x}$ (x = 0 to 0.20) with a lead-deficient and iodide-deficient 3D network of periodically localized defects. In contrast, in the case of "hollow" perovskites, the lead and iodide defects are randomly dispersed in the crystal structure, preserving the archetypal cubic 3D perovskite network.

A striking attribute of these defective materials is the systematic alteration of optical properties (in terms of absorption and emission spectra) by changing the number of defects in the crystal structure. For example, in the "hollow" $(MA)_{1-x}(en)_x(Pb)_{1-0.7x}(I)_{3-0.4x}$ compounds, the bandgap can be adjusted from 1.52 eV for pristine $MAPbI_3$ (x = 0) to 2.1 eV for the $(MA)_{0.56}(en)_{0.44}(Pb)_{0.692}(I)_{2.824}$ (x = 0.44) analog. Additional prominent characteristics involve their exceptional environmental stability and the stabilization of the high symmetry cubic α perovskite phase ($SrTiO_3$)[33-34] at RT. For instance, the $(MA)_{1-x}(en)_x(Sn)_{1-0.7x}(I)_{3-0.4x}$ family of perovskites (in single crystal form) is stable to chemical degradation for 16 days in air (for the 40% *en* based sample), while pristine $MASnI_3$ (x = 0) degrades within ten minutes. The Pb "hollow" analogs are stable for nearly a year compared to hours and weeks for pristine α-$FAPbI_3$ and β-$MAPbI_3$ respectively.[30] The excellent air stability of the "hollow" perovskites may be ascribed to suppressed ion migration, by the presence of a large amount of *en* dications in the lattice. This is supported by our recent work, examining the electronic and ionic conductivity in the "hollow" $MAPbI_3$ system. The suppression of ion migration is reflected by the significant increase of the activation energies for iodide ion migration with higher *en* content derived from both experimental data and *ab initio* simulations.[35]

Intrigued by the notable environmental stability and optoelectronic properties of the "hollow" iodide perovskites, we investigated whether the Pb bromide compounds could also form "hollow" structures. Given the smaller size of the 3D cage in the bromine analogs compared to the iodine analogs, we wanted to determine if such structures can form at all and how they would compare to the iodides. Here, we report a new family of defective materials with general formula $(FA)_{1-x}(en)_x(Pb)_{1-0.7x}(Br)_{3-0.4x}$ (FA = formamidinium, *en* = ethylenediammonium, x = 0-0.44). This is the first demonstration of engineering bromide perovskites with tunable defects in single crystal form, whereas recently Worku *et al*. reported "hollow" $CsPbBr_3$ nanoparticles[36] and Yakunin *et al*. demonstrated the synthesis of "hollow" $FAPbBr_3$ nanoparticles.[37] Using single crystal X-ray diffraction and PDF analysis, we demonstrate that the defective nature of the materials originates from the replacement of Pb and Br atoms by *en* dications. In particular, we employed solid state NMR spectroscopy to shed light on the local structural environment of *en* molecules; these studies revealed the presence of two types of defects in the crystal lattice. The optical properties can be fine-tuned by controlling the degree of *en* molecule incorporation. Usually structural defects act as non-radiative recombination centers (traps) and quench PL emission.[38] Surprisingly, we

observed that, above 33% *en* inclusion, a strong broad emission band centered at 590 nm emerges that is tunable in intensity by controlling the content of *en* in the lattice. Although broad light emission is common for low-dimensional perovskites and metal halides,[39-41] the strong and broad emission of the "hollow" bromide compounds is unique among 3D hybrid halide perovskites.[42-44]

RESULTS AND DISCUSSION

Synthetic aspects and structural characterization

High quality single crystals of $(FA)_{1-x}(en)_x(Pb)_{1-0.7x}(Br)_{3-0.4x}$ (x = 0, 0.07, 0.18, 0.29, 0.33, 0.37, 0.40, 0.42, 0.44) were synthesized by dissolving lead (II) acetate, formamidinium acetate, and various amounts of ethylenediamine (maximum nominal ratio of *en*:FA:Pb: = 1.1:1:1) in a hot acidic H_3PO_2/HBr solvent mixture (Figure S1). Due to the excess of A site cations present in the solution at *en*:Pb ratios (0.5-1.1:1), the corresponding crystals must be isolated from the mother solution shortly after formation to avoid the coprecipitation of the non-perovskite phase $(en)_2PbBr_6$ upon cooling. The existence of $(en)_2PbBr_6$ was confirmed by single crystal X-ray diffraction (XRD) analysis (Tables S1-5). The structure was reported previously by Lemmerer *et al.* and consists of 1D ribbons of corner-sharing $[PbBr_6]^{4-}$ octahedra separated by ethylenediammonium cations and free bromide anions, that charge balance the structure (more precisely $[(H_3NC_2H_4NH_3)_4Pb_2Br_9 \cdot 3Br]$).[45]

Powder X-ray diffraction (PXRD) measurements verified the phase purity of the as-synthesized single crystals, and confirmed that they are all isostructural to the pristine cubic α-$FAPbBr_3$ (Figures 1, S2-3). Notably, with increasing amount of *en* in the structure, there is a gradual unit cell expansion that is clear from the shift of the PXRD patterns to lower 2θ values. The pristine and "hollow" samples (0, 0.18, 0.29, 0.42 content of *en*) crystallize in the same cubic *Pm*-3*m* space group (Table 1). Apparently, even at high *en* loading (44%), the structure retains its 3D nature (Figure S4). All structures were solved and refined using single crystal XRD measurements. However, *en* cations could not be crystallographically resolved because of the lack of periodicity and non-uniform distribution in the crystal lattice, displacing FA^+, Pb^{2+}, and Br^- ions, thus creating a large number of randomly dispersed defects (Figure 2). The only pronounced difference among the solved crystal structures is the elongation of the Pb-Br bonds, from 2.9963(3) Å to 3.0320(10) Å giving rise to a unit cell volume

expansion from 215.202(19) $Å^3$ to 222.986(6) $Å^3$ for the pristine and 42% *en* sample, respectively (Figure 3 and Tables 2, S6-S21). Imposed by the cubic *Pm*-3*m* space group symmetry, all Pb-Br-Pb angles are 180 deg.

Occupancy refinement of the Pb and Br atom sites revealed that by increasing the content of *en* in the structure, there is a rising number of Pb and Br atom vacancies, which is significantly more pronounced for the heavy Pb atoms (up to 20% for 42% *en* loading) (Table S22). This was further supported by energy dispersive spectroscopy (EDS) measurements where for the 42% *en* sample the ratio of Pb:Br is 1:3.9 instead of 1:3 (Figure S5). Thermogravimetric (TGA) analysis corroborates the above results. By increasing the amount of incorporated *en*, there is a gradual weight loss increase in the first step of the graph, which corresponds to FABr and *en*Br_2 loss at around 300 °C. This weight loss ranges from 25.1% to 36.2% for the pristine and 42% *en* based materials, respectively (Figures S6-S9). At the same time, the mass loss at the second step at around 430 °C corresponds to the removal of the $PbBr_2$ inorganic part, which decreases gradually from 73.4% to 60.5% for the pristine and 42% *en* based materials, respectively. These results confirm the reduction in the amount of Pb with increasing amount of *en* in the structure (Table S23).

Solution ^{1}H-NMR spectroscopy measurements verified the presence of *en* in the crystal structure and the ratio among *en* and FA cations (Figures S10-17). The quantification was based on both the methine (=CH-, δ = 7.87 ppm) and the ammonium (-NH_2^+, δ = 8.69 ppm, 9.03 ppm) protons of the FA cation versus the methylene (-CH_2-, δ = 3.07 ppm) and the ammonium (-NH_3^+, δ = 7.89 ppm) protons of the *en* cations. In FA, the integration of those peaks reveals a ratio of 2:2:1, since there is one proton from the methine group (=CH-) and four protons from the two amine cations (-NH_2^+). In *en*, the ratio of the two peaks is 4:6, arising from four -CH_2- protons and six ammonium (-NH_3^+) protons, suggesting that *en* is doubly protonated.

Experimental crystal densities determined from a commercially available pycnometer indicated that the density of the samples decreases proportionally to *en* incorporation in the structure from 3.8116(2) $cm^3\ g^{-1}$ to 3.4657(2) $cm^3\ g^{-1}$ for the pristine and 42% *en* sample accordingly (Table S24). This trend is further supported by the observed expansion of the unit cell dimensions with increasing *en* content, coupled with reduced site occupancies of the heavy atoms that further lowers crystal density.

Considering the disordered nature of the corresponding "hollow" materials, which do not allow direct structure determination as in the case of ordered defective d-$MAPbI_3$ analogs,[26] an indirect method was designed for the assembly of a representative chemical formula that can describe the hollow compounds. In order to examine whether the formula of the hollow iodide samples $(A)_{1-x}(en)_x(M)_{1-0.7x}(I)_{3-0.4x}$, can be applied in the bromide analogs as well, we followed a previously established analysis protocol,[30] combining the data from four different characterization techniques, ^{1}H-NMR, PXRD, XRD, and crystal density measurements. In particular, we compared the theoretical crystal density derived from the examined formula with the experimental crystal density obtained from single-crystal XRD and pycnometry measurements (Table S24). The determined (experimental) crystal density from the single crystal XRD studies is very close to the calculated ones based on PXRD and ^{1}H-NMR studies (0.4-4% difference in crystal density values). The derived values from the pycnometry studies showed somewhat higher variation than the theoretical ones in the range from 0.07% for the pristine material to 8% for the 42% *en* sample. In addition, EDS measurements for the highly hollow sample, $(FA)_{0.58}(en)_{0.42}(Pb)_{0.706}(Br)_{2.832}$ gave a Pb:Br ratio of 1:3.9 which is close to the 1:4 ratio deriving from the formula. Based on these results, we propose the formula $(FA)_{1-x}(en)_x(Pb)_{1-0.7x}(Br)_{3-0.4x}$ to describe the chemical composition of the "hollow" bromide analogs as well. For simplicity purposes the notation % *en*/$FAPbBr_3$ will be used throughout this work.

Notably, the unit cell volume expansion, the reduction in the crystal density and the blue shift of the absorption and emission spectra (see below) proportionally to *en* inclusion, constitute signature characteristics of the "hollow" perovskites. Another trait of the "hollow" bromide perovskites (similar to the iodides) is the change in the crystal morphology, from rhombic dodecahedral shape for the pristine $FAPbBr_3$ to regular octahedral for the "hollow" bromide crystals, as attained from scanning electron microscopy (SEM) measurements (Figure 4) and analysis.

Structural phase transitions. A well-known characteristic of all perovskite structures is the phase transitions associated with the behaviour of the metal octahedra tilting as a function of temperature. Using high resolution variable temperature synchrotron PXRD studies, we explored the phase transitions occurring in both "hollow" iodide and bromide perovskites. We find that *en* incorporation can suppress the temperature dependent phase transitions.[46] The "hollow" bromide samples are stable in the cubic α-phase between 94 K and 493 K (Figures 5, S18). On the contrary,

pristine $FAPbBr_3$ exhibits two distinct phase transitions in this temperature range. One between 275 and 250 K, giving rise to a tetragonal *P*4/*mbm* phase, while upon further cooling, the structure distorts more giving rise to an orthorhombic *Pnma* phase between 150 and 125 K.[47] The thermal stability and robustness of the hollow perovskite structure up to 493 K is accompanied by a gradual increase of the unit cell dimensions due to thermal expansion (from 6.02082(1) Å at 94K to 6.13381(2) Å at 493K for the 42% *en* material), which is a norm for hybrid perovskites and metal halide materials.[39, 48]

The same behavior is observed for the corresponding "hollow" $MAPbI_3$ and $FAPbI_3$ samples. Both 33% *en*/$MAPbI_3$ and 40% *en*/$FAPbI_3$ crystallize at the cubic *Pm*-3*m* space group over the entire examined temperature range as the "hollow" $FAPbBr_3$ compounds (Figures S19-20). Contrarily, pristine $MAPbI_3$ crystals exhibit two phase transitions, one at ~330 K, from cubic α (*Pm*-3*m*) to tetragonal β (*I*4/*mcm*) and one at ~160 K, from tetragonal to orthorhombic (*Pnma*).[49-50] The material's temperature profile is governed by two distinct structural phase transitions, one at ~ 285 K, from cubic α (*Pm*-3*m*) to tetragonal β (*P*4/*mbm*) and one at ~ 140 K, from tetragonal β (*P*4/*mbm*) to tetragonal γ (*P*4/*mbm*).[51-52] Simenas *et al.* reported a similar trend in the case of $MA_{1-x}DMA_xPbBr_3$ single crystals and observed significant suppression of the structural phase transitions, including stabilization of the cubic phase and disorder even for a small amount of dimethylammonium cations.[53] The stabilization of a cubic high temperature phase at lower temperatures due to the presence of defects and increased structural disorder is a well-known phenomenon in metal oxides as well.[54-55]

Local structure through pair distribution function analysis. Pair distribution function (PDF) analysis was utilized to shed light on the local non-periodic crystal structure of the materials. This method is specifically adopted for the characterization of disordered compounds with limited structural coherence.[56-58] The goal was to identify significant deviations from the average crystal structure that may be present and caused by the FA/*en* disorder and Pb/Br vacancies in the lattice. The PDF data confirm the increase in unit cell volume from 216 $Å^3$ in $FAPbBr_3$ to 222 $Å^3$ in the hollow $FAPbBr_3$ samples found by the conventional XRD studies mentioned above. Qualitative comparison of the PDF for pristine $FAPbBr_3$ and 40% *en* substituted $FAPbBr_3$ (Figure 6a) demonstrates a decrease in the number of several pair correlations with *en* substitution, suggesting a smaller concentration of strong scatterers. Several pair correlations also show tailing on the high *r* side of the peak indicating an

asymmetric increase in the distribution of Pb-Br bond distances. Fitting of the PDF to the average cubic perovskite structure (*Pm*-3*m*) indicates that the reduction in intensity and tailing originates primarily from changes at the Pb site. This is most clearly observed by comparing the partial PDFs calculated for Br-Br pair correlations and Pb-Pb pair correlations (Figure 6b). The Br-Br correlations are visually quite similar between the pristine and "hollow" samples. In contrast, Pb-Pb pair correlations exhibit marked decreases in intensity and increase in peak tailing between the pristine and "hollow" perovskite similar to that observed in the total PDF. These features are accompanied by a reduction in the refined Pb site occupancy from 1.02 in pristine $FAPbBr_3$ to 0.85 for 40% *en* substituted $FAPbBr_3$, which is consistent with the results from the single crystal XRD studies. The PDF data therefore demonstrate that *en* substitution leads to decreased Pb atom occupancy, increased disorder, and increased Pb-Br bond distances.

Elucidation of short-range structures and interactions through solid-state NMR spectroscopy. Local chemical environments of *en* cations in the $FAPbBr_3$ perovskite framework are best consolidated by 1D and 2D solid-state NMR spectroscopy (ssNMR) measurements and analysis. Specially, ssNMR spectroscopy has recently been applied to characterize local structures and intermolecular interactions at sub-nm to nm length scale in optoelectronic materials.[59-62] Figure 7 compares the 1D and 2D ^1H ssNMR spectra of pristine $FAPbBr_3$ and *en* substituted $FAPbBr_3$ at different stoichiometric concentrations, whereby signals correspond to distinct ^1H sites, 4.1 (-CH_2-, *en*), ~7.5 (-NH_3^+, *en* and FA^+) and 8.1 ppm (=CH-, FA^+) are color coded as depicted in the schematic structures. Of particular interest is the broad line shape associated with the ^1H signal at ~4.1 ppm in the 1D spectra of 33% *en* and 44% *en* as compared to the narrow feature in 12% *en*, indicating that the *en* cations exhibit different local chemical environments in $FAPbBr_3$ framework. Deconvolution of ^1H NMR signals (4.1 ppm, -CH_2-) in 33% *en* and 44% *en* suggest that the *en* dispersion in $FAPbBr_3$ reaches a saturation point at ~29%, while at higher *en* loadings there is a formation of an additional type of *en* defect in the crystal structure. Apparently for 33% *en* and 41% *en* inclusion in $FAPbBr_3$, there is ~5% and ~12% aggregation of the total *en* cations giving rise to a structurally different local environment around them, as depicted by the broad signals in the corresponding ^1H NMR spectra (Figure 7a, inset). This finding may be correlated to the unit cell expansion and Pb-Br bond elongation (Figure 3) that increase

linearly with increasing *en* amount in the lattice, while above 30% *en* these effects are supressed.

The different distributions of *en* and FA^+ cations in the perovskite framework is further corroborated by the analysis of 2D ^1H-^1H double-quantum (DQ) and ^1H-^1H spin-diffusion spectra of 41% *en*/$FAPbBr_3$. The DQ signals can be excited for inter- and intramolecular dipolar coupled $^1H\cdots{}^1H$ pairs at sub-nanometer distances < 5 Å (Figure 7b): the on-diagonal DQ signals at 8.2 ppm correspond to $^1H\cdots{}^1H$ proximities in the -CH_2- groups of *en* and a broad feature at ~15 ppm corresponds to overlapped contributions from the -NH_3^+ groups in *en* and FA^+. The off-diagonal DQ signal at 11.6 ppm corresponds to $^1H\cdots{}^1H$ proximities between chemically distinct -CH_2- and -NH_3^+ groups of *en*, and at ~15.6 ppm is due to through-space proximities between =CH- and -NH_2^+ groups of FA^+. Notably, ^1H DQ peaks between =CH- groups of FA^+ and -CH_2- groups of *en* (red arrow) indicate the through-space close proximity (<0.5 nm) between =CH- (FA^+) and -CH_2- (*en*), confirming the presence of *en* cations in the perovskite framework. In addition, 2D ^1H-^1H spin-diffusion NMR spectra of 41% *en*/$FAPbBr_3$ were analyzed and compared in order to confirm the through-space proximities between the *en* and FA^+ cations. In a 2D spin-diffusion experiment, magnetization is allowed to exchange between chemically distinct ^1H sites as a function of mixing time, which manifests into off-diagonal signals. In the case of 41% *en*/$FAPbBr_3$, no off-diagonal signals were observed at a shorter mixing time of 20 ms, meaning that the mixing times of ≤20 ms were insufficient to allow the magnetization between *en* and FA^+ ^1H sites to be exchanged. At longer mixing times (>50 ms), the ^1H magnetization exchange between *en* and FA^+ cations leads to the off-diagonal signals (red arrows) as depicted in Figure 7c and Figure S21 (Supporting Information), indicating the sub-nano to nanoscale proximities between *en* and FA^+ cations. Overall, 2D ssNMR experiments corroborate the XRD and PDF results and analysis, and provide an atomic-level picture of the local chemical environments of *en* in the $FAPbBr_3$ perovskite.

Optical absorption, photoluminescence and work functions

All compounds exhibit sharp optical absorption edges in their diffuse reflectance spectra. The band gap shifts from 2.20 eV for the pristine $FAPbBr_3$ to 2.60 (and the color of the crystal changes from orange to yellow) for the 42% *en* compound (Figure 8a and Table 2). The removal of Pb-Br fragments from the crystal structure leads to discontinuities in the infinite Pb-Br-Pb connectivity in the 3D lattice, which

reduces the degree of orbital overlap among these atoms and prevents the development of the full possible electronic bandwidth.[30] This change, in turn, results in widening of the bandgap with increasing amount of *en*. Bandgap widening in perovskites was only possible previously through dimensional reduction, which gives rise to the various classes of two-dimensional compounds such as the Ruddlesden-Popper (RP),[63-64] the Dion-Jacobson (DJ),[65-66] and the alternating cation in the interlayer space (ACI) types.[67] The achievement of "hollow" structures presents a second mode of widening the bandgap while keeping the overall dimensionality 3D. This phenomenon can be exploited to precisely tune the band gap of the 3D structure by controlling the incorporation of *en* cations.

The "hollow" bromide perovskite materials exhibit strong, narrow band-edge PL with an energy that is correlated to the amount of *en* incorporated in the crystal, spanning from 543 nm for pristine $FAPbBr_3$ to 480 nm for the 29% *en* sample (Figure 8b). Surprisingly, above 29% *en* loading, the PL peak broadens significantly (Figure S22), and for the 40% *en* sample, there is a very strong and broad emission band centered at 590 nm (Figures 10d, e, f). The intensity is enhanced further by increasing the amount of *en* to up to 44% *en* loading, where it saturates (Figure S23). This finding appears to be related to the additional type of *en* defect that forms in the crystal above 29% *en* loading according to ssNMR (see above). The percentage of the second type of defect increases proportionally to the inserted amount of *en* in the lattice. Structurally this is the only difference between the samples with lower and higher than 29% *en* loading. Therefore, we ascribe the broad emission to the presence of self-trapped excitons (STEs) (see below) generated by the formation of this type of defect. This result is a clear and rare example of the manipulation of the PL emission of halide perovskites by defect engineering.[68-70]

We examined the optical properties of the 42% *en* sample in detail. Under 380-nm excitation, the 42% *en* sample exhibits a broad emission centered at 590 nm with a large full width at half maximum (FWHM) of 195 nm (0.67 eV) accompanied by a large energy shift of 110 nm (0.48 eV) relative to the absorption onset (Figure 9a). The corresponding photoluminescence quantum yield (PLQY) is 1%, while the PL peak position and FWHM are the same regardless of excitation power (Figure S24). This broad emission at RT is unique among 3D hybrid halide perovskites. The only reports of stronger PL emission from 3D halide perovskites are the narrow band-edge emission

of 3D perovskite films, e.g. $MASnI_3$ and $CsSnI_3$[42-43] and the broad emission of the 3D fully inorganic double perovskite $Cs_2(Ag_{0.60}Na_{0.40})InCl_6$.[71]

Furthermore, the intensity and line-shape of the PL emission of the 42% *en* compound is constant after exposure of the perovskite to ambient conditions for a year, demonstrating the excellent structural stability and integrity of the emission of this defective material (Figure S25). We point out that such robust emission is among the highest reported for halide perovskite materials.[72]

The corresponding CIE (International Commission on Illumination) chromaticity coordinates for the 42% *en* compound are (0.47, 0.49), with a much larger contribution from the red region of the spectrum than pure white light, which has chromaticity coordinates of (0.33, 0.33). This broad emission can be described by a correlated color temperature (CCT) of 3144 K (warm yellow light), and a color-rendering index (CRI) value of 67, which indicates that this light is suitable for outdoor lighting (Figures 10a, b, c and Table 3). CIE coordinates and CCT values were calculated using the ColorCalculator by OSRAM Sylvania, Inc. The CRI index quantifies how accurately illuminated colors are reproduced; for indoor lighting, values above 80 are required.[73]

Interestingly, the emission of the "hollow" bromide materials is very different from that of the iodide analogs, where with increasing amount of *en* above 35% in the latter the PL is increasingly quenched.[30] The difference in PL exhibited by "hollow" bromide and iodide perovskites (i.e., PL from bromide is stronger) qualitatively resembles the difference between layered bromide and iodide perovskites. In layered perovskites, bromides tend to exhibit stronger white-light emission.[74-75] Since layered structure and "hollow" structure both add "softness" to the crystal,[76,77-78] we believe that enhanced broadband PL from bromide perovskites observed for both types of structures likely share the same origin, which warrants further investigation.

We determined the energies of the valence band maxima (VBM) of the corresponding "hollow" bromide compounds with photoemission yield spectroscopy in air (PYSA) measurements,[79] and calculated the conduction band minima (CBM) by adding the corresponding optical band gaps from the measured VBM energies (Figure S26). The incorporation of *en* in the structure lowers the VBM from 5.62 eV in pristine $FAPbBr_3$ to 5.78 eV for the 42% *en* sample. Notably, the latter value is very close to that for the 2D and 1D lead bromide compounds, such as $(2,6\text{-dmpz})_3Pb_2Br_{10}$ with

strong broad light emission (12% PLQY).[80] This finding, coupled with the blue-shift of the optical bandgaps, supports the view that the electronic character of the "hollow" 3D materials is less than 3D and closer to low-dimensional compounds.

Origin of PL

In order to learn more about the mechanism of the broad emission, we performed variable-temperature PL measurements from 80 to 300 K (Figure 9b). Decreasing temperature correlates with a gradual increase in the broad emission intensity up to 180 K with no change in the PL lineshape. At 160 K a new narrow PL peak (FWHM 10.4 nm) appears centered at 498 nm (2.49 eV) accompanied by an increase of the PL intensity by one order of magnitude for both the narrow and the broad PL peaks. The narrow emission is significantly more intense than the below-bandgap broad emission when the temperature is lowered down to 80 K, (FWHM 12.2 nm), but there is no change in energy of the emission for either peak over this temperature range (Figure S27). This behavior is typical for broad-spectrum emitters where there is an energy barrier between the free exciton (FE) and the STE states.[81-82] At room temperature, the thermal energy is large compared to this barrier, and the broad emission from STEs is dominant. At lower temperature, some FEs cannot cross the energy barrier and hence a narrow, higher-energy FE emission appears and increases in intensity with decreasing temperature.[80, 82-83]

There is no detectable change in the PL line shape and emission wavelength at higher temperatures (200 K to 460 K, Figure S28). However, above 300 K, the PL intensity decreases gradually up to 460 K, consistent with increased nonradiative recombination of thermally delocalized carriers in disordered semiconductors.[84-85]

The measured average PL decay lifetime at RT was 15 ns, determined using multi-exponential fitting of the emission decay curve (Figure 9c). This decay includes three exponential components with time constants of 1.6, 10.2, and 22.2 ns. At 80 K, the STE lifetime (measured at 575 nm) shows a fast component followed by a slow single exponential decay with lifetime of 130 ns. Notably, at RT, the recorded lifetime is comparable to those of semiconductor quantum dot materials, with values on the order of a few ns,[86] "hollow' $CsPbBr_3$ nanocrystals,[36] 1D strong light emitting metal halide materials, such as $C_4N_2H_{14}PbBr_4$ (a few tens of ns),[87] and 2D white light emitters such as $[(C_6H_5C_2H_4NH_3)_2PbCl_4]$ (a few ns).[88] Comparing the lifetimes for the FE and STE at RT and 80K, time-resolved photoluminescence (TRPL) studies revealed that

there is an equilibrium between FE and STE at RT (Figure S29). However, at 80K there is a clear difference between the faster decay of the FE in comparison to the STE, demonstrating the better separation between FE and STE (Figure S30), as indicated also by the appearance of the two separate PL peaks (Figure 9b).

Power-dependent PL studies (up to 900 mW cm^{-2}) indicate a linear correlation between the PL intensity and the excitation power density. This suggests that the emission stems from STEs (Figure 9d)[89-91] and not permanent defects, where the PL emission saturates at higher excitation power.[18, 39, 92]

CONCLUSIONS

Significant amounts of *en* can be incorporated in the crystal structure of $FAPbBr_3$ without causing a structural transformation to a two-dimensional or other low-dimensional material. The *en* cation is considered too large and outside the scope of the so-called Goldschmidt tolerance factor to be incorporated in a perovskite cage. However, because of the creation of vacancies by Pb and Br atoms, adjacent cages can fuse to become larger cages effectively making the Goldschmidt tolerance factor irrelevant. Taking advantage of the chemical versatility of hybrid perovskites, we created a new family of environmentally stable "hollow" 3D hybrid halide perovskites with general formula $(FA)_{1-x}(en)_x(Pb)_{1-0.7x}(Br)_{3-0.4x}$, x = 0-0.44. The *en* cations induce randomly dispersed vacancy defects in the lattice by replacing Pb, Br, and FA moieties. Solid state NMR studies suggest that *en* cations are well dispersed into the perovskite framework at *en* loadings less than 30%, whereas two types of local chemical environments of *en* molecules are observed at *en* loadings greater than 30%. By manipulating the amount of incorporated *en*, the optical properties of the corresponding crystals can be fine-tuned over a wide energy range both in terms of emission and absorption spectra. Above 33% *en* inclusion, the "hollow" bromide perovskite emits strong broad light at room temperature that is directly correlated to the number of defects, increasing gradually in intensity for 42%, and reaching a plateau at 44% *en*, with 1% PLQY coupled with a lifetime of 15 ns. Considering that the only structural difference between the compounds with narrow and broad emission is the presence of another type of defect above 29% *en* loading, we ascribe the formation of STEs at RT to its presence. The corresponding material maintains its strong PL emission for at least one year in air exposure. This is the first time that strong broad light emission from a 3D hybrid halide perovskite has been observed, while its PL robustness under ambient

conditions is among the highest reported for halide perovskites. Our work demonstrates in a most concrete manner the highly defect tolerant nature of hybrid halide perovskites which is considered to be the cornerstone of many of their prominent traits, such as the hard radiation damage resilience.

ASSOCIATED CONTENT

Supporting Information

Materials and methods, synthetic details, additional supplementary figures and tables about material characterization, X-ray diffraction measurements, photoluminescence measurements, thermogravimetric analysis, NMR, XRF, EDS and PYSA measurements.

This material is available free of charge via the Internet at http://pubs.acs.org.

Accession Codes

CCDC 2062752-2062755 contain the supplementary crystallographic data for this paper. These data can be obtained free of charge via www.ccdc.cam.ac.uk/data_request/cif,orbyemailingdata_request@ccdc.cam.ac.uk, or by contacting The Cambridge Crystallographic Data Centre, 12 Union Road, Cambridge CB2 1EZ, UK; fax: +44 1223 336033.

AUTHOR INFORMATION

Corresponding Author

m-kanatzidis@northwestern.edu

Present addresses

[#]Department of Chemical and Environmental Engineering, Yale University, 9 Hillhouse Avenue, New Haven, CT 06520, USA

§ School of Physics and Technology, Wuhan University, Wuhan, 430072, People's Republic of China

& Center for Nanoscience and Nanotechnology, Hebrew University of Jerusalem, Israel

Notes

The authors declare no competing financial interest.

ACKNOWLEDGMENT

This work was primarily supported by the Department of Energy, Office of Science, Basic Energy Sciences, under Grant No. SC0012541 (sample synthesis, structure and property characterization). Photoluminescence measurements were supported by the National Science Foundation (NSF) Materials Research Science and Engineering Center (MRSEC) at Northwestern University (NSF DMR-1720139). This work made use of the SPID and EPIC facilities of Northwestern University's NU*ANCE* Center, as well as the IMSERC facilities, which have received support from the Soft and Hybrid Nanotechnology Experimental (SHyNE) Resource (NSF ECCS-1542205), the MRSEC program (NSF DMR-1720139) at the Materials Research Center, the State of Illinois, and the International Institute for Nanotechnology (IIN). This work was performed, in part, at the Center for Nanoscale Materials, a U.S. Department of Energy Office of Science User Facility, and supported by the U.S. Department of Energy, Office of Science, under Contract No. DE-AC02-06CH11357. The MRL Shared Experimental Facilities are supported by the MRSEC Program of the NSF under Award No. DMR 1720256; a member of the NSF-funded Materials Research Facilities Network.

REFERENCES

1. Stoumpos, C. C.; Kanatzidis, M. G., The Renaissance of Halide Perovskites and Their Evolution as Emerging Semiconductors, *Acc. Chem. Res.* **2015,** *48*, 2791-2802.
2. Stoumpos, C. C.; Kanatzidis, M. G., Halide Perovskites: Poor Man's High-Performance Semiconductors, *Adv. Mater.* **2016,** *28*, 5778-5793.
3. Berry, J.; Buonassisi, T.; Egger, D. A.; Hodes, G.; Kronik, L.; Loo, Y.-L.; Lubomirsky, I.; Marder, S. R.; Mastai, Y.; Miller, J. S.; Mitzi, D. B.; Paz, Y.; Rappe, A. M.; Riess, I.; Rybtchinski, B.; Stafsudd, O.; Stevanovic, V.; Toney, M. F.; Zitoun, D.; Kahn, A.; Ginley, D.; Cahen, D., Hybrid Organic–Inorganic Perovskites (HOIPs): Opportunities and Challenges, *Adv. Mater.* **2015,** *27*, 5102-5112.
4. Manser, J. S.; Christians, J. A.; Kamat, P. V., Intriguing Optoelectronic Properties of Metal Halide Perovskites, *Chem. Rev.* **2016,** *116*, 12956-13008.
5. Chen, K.; Schünemann, S.; Song, S.; Tüysüz, H., Structural effects on optoelectronic properties of halide perovskites, *Chem. Soc. Rev.* **2018,** *47*, 7045-7077.
6. Saparov, B.; Mitzi, D. B., Organic–Inorganic Perovskites: Structural Versatility for Functional Materials Design, *Chem. Rev.* **2016,** *116*, 4558-4596.
7. Chouhan, L.; Ghimire, S.; Subrahmanyam, C.; Miyasaka, T.; Biju, V., Synthesis, optoelectronic properties and applications of halide perovskites, *Chem. Soc. Rev.* **2020,** *49*, 2869-2885.
8. Koji, Y.; Hiroshi, K.; Takashi, M.; Tsutomu, O.; Sumio, I., Structural Phase Transition and Electrical Conductivity of the Perovskite $CH_3NH_3Sn_{1-x}Pb_xBr_3$ and $CsSnBr_3$, *Bull. Chem. Soc. Jpn.* **1990,** *63*, 2521-2525.
9. Stoumpos, C. C.; Malliakas, C. D.; Kanatzidis, M. G., Semiconducting Tin and Lead Iodide Perovskites with Organic Cations: Phase Transitions, High Mobilities, and Near-Infrared Photoluminescent Properties, *Inorg. Chem.* **2013,** *52*, 9019-9038.
10. MØLler, C. K., Crystal Structure and Photoconductivity of Cæsium Plumbohalides, *Nature* **1958,** *182*, 1436-1436.
11. Wang, P.; Wu, Y.; Cai, B.; Ma, Q.; Zheng, X.; Zhang, W.-H., Solution-Processable Perovskite Solar

Cells toward Commercialization: Progress and Challenges, *Adv. Funct. Mater.* **2019,** *29*, 1807661.
12. Zhao, D.; Yu, Y.; Wang, C.; Liao, W.; Shrestha, N.; Grice, C. R.; Cimaroli, A. J.; Guan, L.; Ellingson, R. J.; Zhu, K.; Zhao, X.; Xiong, R.-G.; Yan, Y., Low-bandgap mixed tin–lead iodide perovskite absorbers with long carrier lifetimes for all-perovskite tandem solar cells, *Nat. Energy* **2017,** *2*, 17018.
13. Stranks, S. D.; Eperon, G. E.; Grancini, G.; Menelaou, C.; Alcocer, M. J. P.; Leijtens, T.; Herz, L. M.; Petrozza, A.; Snaith, H. J., Electron-Hole Diffusion Lengths Exceeding 1 Micrometer in an Organometal Trihalide Perovskite Absorber, *Science* **2013,** *342*, 341-344.
14. Dong, Q.; Fang, Y.; Shao, Y.; Mulligan, P.; Qiu, J.; Cao, L.; Huang, J., Electron-hole diffusion lengths > 175 μm in solution-grown $CH_3NH_3PbI_3$ single crystals, *Science* **2015,** *347*, 967-970.
15. Wei, H.; Huang, J., Halide lead perovskites for ionizing radiation detection, *Nat. Commun.* **2019,** *10*, 1066.
16. Kanaya, S.; Kim, G. M.; Ikegami, M.; Miyasaka, T.; Suzuki, K.; Miyazawa, Y.; Toyota, H.; Osonoe, K.; Yamamoto, T.; Hirose, K., Proton Irradiation Tolerance of High-Efficiency Perovskite Absorbers for Space Applications, *J. Phys. Chem. Lett.* **2019,** *10*, 6990-6995.
17. Reb, L. K.; Böhmer, M.; Predeschly, B.; Grott, S.; Weindl, C. L.; Ivandekic, G. I.; Guo, R.; Dreißigacker, C.; Gernhäuser, R.; Meyer, A.; Müller-Buschbaum, P., Perovskite and Organic Solar Cells on a Rocket Flight, *Joule* **2020,** *4*, 1880-1892.
18. Meggiolaro, D.; Motti, S. G.; Mosconi, E.; Barker, A. J.; Ball, J.; Andrea Riccardo Perini, C.; Deschler, F.; Petrozza, A.; De Angelis, F., Iodine chemistry determines the defect tolerance of lead-halide perovskites, *Energy Environ. Sci.* **2018,** *11*, 702-713.
19. Chu, W.; Zheng, Q.; Prezhdo, O. V.; Zhao, J.; Saidi, W. A., Low-frequency lattice phonons in halide perovskites explain high defect tolerance toward electron-hole recombination, *Sci. Adv.* **2020,** *6*, eaaw7453.
20. Kim, G.-W.; Petrozza, A., Defect Tolerance and Intolerance in Metal-Halide Perovskites, *Adv. Energy Mater.* **2020,** *10*, 2001959.
21. Kumar, S.; Hodes, G.; Cahen, D., Defects in halide perovskites: The lattice as a boojum?, *MRS Bull.* **2020,** *45*, 478-484.
22. Yin, W.-J.; Shi, T.; Yan, Y., Superior Photovoltaic Properties of Lead Halide Perovskites: Insights from First-Principles Theory, *J. Phys. Chem. C* **2015,** *119*, 5253-5264.
23. Huang, J.; Yuan, Y.; Shao, Y.; Yan, Y., Understanding the physical properties of hybrid perovskites for photovoltaic applications, *Nat. Rev. Mater.* **2017,** *2*, 17042.
24. Sun, C.; Xu, L.; Lai, X.; Li, Z.; He, M., Advanced Strategies of Passivating Perovskite Defects for High-Performance Solar Cells, *Energy Environ. Mater.* **2020,** *0*, 1-10.
25. Leblanc, A.; Mercier, N.; Allain, M.; Dittmer, J.; Pauporté, T.; Fernandez, V.; Boucher, F.; Kepenekian, M.; Katan, C., Enhanced Stability and Band Gap Tuning of α-$[HC(NH_2)_2]PbI_3$ Hybrid Perovskite by Large Cation Integration, *ACS Appl. Mater. Interfaces* **2019,** *11*, 20743-20751.
26. Leblanc, A.; Mercier, N.; Allain, M.; Dittmer, J.; Fernandez, V.; Pauporté, T., Lead- and Iodide-Deficient $(CH_3NH_3)PbI_3$ (d-MAPI): The Bridge between 2D and 3D Hybrid Perovskites, *Angew. Chem. Int. Ed.* **2017,** *56*, 16067-16072.
27. Tsai, C.-M.; Lin, Y.-P.; Pola, M. K.; Narra, S.; Jokar, E.; Yang, Y.-W.; Diau, E. W.-G., Control of Crystal Structures and Optical Properties with Hybrid Formamidinium and 2-Hydroxyethylammonium Cations for Mesoscopic Carbon-Electrode Tin-Based Perovskite Solar Cells, *ACS Energy Lett.* **2018,** *3*, 2077-2085.
28. McNulty, J. A.; Slawin, A. M. Z.; Lightfoot, P., Variable dimensionality in 'hollow' hybrid tin iodide perovskites, *Dalton Trans.* **2020,** *49*, 15171-15174.
29. Ke, W.; Stoumpos, C. C.; Zhu, M.; Mao, L.; Spanopoulos, I.; Liu, J.; Kontsevoi, O. Y.; Chen, M.; Sarma, D.; Zhang, Y.; Wasielewski, M. R.; Kanatzidis, M. G., Enhanced photovoltaic performance and stability with a new type of hollow 3D perovskite {en}$FASnI_3$, *Sci. Adv.* **2017,** *3*, e1701293.
30. Spanopoulos, I.; Ke, W.; Stoumpos, C. C.; Schueller, E. C.; Kontsevoi, O. Y.; Seshadri, R.; Kanatzidis, M. G., Unraveling the Chemical Nature of the 3D "Hollow" Hybrid Halide Perovskites, *J. Am. Chem. Soc.* **2018,** *140*, 5728-5742.
31. Ke, W.; Stoumpos, C. C.; Spanopoulos, I.; Chen, M.; Wasielewski, M. R.; Kanatzidis, M. G., Diammonium Cations in the FASnI3 Perovskite Structure Lead to Lower Dark Currents and More Efficient Solar Cells, *ACS Energy Lett.* **2018,** *3*, 1470-1476.
32. Ke, W.; Spanopoulos, I.; Tu, Q.; Hadar, I.; Li, X.; Shekhawat, G. S.; Dravid, V. P.; Kanatzidis, M. G., Ethylenediammonium-Based "Hollow" Pb/Sn Perovskites with Ideal Band Gap Yield Solar Cells with Higher Efficiency and Stability, *J. Am. Chem. Soc.* **2019,** *141*, 8627-8637.
33. Abramov, Y. A.; Tsirelson, V. G.; Zavodnik, V. E.; Ivanov, S. A.; Brown I. D., The chemical bond

and atomic displacements in $SrTiO_3$ from X-ray diffraction analysis, *Acta Crystallogr. Sect. B* **1995,** *51*, 942-951.
34. Cowley, R. A., Lattice Dynamics and Phase Transitions of Strontium Titanate, *Phys. Rev.* **1964,** *134*, A981-A997.
35. Senocrate, A.; Spanopoulos, I.; Zibouche, N.; Maier, J.; Islam, M. S.; Kanatzidis, M. G., Tuning Ionic and Electronic Conductivities in the "Hollow" Perovskite {*en*}$MAPbI_3$, *Chem. Mater.* **2021,** *33*, 719-726.
36. Worku, M.; Tian, Y.; Zhou, C.; Lin, H.; Chaaban, M.; Xu, L.-j.; He, Q.; Beery, D.; Zhou, Y.; Lin, X.; Su, Y.-f.; Xin, Y.; Ma, B., Hollow metal halide perovskite nanocrystals with efficient blue emissions, *Sci. Adv.* **2020,** *6*, eaaz5961.
37. Yakunin, S.; Chaaban, J.; Benin, B. M.; Cherniukh, I.; Bernasconi, C.; Landuyt, A.; Shynkarenko, Y.; Bolat, S.; Hofer, C.; Romanyuk, Y. E.; Cattaneo, S.; Pokutnyi, S. I.; Schaller, R. D.; Bodnarchuk, M. I.; Poulikakos, D.; Kovalenko, M. V., Radiative lifetime-encoded unicolour security tags using perovskite nanocrystals, *Nat. Commun.* **2021,** *12*, 981.
38. Liu, X.-K.; Xu, W.; Bai, S.; Jin, Y.; Wang, J.; Friend, R. H.; Gao, F., Metal halide perovskites for light-emitting diodes, *Nat. Mater.* **2021,** *20*, 10-21.
39. Spanopoulos, I.; Hadar, I.; Ke, W.; Guo, P.; Sidhik, S.; Kepenekian, M.; Even, J.; Mohite, A. D.; Schaller, R. D.; Kanatzidis, M. G., Water-Stable 1D Hybrid Tin(II) Iodide Emits Broad Light with 36% Photoluminescence Quantum Efficiency, *J. Am. Chem. Soc.* **2020,** *142*, 9028-9038.
40. Wang, A.; Guo, Y.; Zhou, Z.; Niu, X.; Wang, Y.; Muhammad, F.; Li, H.; Zhang, T.; Wang, J.; Nie, S.; Deng, Z., Aqueous acid-based synthesis of lead-free tin halide perovskites with near-unity photoluminescence quantum efficiency, *Chem. Sci.* **2019,** *10*, 4573-4579.
41. Zhou, C.; Tian, Y.; Yuan, Z.; Lin, H.; Chen, B.; Clark, R.; Dilbeck, T.; Zhou, Y.; Hurley, J.; Neu, J.; Besara, T.; Siegrist, T.; Djurovich, P.; Ma, B., Highly Efficient Broadband Yellow Phosphor Based on Zero-Dimensional Tin Mixed-Halide Perovskite, *ACS Appl. Mater. Interfaces* **2017,** *9*, 44579-44583.
42. Lai, M. L.; Tay, T. Y. S.; Sadhanala, A.; Dutton, S. E.; Li, G.; Friend, R. H.; Tan, Z.-K., Tunable Near-Infrared Luminescence in Tin Halide Perovskite Devices, *J. Phys. Chem. Lett.* **2016,** *7*, 2653-2658.
43. Xing, G.; Kumar, M. H.; Chong, W. K.; Liu, X.; Cai, Y.; Ding, H.; Asta, M.; Grätzel, M.; Mhaisalkar, S.; Mathews, N.; Sum, T. C., Solution-Processed Tin-Based Perovskite for Near-Infrared Lasing, *Adv. Mater.* **2016,** *28*, 8191-8196.
44. Xiao, Z.; Kerner, R. A.; Zhao, L.; Tran, N. L.; Lee, K. M.; Koh, T.-W.; Scholes, G. D.; Rand, B. P., Efficient perovskite light-emitting diodes featuring nanometre-sized crystallites, *Nat. Photon.* **2017,** *11*, 108-115.
45. Lemmerer, A.; Billing, D. G., Lead halide inorganic-organic hybrids incorporating diammonium cations, *CrystEngComm* **2012,** *14*, 1954-1966.
46. Mozur, E. M.; Hope, M. A.; Trowbridge, J. C.; Halat, D. M.; Daemen, L. L.; Maughan, A. E.; Prisk, T. R.; Grey, C. P.; Neilson, J. R., Cesium Substitution Disrupts Concerted Cation Dynamics in Formamidinium Hybrid Perovskites, *Chem. Mater.* **2020,** *32*, 6266-6277.
47. Schueller, E. C.; Laurita, G.; Fabini, D. H.; Stoumpos, C. C.; Kanatzidis, M. G.; Seshadri, R., Crystal Structure Evolution and Notable Thermal Expansion in Hybrid Perovskites Formamidinium Tin Iodide and Formamidinium Lead Bromide, *Inorg. Chem.* **2018,** *57*, 695-701.
48. Spanopoulos, I.; Hadar, I.; Ke, W.; Tu, Q.; Chen, M.; Tsai, H.; He, Y.; Shekhawat, G.; Dravid, V. P.; Wasielewski, M. R.; Mohite, A. D.; Stoumpos, C. C.; Kanatzidis, M. G., Uniaxial Expansion of the 2D Ruddlesden–Popper Perovskite Family for Improved Environmental Stability, *J. Am. Chem. Soc.* **2019,** *141*, 5518-5534.
49. Whitfield, P. S.; Herron, N.; Guise, W. E.; Page, K.; Cheng, Y. Q.; Milas, I.; Crawford, M. K., Structures, Phase Transitions and Tricritical Behavior of the Hybrid Perovskite Methyl Ammonium Lead Iodide, *Sci. Rep.* **2016,** *6*, 35685.
50. Ong, K. P.; Goh, T. W.; Xu, Q.; Huan, A., Structural Evolution in Methylammonium Lead Iodide $CH_3NH_3PbI_3$, *J. Phys. Chem. A* **2015,** *119*, 11033-11038.
51. Fabini, D. H.; Stoumpos, C. C.; Laurita, G.; Kaltzoglou, A.; Kontos, A. G.; Falaras, P.; Kanatzidis, M. G.; Seshadri, R., Reentrant Structural and Optical Properties and Large Positive Thermal Expansion in Perovskite Formamidinium Lead Iodide, *Angew. Chem., Int. Ed.* **2016,** *55*, 15392-15396.
52. Weber, O. J.; Ghosh, D.; Gaines, S.; Henry, P. F.; Walker, A. B.; Islam, M. S.; Weller, M. T., Phase Behavior and Polymorphism of Formamidinium Lead Iodide, *Chem. Mater.* **2018,** *30*, 3768-3778.
53. Simenas, M.; Balciunas, S.; Wilson, J. N.; Svirskas, S.; Kinka, M.; Garbaras, A.; Kalendra, V.; Gagor, A.; Szewczyk, D.; Sieradzki, A.; Maczka, M.; Samulionis, V.; Walsh, A.; Grigalaitis, R.; Banys, J.,

Suppression of phase transitions and glass phase signatures in mixed cation halide perovskites, *Nat. Commun.* **2020,** *11*, 5103.
54. Fung, K. Z.; Virkar, A. V., Phase Stability, Phase Transformation Kinetics, and Conductivity of Y_2O_3—Bi_2O_3 Solid Electrolytes Containing Aliovalent Dopants, *J. Am. Ceram. Soc.* **1991,** *74*, 1970-1980.
55. Ding, H.; Virkar, A. V.; Liu, F., Defect configuration and phase stability of cubic versus tetragonal yttria-stabilized zirconia, *Solid State Ionics* **2012,** *215*, 16-23.
56. Jiang, B.; Grande, T.; Selbach, S. M., Local Structure of Disordered Bi0.5K0.5TiO3 Investigated by Pair Distribution Function Analysis and First-Principles Calculations, *Chem. Mater.* **2017,** *29*, 4244-4252.
57. Young, C. A.; Goodwin, A. L., Applications of pair distribution function methods to contemporary problems in materials chemistry, *J. Mater. Chem.* **2011,** *21*, 6464-6476.
58. Billinge, S. J. L.; Kanatzidis, M. G., Beyond crystallography: the study of disorder, nanocrystallinity and crystallographically challenged materials with pair distribution functions, *Chem. Commun.* **2004**, 749-760.
59. Piveteau, L.; Morad, V.; Kovalenko, M. V., Solid-State NMR and NQR Spectroscopy of Lead-Halide Perovskite Materials, *J. Am. Chem. Soc.* **2020,** *142*, 19413-19437.
60. Alharbi, E. A.; Alyamani, A. Y.; Kubicki, D. J.; Uhl, A. R.; Walder, B. J.; Alanazi, A. Q.; Luo, J.; Burgos-Caminal, A.; Albadri, A.; Albrithen, H.; Alotaibi, M. H.; Moser, J.-E.; Zakeeruddin, S. M.; Giordano, F.; Emsley, L.; Grätzel, M., Atomic-level passivation mechanism of ammonium salts enabling highly efficient perovskite solar cells, *Nat. Commun.* **2019,** *10*, 3008.
61. Akhavan Kazemi, M. A.; Raval, P.; Cherednichekno, K.; Chotard, J.-N.; Krishna, A.; Demortiere, A.; Reddy, G. N. M.; Sauvage, F., Molecular-Level Insight into Correlation between Surface Defects and Stability of Methylammonium Lead Halide Perovskite Under Controlled Humidity, *Small Methods* **2020**, 2000834.
62. Seifrid, M.; Reddy, G. N. M.; Chmelka, B. F.; Bazan, G. C., Insight into the structures and dynamics of organic semiconductors through solid-state NMR spectroscopy, *Nat. Rev. Mater.* **2020,** *5*, 910-930.
63. Stoumpos, C. C.; Cao, D. H.; Clark, D. J.; Young, J.; Rondinelli, J. M.; Jang, J. I.; Hupp, J. T.; Kanatzidis, M. G., Ruddlesden–Popper Hybrid Lead Iodide Perovskite 2D Homologous Semiconductors, *Chem. Mater.* **2016,** *28*, 2852-2867.
64. Battle, P. D.; Green, M. A.; Lago, J.; Millburn, J. E.; Rosseinsky, M. J.; Vente, J. F., Crystal and Magnetic Structures of $Ca_4Mn_3O_{10}$, an n = 3 Ruddlesden−Popper Compound, *Chem. Mater.* **1998,** *10*, 658-664.
65. Mao, L.; Ke, W.; Pedesseau, L.; Wu, Y.; Katan, C.; Even, J.; Wasielewski, M. R.; Stoumpos, C. C.; Kanatzidis, M. G., Hybrid Dion–Jacobson 2D Lead Iodide Perovskites, *J. Am. Chem. Soc.* **2018,** *140*, 3775-3783.
66. Dion, M.; Ganne, M.; Tournoux, M., Nouvelles familles de phases $M^{I}M^{II}{}_2Nb_3O_{10}$ a feuillets "perovskites", *Mater. Res. Bull.* **1981,** *16*, 1429-1435.
67. Soe, C. M. M.; Stoumpos, C. C.; Kepenekian, M.; Traoré, B.; Tsai, H.; Nie, W.; Wang, B.; Katan, C.; Seshadri, R.; Mohite, A. D.; Even, J.; Marks, T. J.; Kanatzidis, M. G., New Type of 2D Perovskites with Alternating Cations in the Interlayer Space, $(C(NH_2)_3)(CH_3NH_3)_nPb_nI_{3n+1}$: Structure, Properties, and Photovoltaic Performance, *J. Am. Chem. Soc.* **2017,** *139*, 16297-16309.
68. Li, S.; Zhu, Q.; Li, X.; Sun, X.; Li, J.-G., Near-infrared emitting microspheres of $LaAlO_3$:Mn^{4+}: Defects engineering via Ge^{4+} doping for greatly enhanced luminescence and improved afterglow, *J. Alloys Compd.* **2020,** *827*, 154365.
69. Cortecchia, D.; Mróz, W.; Neutzner, S.; Borzda, T.; Folpini, G.; Brescia, R.; Petrozza, A., Defect Engineering in 2D Perovskite by Mn(II) Doping for Light-Emitting Applications, *Chem* **2019,** *5*, 2146-2158.
70. Seth, S.; Ahmed, T.; De, A.; Samanta, A., Tackling the Defects, Stability, and Photoluminescence of $CsPbX_3$ Perovskite Nanocrystals, *ACS Energy Lett.* **2019,** *4*, 1610-1618.
71. Luo, J.; Wang, X.; Li, S.; Liu, J.; Guo, Y.; Niu, G.; Yao, L.; Fu, Y.; Gao, L.; Dong, Q.; Zhao, C.; Leng, M.; Ma, F.; Liang, W.; Wang, L.; Jin, S.; Han, J.; Zhang, L.; Etheridge, J.; Wang, J.; Yan, Y.; Sargent, E. H.; Tang, J., Efficient and stable emission of warm-white light from lead-free halide double perovskites, *Nature* **2018,** *563*, 541-545.
72. Sun, C.; Gao, Z.; Deng, Y.; Liu, H.; Wang, L.; Su, S.; Li, P.; Li, H.; Zhang, Z.; Bi, W., Orange to Red, Emission-Tunable Mn-Doped Two-Dimensional Perovskites with High Luminescence and Stability, *ACS Appl. Mater. Interfaces* **2019,** *11*, 34109-34116.
73. Pimputkar, S.; Speck, J. S.; DenBaars, S. P.; Nakamura, S., Prospects for LED lighting, *Nat. Photon.*

2009, *3*, 180.
74. Lin, C.-W.; Liu, F.; Chen, T.-Y.; Lee, K.-H.; Chang, C.-K.; He, Y.; Leung, T. L.; Ng, A. M. C.; Hsu, C.-H.; Popović, J.; Djurišić, A.; Ahn, H., Structure-Dependent Photoluminescence in Low-Dimensional Ethylammonium, Propylammonium, and Butylammonium Lead Iodide Perovskites, *ACS Appl. Mater. Interfaces* **2020,** *12*, 5008-5016.
75. Deng, C.; Zhou, G.; Chen, D.; Zhao, J.; Wang, Y.; Liu, Q., Broadband Photoluminescence in 2D Organic–Inorganic Hybrid Perovskites: $(C_7H_{18}N_2)PbBr_4$ and $(C_9H_{22}N_2)PbBr_4$, *J. Phys. Chem. Lett.* **2020,** *11*, 2934-2940.
76. Ferreira, A. C.; Létoublon, A.; Paofai, S.; Raymond, S.; Ecolivet, C.; Rufflé, B.; Cordier, S.; Katan, C.; Saidaminov, M. I.; Zhumekenov, A. A.; Bakr, O. M.; Even, J.; Bourges, P., Elastic Softness of Hybrid Lead Halide Perovskites, *Phys. Rev. Lett.* **2018,** *121*, 085502.
77. Wright, A. D.; Verdi, C.; Milot, R. L.; Eperon, G. E.; Pérez-Osorio, M. A.; Snaith, H. J.; Giustino, F.; Johnston, M. B.; Herz, L. M., Electron–phonon coupling in hybrid lead halide perovskites, *Nat. Commun.* **2016,** *7*, 11755.
78. Neukirch, A. J.; Abate, I. I.; Zhou, L.; Nie, W.; Tsai, H.; Pedesseau, L.; Even, J.; Crochet, J. J.; Mohite, A. D.; Katan, C.; Tretiak, S., Geometry Distortion and Small Polaron Binding Energy Changes with Ionic Substitution in Halide Perovskites, *J. Phys. Chem. Lett.* **2018,** *9*, 7130-7136.
79. Harwell, J. R.; Baikie, T. K.; Baikie, I. D.; Payne, J. L.; Ni, C.; Irvine, J. T. S.; Turnbull, G. A.; Samuel, I. D. W., Probing the energy levels of perovskite solar cells via Kelvin probe and UV ambient pressure photoemission spectroscopy, *Phys. Chem. Chem. Phys.* **2016,** *18*, 19738-19745.
80. Mao, L.; Guo, P.; Kepenekian, M.; Hadar, I.; Katan, C.; Even, J.; Schaller, R. D.; Stoumpos, C. C.; Kanatzidis, M. G., Structural Diversity in White-Light-Emitting Hybrid Lead Bromide Perovskites, *J. Am. Chem. Soc.* **2018,** *140*, 13078-13088.
81. Smith, M. D.; Jaffe, A.; Dohner, E. R.; Lindenberg, A. M.; Karunadasa, H. I., Structural origins of broadband emission from layered Pb–Br hybrid perovskites, *Chem. Sci.* **2017,** *8*, 4497-4504.
82. Li, X.; Guo, P.; Kepenekian, M.; Hadar, I.; Katan, C.; Even, J.; Stoumpos, C. C.; Schaller, R. D.; Kanatzidis, M. G., Small Cyclic Diammonium Cation Templated (110)-Oriented 2D Halide (X = I, Br, Cl) Perovskites with White-Light Emission, *Chem. Mater.* **2019,** *31*, 3582-3590.
83. Gautier, R.; Paris, M.; Massuyeau, F., Exciton Self-Trapping in Hybrid Lead Halides: Role of Halogen, *J. Am. Chem. Soc.* **2019,** *141*, 12619-12623.
84. Shakfa, M. K.; Wiemer, M.; Ludewig, P.; Jandieri, K.; Volz, K.; Stolz, W.; Baranovskii, S. D.; Koch, M., Thermal quenching of photoluminescence in Ga(AsBi), *J. Appl. Phys.* **2015,** *117*, 025709.
85. Rubel, O.; Baranovskii, S. D.; Hantke, K.; Kunert, B.; Rühle, W. W.; Thomas, P.; Volz, K.; Stolz, W., Model of temperature quenching of photoluminescence in disordered semiconductors and comparison to experiment, *Phys. Rev. B* **2006,** *73*, 233201.
86. Li, X.; Wu, Y.; Zhang, S.; Cai, B.; Gu, Y.; Song, J.; Zeng, H., $CsPbX_3$ Quantum Dots for Lighting and Displays: Room-Temperature Synthesis, Photoluminescence Superiorities, Underlying Origins and White Light-Emitting Diodes, *Adv. Funct. Mater.* **2016,** *26*, 2435-2445.
87. Yuan, Z.; Zhou, C.; Tian, Y.; Shu, Y.; Messier, J.; Wang, J. C.; van de Burgt, L. J.; Kountouriotis, K.; Xin, Y.; Holt, E.; Schanze, K.; Clark, R.; Siegrist, T.; Ma, B., One-dimensional organic lead halide perovskites with efficient bluish white-light emission, *Nat. Commun.* **2017,** *8*, 14051.
88. Thirumal, K.; Chong, W. K.; Xie, W.; Ganguly, R.; Muduli, S. K.; Sherburne, M.; Asta, M.; Mhaisalkar, S.; Sum, T. C.; Soo, H. S.; Mathews, N., Morphology-Independent Stable White-Light Emission from Self-Assembled Two-Dimensional Perovskites Driven by Strong Exciton–Phonon Coupling to the Organic Framework, *Chem. Mater.* **2017,** *29*, 3947-3953.
89. Zhou, G.; Li, M.; Zhao, J.; Molokeev, M. S.; Xia, Z., Single-Component White-Light Emission in 2D Hybrid Perovskites with Hybridized Halogen Atoms, *Adv. Optical Mater.* **2019,** *7*, 1901335.
90. Lian, L.; Zheng, M.; Zhang, P.; Zheng, Z.; Du, K.; Lei, W.; Gao, J.; Niu, G.; Zhang, D.; Zhai, T.; Jin, S.; Tang, J.; Zhang, X.; Zhang, J., Photophysics in $Cs_3Cu_2X_5$ (X = Cl, Br, or I): Highly Luminescent Self-Trapped Excitons from Local Structure Symmetrization, *Chem. Mater.* **2020,** *32*, 3462-3468.
91. Febriansyah, B.; Giovanni, D.; Ramesh, S.; Koh, T. M.; Li, Y.; Sum, T. C.; Mathews, N.; England, J., Inducing formation of a corrugated, white-light emitting 2D lead-bromide perovskite via subtle changes in templating cation, *J. Mater. Chem. C* **2020,** *8*, 889-893.
92. Paternò, G. M.; Mishra, N.; Barker, A. J.; Dang, Z.; Lanzani, G.; Manna, L.; Petrozza, A., Broadband Defects Emission and Enhanced Ligand Raman Scattering in 0D $Cs_3Bi_2I_9$ Colloidal Nanocrystals, *Adv. Funct. Mater.* **2019,** *29*, 1805299.

Figures

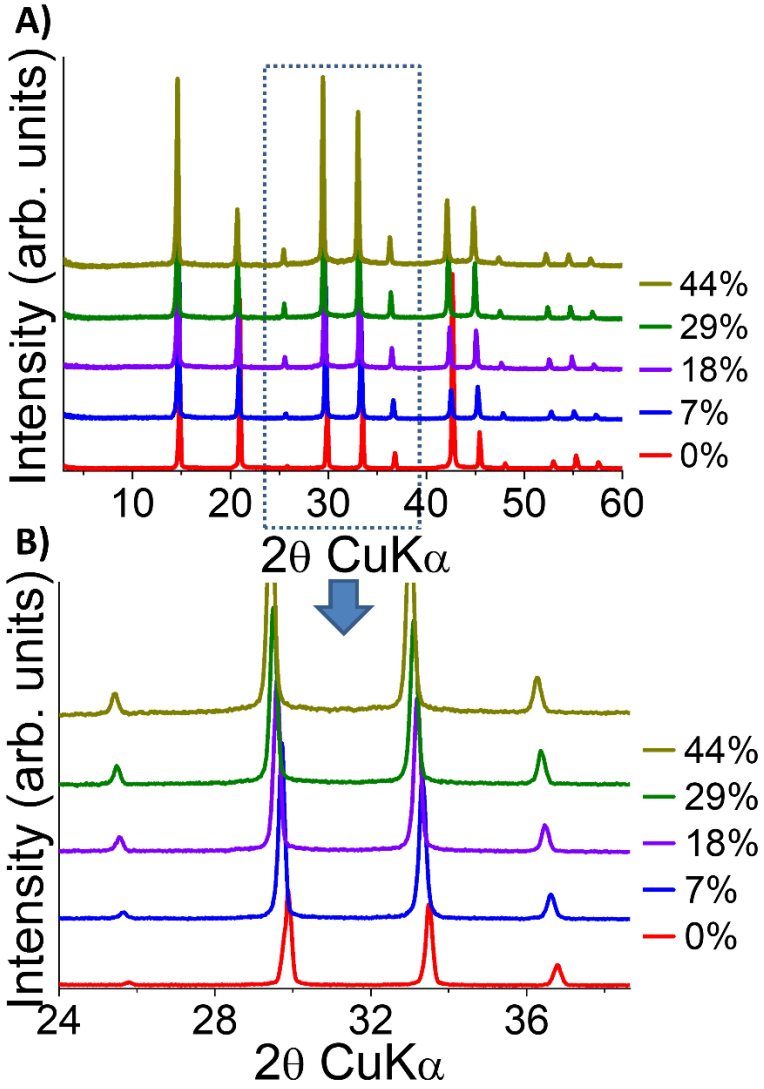

Figure 1. A) Comparison of experimental PXRD patterns of the $(FA)_{1-x}(en)_x(Pb)_{1-0.7x}(Br)_{3-0.4x}$ compounds with increasing amount of *en* (x = 0%, 7%, 18%, 29%, 44%). All materials regardless of x-value are isostructural to cubic α-$FAPbBr_3$ perovskite. B) magnified area of the PXRD patterns from 24° to 37° 2θ showing the shift of the diffraction peaks to lower degrees 2θ with increasing *en* loading, signaling unit cell expansion.

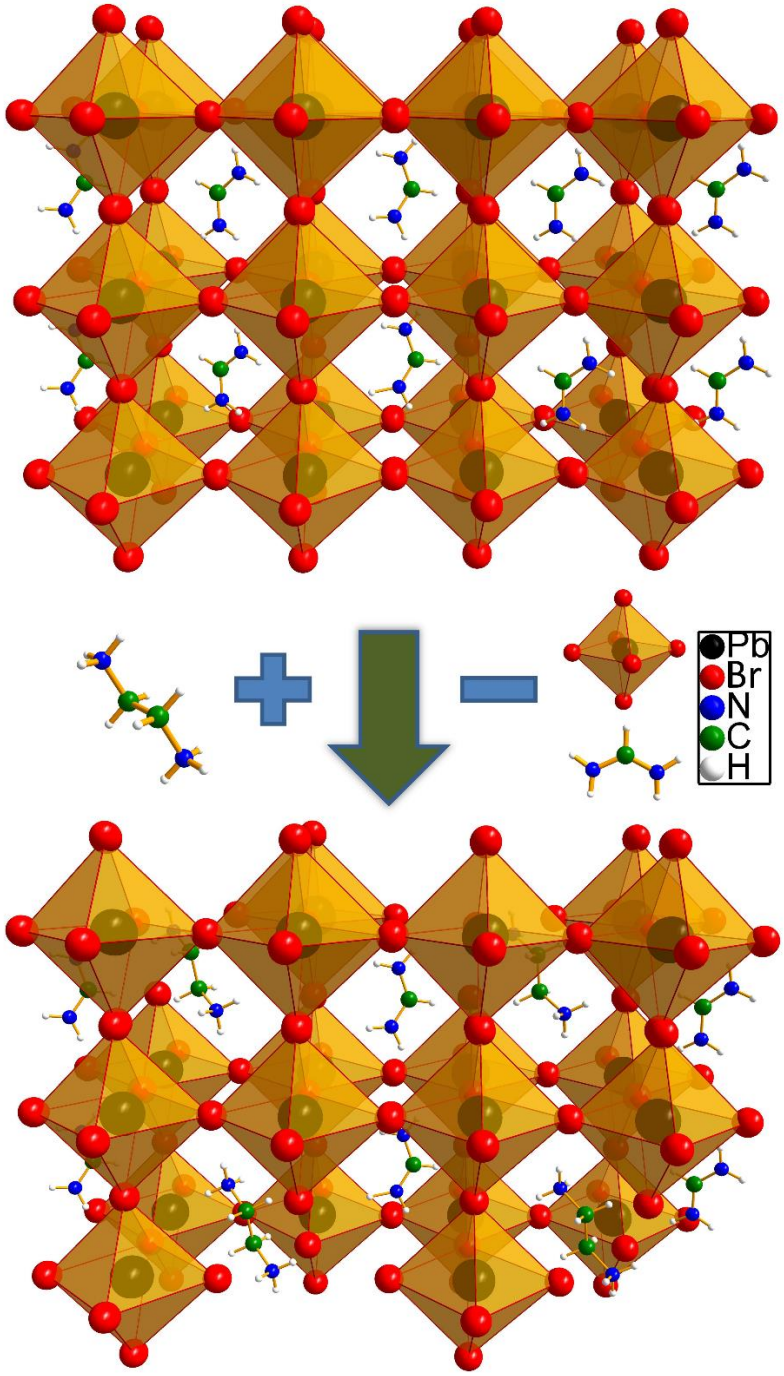

Figure 2. Structural derivation of the "hollow" perovskite from the proper 3D perovskite. In order for *en* cations to be replace formamidinium cations in the lattice without structural rearrangement, $[PbBr_6]^{4-}$ octahedra must be expelled from the structure.

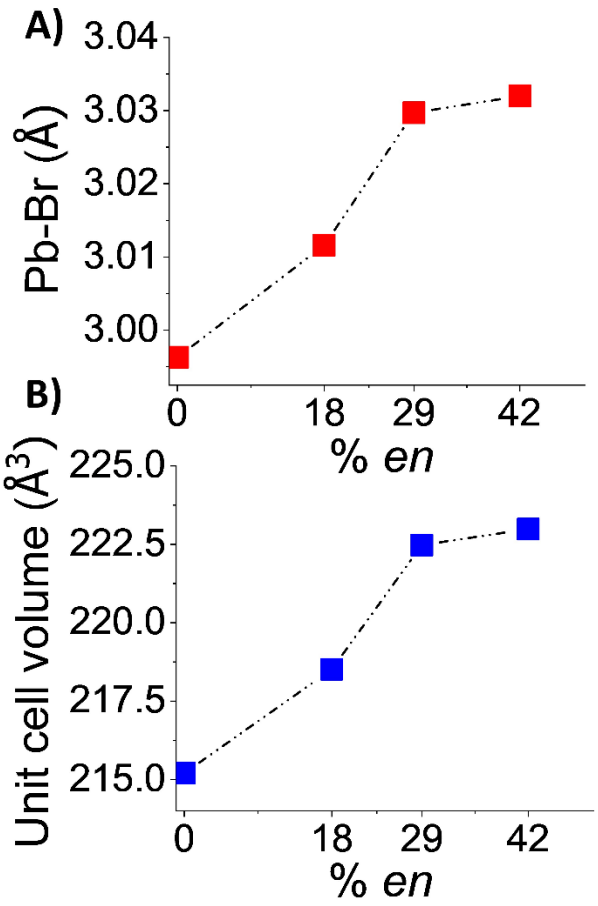

Figure 3. Correlation between the A) Pb-Br bond lengths and B) unit cell volume as a function of the amount of incorporated *en* based on single crystal XRD studies.

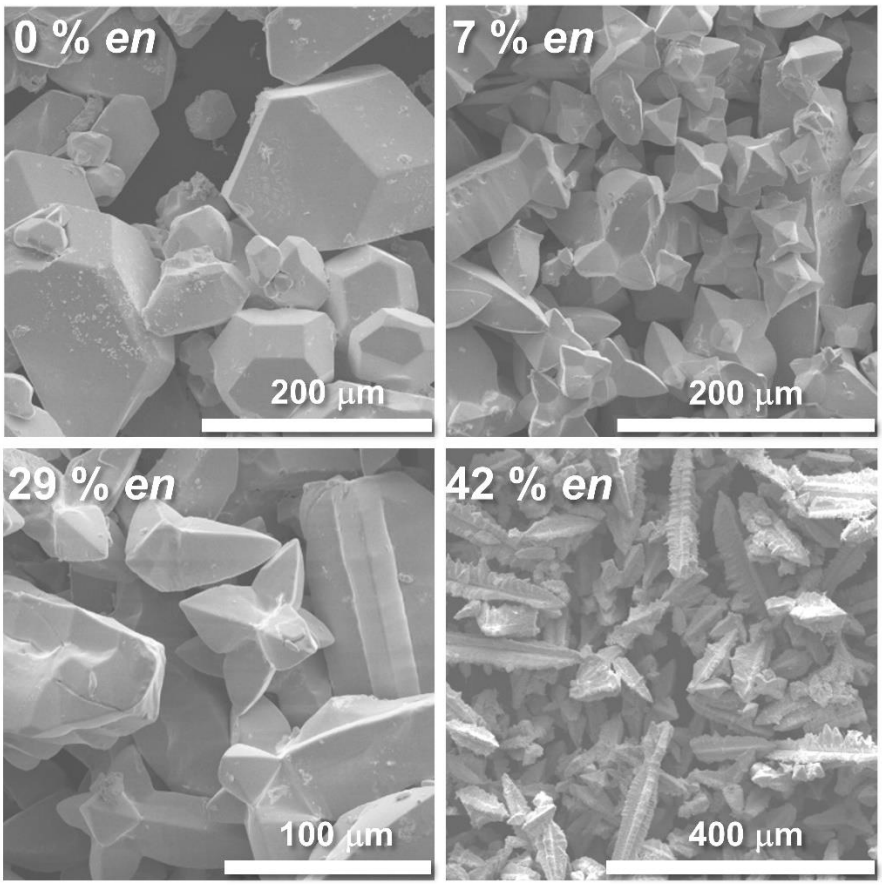

Figure 4. Representative SEM images of as-produced $(FA)_{1-x}(en)_x(Pb)_{1-0.7x}(Br)_{3-0.4x}$ perovskite crystals for x = 0%, 7%, 29%, 42%, respectively. At high *en* loading spear like crystals based on intergrowths of crystal octahedra are observed.

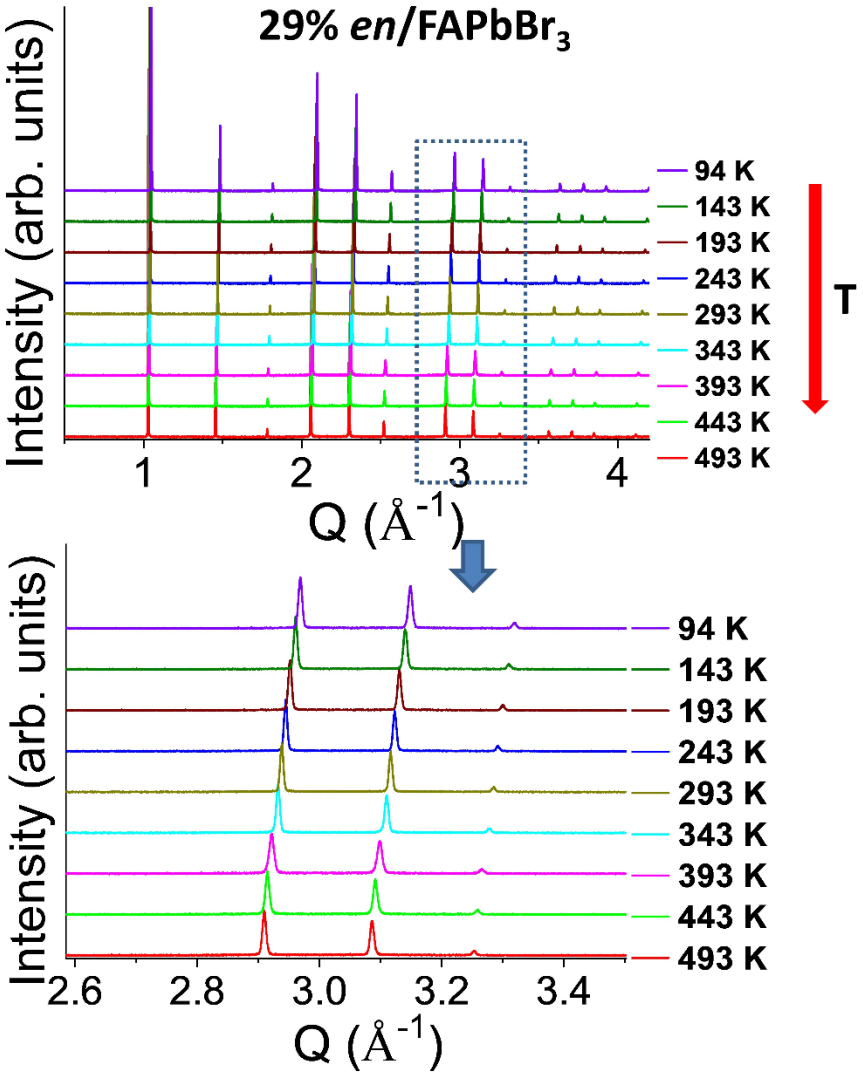

Figure 5. A) High resolution variable temperature PXRD patterns for the 29% *en*/$FAPbBr_3$, consisting of one heating cycle. B) The highlighted area is enlarged to show the shift of the diffraction peaks to lower Q values with increasing temperature, indicative of lattice thermal expansion. There is no appearance of additional diffraction peaks, revealing the absence of temperature dependent structural transitions.

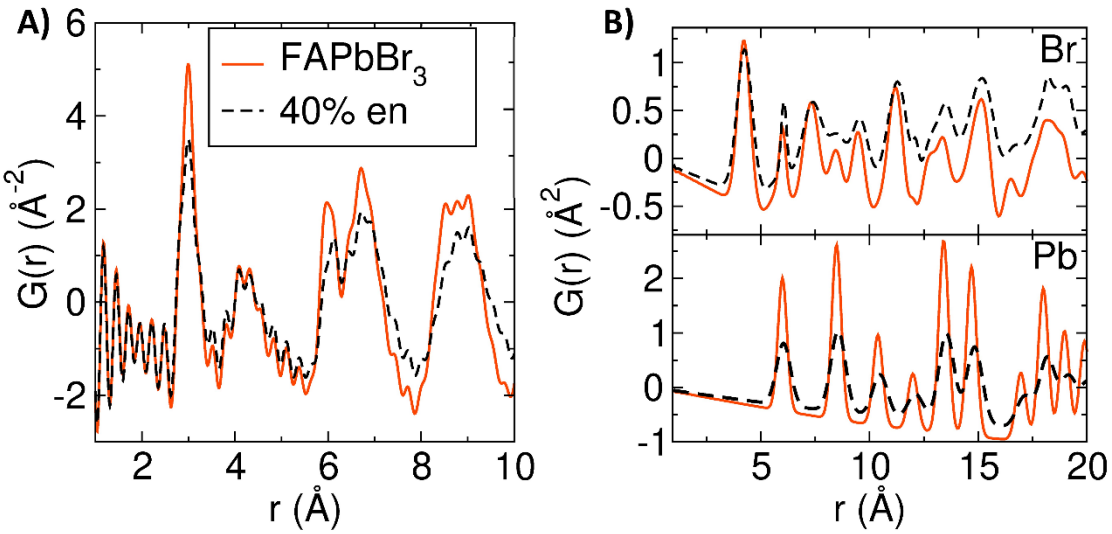

Figure 6. A) PDF G(r) comparison of the pristine $FAPbBr_3$, solid orange line, and 40% *en*/ $FAPbBr_3$, black dashed lines. B) Calculated partial PDF of pristine $FAPbBr_3$ and 40% *en*/ $FAPbBr_3$ describing (top) Br-Br correlations and (bottom) Pb-Pb correlations.

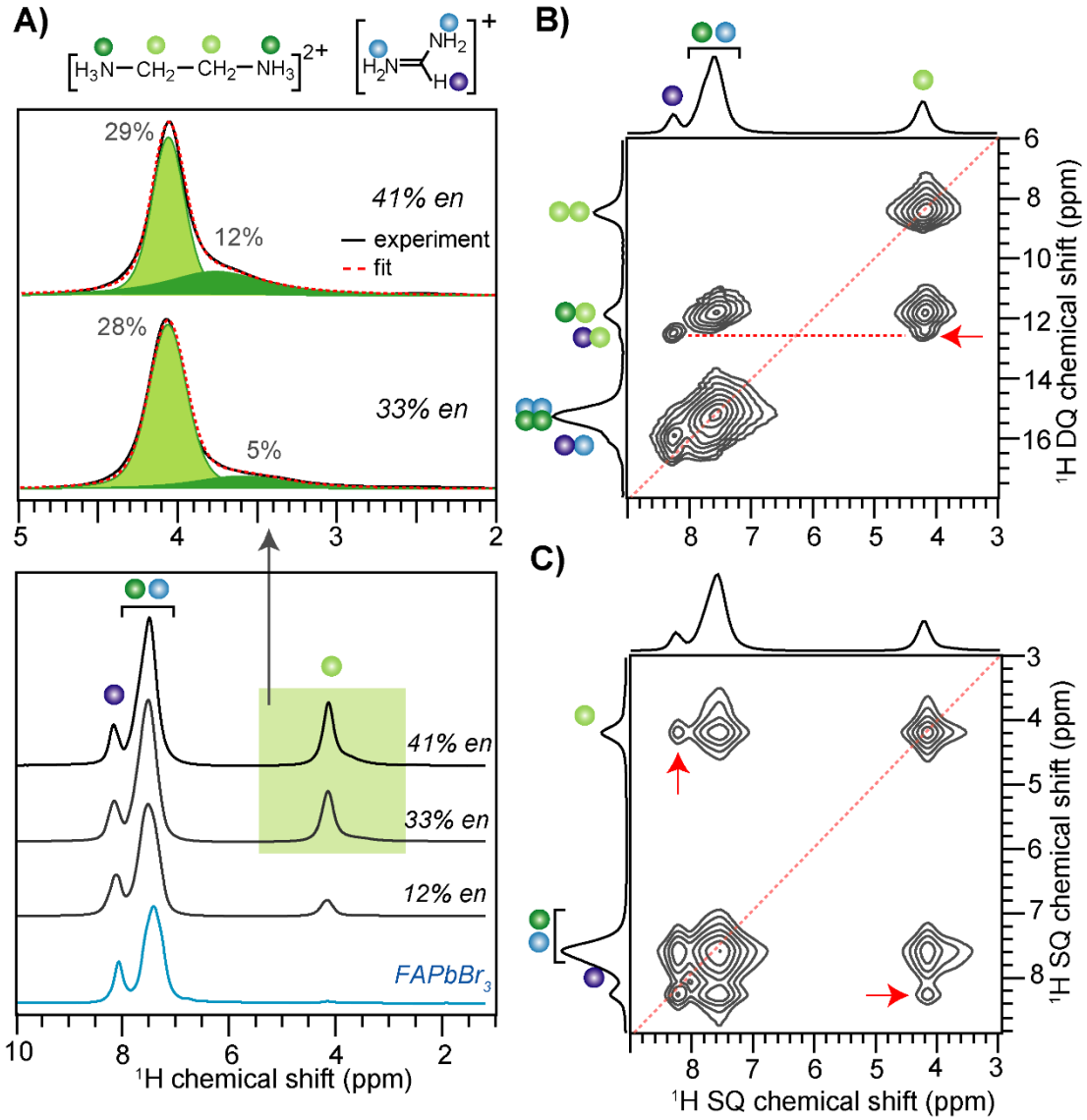

Figure 7. Solid-state ^{1}H MAS NMR spectra of $FAPbBr_3$ and hollow perovskites acquired of at 18.8 T (Larmor frequency of ^{1}H is 850.1 MHz) and at RT with 35 kHz MAS. A) Comparison of 1D ^{1}H MAS NMR spectra of $FAPbBr_3$, 12% *en*/$FAPbBr_3$, 33% *en*/$FAPbBr_3$ and 41% *en*/$FAPbBr_3$. Signals correspond to FA^{+} and en^{+} protons are depicted in color dots as shown in the Figure inset. B) 2D ^{1}H-^{1}H DQ-SQ correlation NMR spectra of 41% *en*/$FAPbBr_3$ using DQ excitation time of 28.6 µs. C) 2D ^{1}H-^{1}H SQ-SQ correlation NMR spectra of 41% *en*/$FAPbBr_3$ using spin diffusion mixing time of 100 ms.

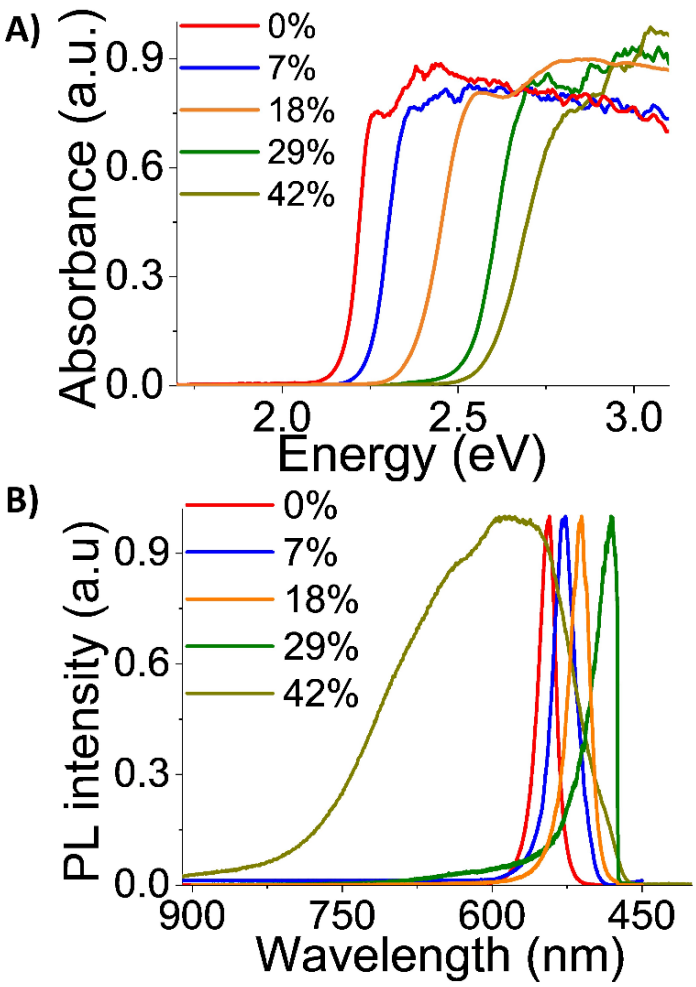

Figure 8. A) Optical absorption and B) emission spectra of compounds $(FA)_{1-x}(en)_x(Pb)_{1-0.7x}(Br)_{3-0.4x}$, with increasing amount of *en*.

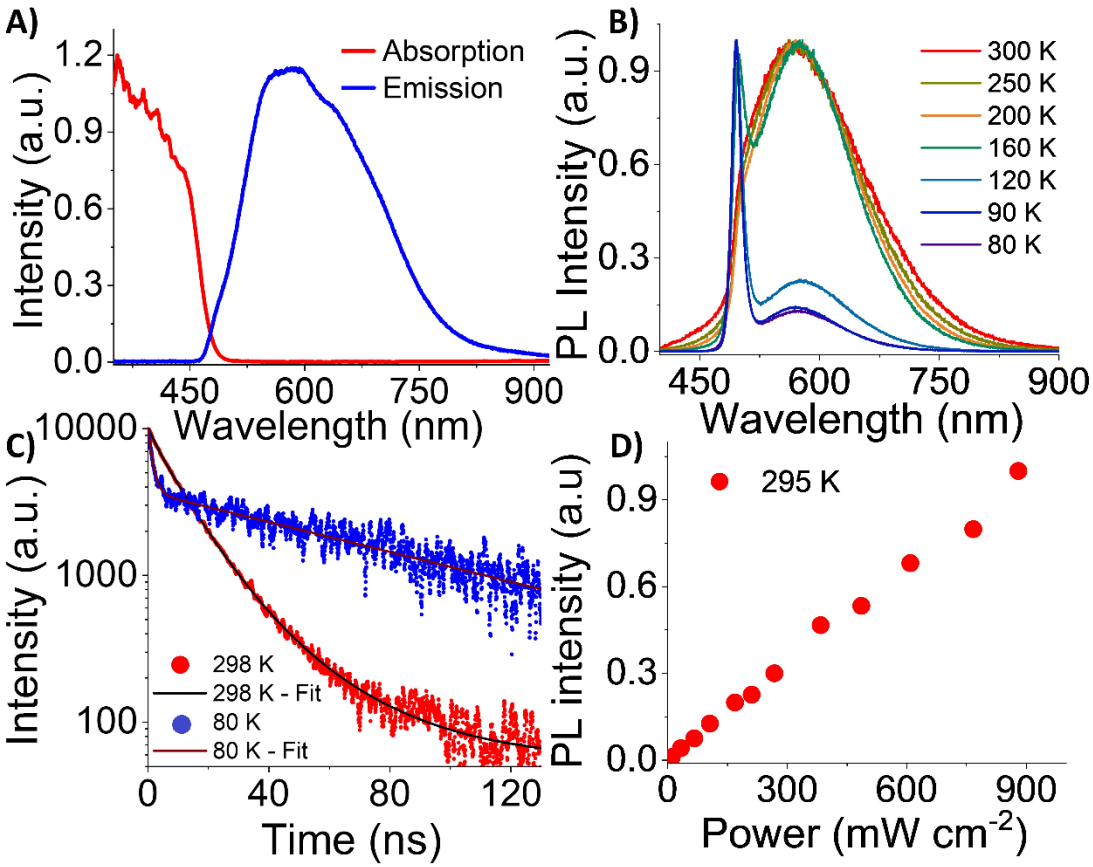

Figure 9. A) The recorded absorption and emission spectra of 42% *en*/$FAPbBr_3$ compound at RT, B) temperature dependent PL measurements from 300K to 80K (normalized), C) Time-resolved photoluminescence decay at 80K and 298K, D) Emission intensity versus excitation power, revealing the linear correlation of PL intensity with increasing power. The differences in the PL emission spectra at RT in A) and B) are ascribed to the different instrumentation set up and excitation wavelength used.

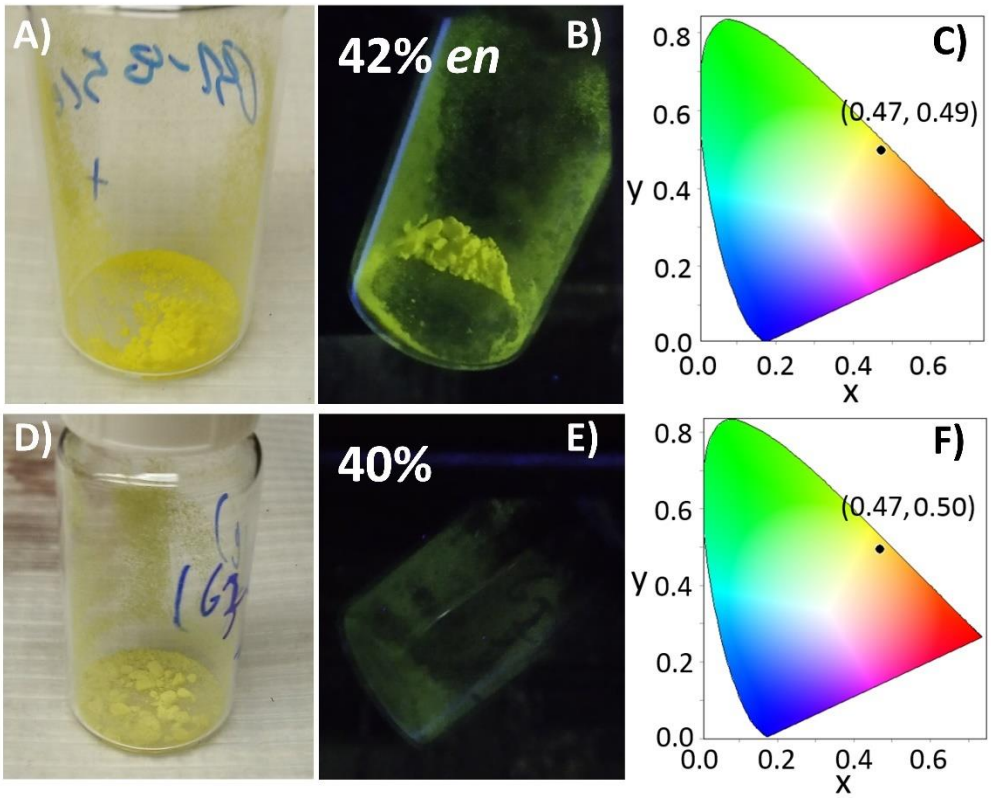

Figure 10. Photographs of dried polycrystalline solids of 42% *en*/$FAPbBr_3$ and 40% *en*/$FAPbBr_3$ samples, under ambient light A), D), and under UV light B), E) respectively. CIE chromaticity coordinates C) and F) for the corresponding compounds respectively.

Table 1. Crystal and Structure Refinement Data for $(FA)_{1-x}(en)_x(Pb)_{1-0.7x}(Br)_{3-0.4x}$ (x= 0%, 18%, 29%, 42%) at 293K.

Sample name	**α-$FAPbBr_3$**	**18% *en***	**29% *en***	**42% *en***
Temperature	293K	293K	293K	293K
Crystal system	cubic	cubic	cubic	cubic
Space group	*Pm*-3*m*	*Pm*-3*m*	*Pm*-3*m*	*Pm*-3*m*
Unit cell dimensions	a = 5.9926(3) Å, α = 90° b = 5.9926(3) Å, β = 90° c = 5.9926(3) Å, γ = 90°	a = 6.02320(10) Å, α = 90° b = 6.02320(10) Å, β = 90° c = 6.02320(10) Å, γ = 90°	a = 6.0594(2) Å, α = 90° b = 6.0594(2) Å, β = 90° c = 6.0594(2) Å, γ = 90°	a = 6.06400(10) Å, α = 90° b = 6.06400(10) Å, β = 90° c = 6.06400(10) Å, γ = 90°
Volume	215.202(19) $Å^3$	218.515(6) $Å^3$	222.479(13) $Å^3$	222.986(6) $Å^3$
Z	1	1	1	1
Density (calculated)	3.7574 g/cm^3	3.5729 g/cm^3	3.3631 g/cm^3	3.3177 g/cm^3
Independent reflections	86 [R_{int} = 0.0395]	95 [R_{int} = 0.0224]	105 [R_{int} = 0.0228]	90 [R_{int} = 0.0208]
Completeness to θ = 29.33°	98%	98%	97%	100%
Data / restraints / parameters	86 / 1 / 8	95 / 1 / 7	105 / 1 / 7	90 / 1 / 7
Goodness-of-fit	1.53	1.95	2.96	2.67
Final R indices [I>2σ(I)]	R_{obs} = 0.0223, wR_{obs} = 0.0513	R_{obs} = 0.0189, wR_{obs} = 0.0518	R_{obs} = 0.0251, wR_{obs} = 0.0715	R_{obs} = 0.0267, wR_{obs} = 0.0692
R indices [all data]	R_{all} = 0.0235, wR_{all} = 0.0516	R_{all} = 0.0189, wR_{all} = 0.0518	R_{all} = 0.0252, wR_{all} = 0.0715	R_{all} = 0.0267, wR_{all} = 0.0692
Largest diff. peak and hole	0.67 and -0.82 e·$Å^{-3}$	0.61 and -0.47 e·$Å^{-3}$	0.79 and -0.40 e·$Å^{-3}$	0.87 and -0.29 e·$Å^{-3}$

$R = \Sigma||F_o|-|F_c|| / \Sigma|F_o|$, $wR = (\Sigma[w(|F_o|^2 - |F_c|^2)^2] / \Sigma[w(|F_o|^4)])^{1/2}$ and $w=1/(\sigma^2(I)+0.0004I^2)$

Table 2. Comparison of the refined unit cell dimensions of $(FA)_{1-x}(en)_x(Pb)_{1-0.7x}(Br)_{3-0.4x}$ materials along with their determined band gaps. The increase of the *en* concentration leads to an increase to the unit cell dimensions and a blue shift of the band gap for all materials. The unit cell dimensions of the 7% *en* sample were determined from indexing of the PXRD patterns.

$FAPbBr_3$ + *en*%	**Unit cell parameters a (Å)**	**Unit cell Volume ($Å^3$)**	**Band gap (eV)**
0	5.9926(3)	215.202(19)	2.20
7	6.0046(2)	216.00(2)	2.25
18	6.02320(10)	218.515(6)	2.36
29	6.0594(2)	222.479(13)	2.54
42	6.06400(10)	222.986(6)	2.60

Table 3. Photophysical properties of bulk crystals of the 42% *en*/$FAPbBr_3$ compound. (τ_{av} is the average PL lifetime).

42% *en*/$FAPbBr_3$	**T(K)**	**PLQY (%)**	**τ_{av} (ns)**	**FWHM (nm)**	**CRI**	**CCT (K)**	**CIE**
Crystals	298K	1	15	195	67	3144	(0.47,0.49)

Table of Contents Graphic

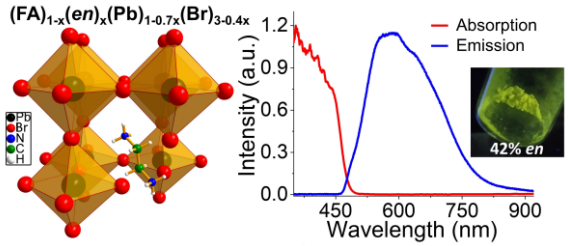

Supporting information

Tunable Broad Light Emission from 3D "Hollow" Bromide Perovskites through Defect Engineering

Ioannis Spanopoulos[1], Ido Hadar[1&], Weijun Ke[1§], Peijun Guo[2#], Eve M. Mozur,[3] Emily Morgan,[3] Shuxin Wang,[3] Ding Zheng,[1] Suyog Padgaonkar,[4] G. N. Manjunatha Reddy,[5] Emily A. Weiss,[4] Mark C. Hersam,[6] Ram Seshadri,[3] Richard D. Schaller[1], and Mercouri G. Kanatzidis*,[1]

[1]*Department of Chemistry, Northwestern University, Evanston, Illinois 60208, United States*
[2]*Center for Nanoscale Materials, Argonne National Laboratory, 9700 South Cass Avenue, Lemont, Illinois 60439, United States*
[3]*Materials Department and Materials Research Laboratory, University of California, Santa Barbara, California 93106, United States*
[4]*Department of Chemistry and the Materials Research Center, Applied Physics Program, and Department of Materials Science and Engineering and the Materials Research Center, Northwestern University, Evanston, Illinois 60208, United States*
[5]*Univ. Lille, CNRS, Centrale Lille Institut, Univ. Artois, UMR8181-UCCS-Unité de Catalyse et Chimie du Solide, F-59000 Lille, France.*
[6]*Department of Materials Science and Engineering, Department of Chemistry, Department of Electrical and Computer Engineering, and the Materials Research Center, Northwestern University, Evanston, Illinois 60208, United States*

Table of contents

1. Materials and methods

Starting materials

All starting materials for synthesis were purchased commercially and were used without further purification. Lead(II) acetate trihydrate puriss. p.a., ACS, 99.5-102.0%, Formamidine acetate 99%, Hypophosphorous acid solution 50 wt. % in H_2O, Hydrobromic acid ACS reagent, 48%, Ethylenediamine ReagentPlus®, ≥99% and Dimethyl sulfoxide-d_6 99.9 atom %D were purchased from Aldrich. Hollow $MAPbI_3$ and $FAPbI_3$ samples were prepared according to published procedures.[1]

Solution ^{1}H-NMR measurements

^{1}H NMR spectra were recorded on 500 MHz Bruker, X500 spectrometer. All samples were prepared by dissolving a small portion of the dried solids (~ 10 mg) in a DMSO-d_6 solution (0.5 mL). The actual amount of *en* (x) that resides in the crystal structure was determined by ^{1}H-NMR spectroscopy.

From NMR spectroscopy it was possible to calculate only the ratio between *en* and FA molecules. In order to find a way to quantify the amount of *en* relative to the FA we have introduced another equation that included the two molecules, namely:

$$FA + en = 1 \qquad \text{(eq. 1)}$$

This is consistent with the 113 (Cation)MX_3 (Cation= FA + *en*) perovskite formula. Since we have only two organic molecules in the structure, the total organic content should be equal to 1 (or 100%).

Solid state NMR measurements

Bulk crystals of $FAPbBr_3$ and hollow perovskites were separately packed into a 1.6 mm Phoenix rotor fitted with Vespel® caps. All 1D ^{1}H MAS and 2D ^{1}H-^{1}H correlation NMR experiments were carried out on a Bruker Avance Neo (18.8 T, ^{1}H Larmor frequency = 800.13 MHz) spectrometer using a Phoenix 1.6 mm H-X-Y probe. The nutation frequency for ^{1}H was 100 kHz, corresponding to a 90° pulse duration of 2.5 μs. The MAS frequency was 35 kHz. The ^{1}H spin-lattice relaxation times (T_1) for protons sites in FA^+ and en^+ cations were determined to be 3 s, based on inversion recovery measurements and analyses. 1D ^{1}H MAS NMR spectrum was acquired using 32 co-added transients using a relaxation delay of 3 s. In the case of 2D ^{1}H-^{1}H double-quantum(DQ)-single-quantum (SQ) NMR spectrum, the DQ coherences were excited using one rotor period ($1\tau_r$) Back-to-Back (BaBa) sequence, and reconverted using a 16-step phase cycle to choose $\Delta p = \pm 2$ on the DQ excitation pulses (4 steps) and $\Delta p = \pm 1$ (4 steps), where p is the coherence order. A rotor-synchronized t_1 increment of 28.6 μs was applied to acquire the indirect ^{1}H DQ dimension with 128 t_1 increments, each with 16 co-added transients, corresponding to a total experimental time of 5 h. 2D ^{1}H-^{1}H spin diffusion NMR spectra were acquired using different mixing times, 20, 100 and 500 ms. 2D spectra was acquired using 380 t_1 increments, each with 4 co-added transients. The ^{1}H chemical shifts were calibrated with respect to neat TMS using adamantane as an external reference (^{1}H resonance, 1.81 ppm).

XRD measurements

Single-crystal X-ray diffraction

Single crystal diffraction experiments were performed using a Bruker Molly instrument with MoKα IμS microfocus source (λ= 0.71073 Å) with MX Optics at 293 K. The collected data were integrated and applied with multiscan absorption correction using the APEX3 software. Additionally a four-circle Rigaku XtaLAB Synergy system equipped with a PhotonJet (Mo, λ= 0.71073 Å) micro-focus sealed X-ray tube and Hybrid Pixel Array Detector was utilized as well. The structure was solved by charge flipping and refined by full-matrix least squares on F^2 with the Jana2006 package.[2]

Powder X-ray diffraction

Powder X-ray diffraction patterns were collected on a Rigaku Miniflex system (CuKα radiation) operated at 40 kV and 15 mA. A typical scan rate was 20 sec/step with a step size of 0.02 deg. The data were manipulated with CMPR,[3] and Rietveld analysis was performed with the Jana2006 package.[2]

Variable Temperature high resolution Powder X-ray diffraction

High resolution variable Temperature Powder X-ray diffraction measurements were performed at APS Argonne National Lab, on beamline 11BM, with an average wavelength of 0.457850 Å. Discrete detectors covering an angular range from 0 to 4 2θ were scanned over a 25.5 2θ range, and data points were collected e very 0.001 2θ at a scan speed of 0.1/s. The data were manipulated with CMPR,[4] and Le Bail fit and Rietveld analysis were performed with the Jana2006 Package.[2] Total sctattering diffraction data were recorded on APS 11-ID-B beamline.

PDF analysis

Two dimensional total scattering data were integrated and masked using Fit2D.[5-6] Data were reduced and transformed to the PDF with PDFgetx3.[7] The PDF was modled in PDFgui as a cubic perovskite.[8] Electron density for formamidinium was approximated by a single atom with the analogous number of electrons. Thermal displacement parameters were refined according to the average symmetry (*Pm-3m*).

Optical Spectroscopy.

Optical diffuse-reflectance measurements were performed at room temperature using a Shimadzu UV-3600 PC double-beam, double-monochromator spectrophotometer operating from 200 to 2500 nm. $BaSO_4$ was used as a non-absorbing reflectance reference. The generated reflectance-versus-wavelength data were used to estimate the band gap of the material by converting reflectance to absorbance data according to the Kubelka−Munk equation: $\alpha/S = (1 - R)^2/2R$, where R is the reflectance and α and S are the absorption and scattering coefficients, respectively.[9]

PL/PLE/TRPL Measurements.

PL studies were perfomed using a Horiba LabRam Evolution high-resolution confocal Raman microscope spectrometer (600 g/mm diffraction grating) equipped with a diode continuous wave laser (473 nm, 25 mW) and a Synapse charge-coupled device camera. The maximum power output of the laser source was filtered to 1% of the maximum power output. PLE excitation-emission studies were perfomed using a Horiba Jobin-Yvon Nanolog spectrofluorometer and Synapse CCD. Temperature dependent PL measurements were performed using 405-nm diode laser (Picoquant) with the samples mounted in a liquid-nitrogen cooled cryostat (Janis, VPF-100). The PL signals were dispersed by a spectrograph and captured by an EMCCD (Princeton).

PLQY determination

PLQYs of powder samples were obtained on a Horiba FluoroMax-4 equipped with an integrating sphere using a 150 W continuous Xe arc lamp as excitation source at room temperature.

TGA measurements

The Thermogravimetric Analysis (TGA) measurements were performed on a Netzsch's Simultaneous Thermal Analysis (STA) system. An amount of ~15 mg of sample was placed inside an alumina cap and heated up to 700 ^oC under He flow with a heating rate of 8 ^oC/min. We must note here that if an aluminum cap is used instead (up to 600 ^0C), then the TGA curve is incomplete, as there is a significant amount of a residue left, possibly from the reaction of the perovskite with the metallic medium.[10-11]

SEM/EDX

Scanning Electron Microscopy (SEM) measurements were recorded on a high-resolution field emission Hitachi SU8030. A Hitachi S3400N-II instrument equipped with a PGT energy-dispersive X-ray analyser was used for the EDX measurements. Data were acquired with an accelerating voltage of 20 kV.

Density measurements

A Micromeritics AccuPyc II 1340 pycnometer was utilized for the density determination of all samples. An amount of 400 mg of dry sample was loaded to an aluminum cap (1 mL) and the volume determination was performed based on He displacement. Each sample was measured 3 times and the sample volume was recorded along with standard deviation. The average volume of each sample was used for the density calculations.

Photoemission yield spectroscopy in air (PYSA)

The energy level of the valence band maximum (VBM) was measured by Photoemission yield spectroscopy in air (PYSA, AC-2, Riken-Keiki). Briefly, the sample is scanned by tunable mono-chromatic ultraviolet light (UV, 4.2–6.2 eV), under ambient conditions and the number of generated photoelectrons are measured at each excitation energy. Photoelectrons are only generated when the photon energy is higher than the VBM. The VBM is determined by finding the onset of the PYSA spectra.

XRF studies

The composition of two samples with 0% *en* and 37% *en*, respectively, was studied by X-ray fluorescence (XRF) using a Rigaku ZSX Primus IV, which has a detection limit of 0.009% by mass. The relative amounts of Pb and Br were determined using the Pb Lα and Br Kα lines with a 15 s scan time and 15 s fixed angle measurement. Additionally, the Sn Kα line was used to confirm that the samples did not contain any Sn impurities.

2. Syntheses

Syntheses of $(FA)_{1-x}(en)_x(Pb)_{1-0.7x}(Br)_{3-0.4x}$ (x: 0%, 7%, 18%, 29%, 33%, 37%, 40%, 42%, 44%)

α-$FAPbBr_3$: 1137 mg (3 mmol) of $Pb(CH_3CO_2)_2 \cdot 3H_2O$ were dissolved in a solution consisting of 6 mL of 48% aqueous HBr, by heating under constant magnetic stirring. Then 312 mg (3 mmol) of formamidinium acetate were added to the hot colorless solution. Heating was discontinued and the sample was left to cool to RT directly. Orange crystals deposited after 10 min. They were collected by suction filtration and dried under vaccum overnight. Yield: 800 mg, (54% based on Pb)

x = 7%: 1137 mg (3 mmol) of $Pb(CH_3CO_2)_2 \cdot 3H_2O$ were dissolved in a 48% aqueous HBr solution (7 mL) by heating under constant magnetic stirring for about 5 minutes. Then 20 µL of ethylenediamine (0.3 mmol) were added to 50% aqueous H_3PO_2 (1 mL) at RT. This solution was added to the hot reaction solution. Subsequent addition of 312 mg (3 mmol) of formamidine acetate to the hot solution lead to the formation of light orange crystals. Stirring was continued for 5 min. They were collected by suction filtration and dried under vaccum overnight. Yield: 460 mg, (31% based on Pb)

x = 18%: 1137 mg (3 mmol) of $Pb(CH_3CO_2)_2 \cdot 3H_2O$ were dissolved in a 48% aqueous HBr solution (7 mL) by heating under constant magnetic stirring for about 5 minutes. Then 60 µL of ethylenediamine (0.9 mmol) were added to 50% aqueous H_3PO_2 (1 mL) at RT. This solution was added to the hot reaction solution. Subsequent addition of 312 mg (3 mmol) of formamidine acetate to the hot solution lead to the formation of dark yellow crystals. Stirring was continued for 5 min. They were collected by suction filtration and dried under vaccum overnight. Yield: 350 mg, (25% based on Pb

x = 29%: 1137 mg (3 mmol) of $Pb(CH_3CO_2)_2 \cdot 3H_2O$ were dissolved in a 48% aqueous HBr solution (7 mL) by heating under constant magnetic stirring for about 5 minutes. Then 100 µL of ethylenediamine (1.5 mmol) were added to 50% aqueous H_3PO_2 (1 mL) at RT. This solution was added to the hot reaction solution. Subsequent addition of 312 mg (3 mmol) of formamidine acetate to the hot solution lead to the formation of light yellow crystals. Stirring was continued for 5 min. They were collected by suction filtration and dried under vaccum overnight. Yield: 240 mg, (18% based on Pb)

x = 33%: 2274 mg (6 mmol) of $Pb(CH_3CO_2)_2 \cdot 3H_2O$ were dissolved in a 48% aqueous HBr solution (14 mL) by heating under constant magnetic stirring for about 5 minutes. Then 300 µL of ethylenediamine (4.5 mmol) were added to 50% aqueous H_3PO_2 (2 mL) at RT. This solution was added to the hot reaction solution. Subsequent addition of 624 mg (6 mmol) of formamidine acetate to the hot solution lead to the formation of light yellow crystals after 10 min. They were collected by suction filtration and dried under vaccum overnight. Yield: 600 mg, (22% based on Pb)

x = 37%: 2274 mg (6 mmol) of $Pb(CH_3CO_2)_2 \cdot 3H_2O$ were dissolved in a 48% aqueous HBr solution (14 mL) by heating under constant magnetic stirring for about 5 minutes. Then 340 µL of ethylenediamine (5.1 mmol) were added to 50% aqueous H_3PO_2 (2 mL) at RT. This solution was added to the hot reaction solution. Subsequent addition of 624 mg (6 mmol) of formamidine acetate to the hot solution lead to the formation of light yellow crystals after 10 min. They were collected by suction filtration and dried under vaccum overnight. Yield: 590 mg, (21% based on Pb)

x = 40%: 2274 mg (6 mmol) of $Pb(CH_3CO_2)_2 \cdot 3H_2O$ were dissolved in a 48% aqueous HBr solution (14 mL) by heating under constant magnetic stirring for about 5 minutes. Then 380 µL of ethylenediamine (5.7 mmol) were added to 50% aqueous H_3PO_2 (2 mL) at RT. This solution was added to the hot reaction solution. Subsequent addition of 624 mg (6 mmol) of formamidine acetate to the hot solution lead to the formation of light yellow crystals after 10 min. They were collected by suction filtration and dried under vaccum overnight. Yield: 590 mg, (21% based on Pb)

x = 42%: 1137 mg (3 mmol) of $Pb(CH_3CO_2)_2 \cdot 3H_2O$ were dissolved in a 48% aqueous HBr solution (7 mL) by heating under constant magnetic stirring for about 5 minutes. Then 200 µL of ethylenediamine (3 mmol) were added to 50% aqueous H_3PO_2 (1 mL) at RT. This solution was added to the hot reaction solution. Subsequent addition of 312 mg (3 mmol) of formamidine acetate to the hot solution lead to the formation of light yellow crystals. Stirring was continued for 5 min. They were collected by suction filtration and dried under vaccum overnight. Yield: 120 mg, (10% based on Pb)
x = 44%: 1137 mg (3 mmol) of $Pb(CH_3CO_2)_2 \cdot 3H_2O$ were dissolved in a 48% aqueous HBr solution (9 mL) by heating under constant magnetic stirring for about 5 minutes. Then 220 µL of ethylenediamine (3.3 mmol) were added to the reaction gradualy. Subsequent addition of 312 mg (3 mmol) of formamidine acetate to the hot solution lead to the formation of light yellow crystals. Stirring was continued for 5 min. They were collected by suction filtration and dried under vaccum overnight. Yield: 110 mg, (9% based on Pb)

Figure S1. Photograph of freshly precipitated perovskite crystals of $(FA)_{1-x}(en)_x(Pb)_{1-0.7x}(Br)_{3-0.4x}$, for x = 0%, 7%, 18%, 29% and 42% *en* respectively, starting from left to right.

3. Characterization
X-ray diffraction measurements

Table S1. Crystal data and structure refinement for $(en)_4Pb_2Br_9 \cdot 3Br^-$ at 293 K.

Empirical formula	C8 H40 Br12 N8 Pb2
Formula weight	1621.7
Temperature	293 K
Wavelength	0.71073 Å
Crystal system	monoclinic
Space group	$P2_1/n$
Unit cell dimensions	a = 8.9295(2) Å, α = 90° b = 27.8031(7) Å, β = 101.968(3)° c = 14.7492(4) Å, γ = 90°
Volume	3582.16(16) $Å^3$
Z	4
Density (calculated)	3.007 g/cm^3
Absorption coefficient	22.788 mm^{-1}
F(000)	2912
θ range for data collection	2.03 to 31.03°
Index ranges	-11<=h<=12, -36<=k<=37, -18<=l<=20
Reflections collected	60716
Independent reflections	9747 [R_{int} = 0.0693]
Completeness to θ = 28.57°	98%
Refinement method	Full-matrix least-squares on F^2
Data / restraints / parameters	9747 / 0 / 194
Goodness-of-fit	1.75
Final R indices [I>2σ(I)]	R_{obs} = 0.0668, wR_{obs} = 0.0856
R indices [all data]	R_{all} = 0.1006, wR_{all} = 0.0893
Extinction coefficient	-
Largest diff. peak and hole	3.37 and -2.70 e·$Å^{-3}$

$R = \Sigma||F_o|-|F_c|| / \Sigma|F_o|$, $wR = \{\Sigma[w(|F_o|^2 - |F_c|^2)^2] / \Sigma[w(|F_o|^4)]\}^{1/2}$ and $w=1/(\sigma^2(I)+0.0004I^2)$

Crystallographic tables

1. Structure: (*en*)$_4$Pb$_2$Br$_9$·3Br$^-$

Table S2. Atomic coordinates (x10^4) and equivalent isotropic displacement parameters (Å^{2}x10^3) for *(en)*$_4$Pb$_2$Br$_9$·3Br$^-$ at 293 K with estimated standard deviations in parentheses.

Label	x	y	z	Occupancy	U_{eq}*
Pb(1)	7897(1)	522(1)	984(1)	1	25(1)
Pb(2)	1549(1)	6844(1)	2388(1)	1	25(1)
Br(1)	-1062(1)	7446(1)	1578(1)	1	33(1)
Br(2)	3777(1)	2349(1)	800(1)	1	37(1)
Br(3)	989(2)	6318(1)	634(1)	1	39(1)
Br(4)	7723(1)	3481(1)	1813(1)	1	35(1)
Br(5)	3894(2)	7464(1)	1865(1)	1	41(1)
Br(6)	2194(2)	4880(1)	-47(1)	1	45(1)
Br(7)	2930(2)	3687(1)	1578(1)	1	42(1)
Br(8)	7451(1)	1206(1)	-616(1)	1	41(1)
Br(9)	5000	0	0	1	49(1)
Br(10)	8837(2)	-180(1)	2516(1)	1	48(1)
Br(11)	615(2)	1149(1)	1879(1)	1	46(1)
Br(12)	10000	0	0	1	62(1)
Br(13)	5942(2)	1123(1)	2075(1)	1	53(1)
N(1)	5392(9)	4244(3)	376(5)	1	39(2)
N(2)	38(9)	4392(3)	1521(6)	1	49(2)
N(3)	331(8)	2797(3)	891(5)	1	40(2)
N(4)	6040(8)	8371(2)	936(5)	1	37(2)
N(5)	9438(8)	8740(3)	1540(5)	1	40(2)
N(6)	-2352(9)	2242(3)	1563(6)	1	49(2)
N(7)	2772(10)	3588(3)	-638(6)	1	55(2)
C(1)	5100(10)	4070(3)	-582(6)	1	38(2)
C(2)	-2183(10)	2359(3)	620(6)	1	35(2)
C(3)	-544(10)	2361(3)	516(6)	1	36(2)
C(4)	364(12)	4645(4)	2419(8)	1	61(3)
C(5)	8423(10)	8726(3)	611(7)	1	40(2)
C(6)	6765(10)	8798(3)	611(6)	1	40(2)
C(7)	4367(12)	3584(4)	-713(7)	1	56(3)
C(8)	1763(17)	4945(5)	2614(11)	1	91(4)
N(8)	1853(18)	5304(6)	2056(11)	1	144(5)

H(1n1)	5784.81	4531.65	399.78	1	46.7
H(2n1)	4535.89	4253.78	569.03	1	46.7
H(3n1)	6028.56	4051.5	726.61	1	46.7
H(1n2)	-586.66	4154.36	1545.69	1	58.3
H(2n2)	-378.28	4590.88	1086.56	1	58.3
H(3n2)	887.69	4280.97	1401.56	1	58.3
H(1n3)	1259.99	2777.02	798.07	1	48.1
H(2n3)	-111.97	3051.34	612.4	1	48.1
H(3n3)	358.6	2818.91	1482.77	1	48.1
H(1n4)	5084.48	8433.2	933.97	1	44.6
H(2n4)	6095.16	8129.24	569.73	1	44.6
H(3n4)	6513.96	8298.7	1496.53	1	44.6
H(1n5)	10333.55	8627.41	1508.3	1	48.2
H(2n5)	9531.72	9036.07	1737.62	1	48.2
H(3n5)	9044.46	8566.34	1922.38	1	48.2
H(1n6)	-3242.95	2338.9	1641.43	1	58.6
H(2n6)	-2278.9	1932.07	1645.46	1	58.6
H(3n6)	-1635.51	2384.39	1962.09	1	58.6
H(1n7)	2443.84	3294.19	-624.99	1	66.5
H(2n7)	2685.21	3735.51	-130.68	1	66.5
H(3n7)	2229.62	3737.88	-1112.54	1	66.5
H(1n8)	2716.43	5287.91	1871.73	1	173
H(2n8)	1097.15	5288.06	1578.58	1	173
H(3n8)	1806.71	5573.61	2347	1	173
H(1c1)	6041.68	4064.89	-799.03	1	45.2
H(2c1)	4472.74	4297.91	-978.4	1	45.2
H(1c2)	-2634.76	2667.89	445.41	1	41.4
H(2c2)	-2757.06	2134.06	190.97	1	41.4
H(1c3)	-33.71	2080.32	806.33	1	43.1
H(2c3)	-508.03	2324.14	-126.58	1	43.1
H(1c4)	397.6	4416.25	2911.21	1	72.8
H(2c4)	-504.06	4836.85	2477.37	1	72.8
H(1c5)	8557.16	8426.1	315.79	1	47.4
H(2c5)	8749.7	8963.49	220.54	1	47.4
H(1c6)	6227.99	8881.68	-1.53	1	48.5
H(2c6)	6648.13	9069.39	992.84	1	48.5
H(1c7)	4447.36	3458.16	-1307.68	1	67

H(2c7)	4928.23	3364.25	-265.98	1	67
H(1c8)	1932.62	5059.97	3240.5	1	109.3
H(2c8)	2647.86	4742.91	2659.72	1	109.3

*U_{eq} is defined as one third of the trace of the orthogonalized U_{ij} tensor.

Table S3. Anisotropic displacement parameters ($Å^2x10^3$) for *(en)*$_4Pb_2Br_9 \cdot 3Br^-$ at 293 K with estimated standard deviations in parentheses.

Label	U_{11}	U_{22}	U_{33}	U_{12}	U_{13}	U_{23}
Pb(1)	25(1)	23(1)	27(1)	0(1)	7(1)	-2(1)
Pb(2)	22(1)	31(1)	22(1)	2(1)	3(1)	2(1)
Br(1)	33(1)	37(1)	29(1)	10(1)	6(1)	5(1)
Br(2)	32(1)	50(1)	28(1)	6(1)	4(1)	-1(1)
Br(3)	41(1)	43(1)	31(1)	8(1)	4(1)	-5(1)
Br(4)	39(1)	34(1)	33(1)	4(1)	13(1)	2(1)
Br(5)	42(1)	44(1)	35(1)	-11(1)	5(1)	7(1)
Br(6)	39(1)	38(1)	62(1)	7(1)	22(1)	15(1)
Br(7)	36(1)	55(1)	33(1)	-4(1)	2(1)	3(1)
Br(8)	30(1)	48(1)	47(1)	7(1)	13(1)	19(1)
Br(9)	41(1)	37(1)	62(1)	-12(1)	-8(1)	4(1)
Br(10)	65(1)	40(1)	38(1)	10(1)	9(1)	12(1)
Br(11)	47(1)	41(1)	43(1)	-14(1)	-5(1)	-1(1)
Br(12)	65(2)	51(1)	84(2)	15(1)	46(1)	-11(1)
Br(13)	55(1)	53(1)	54(1)	16(1)	18(1)	-12(1)

The anisotropic displacement factor exponent takes the form: $-2\pi^2[h^2a^{*2}U_{11} + ... + 2hka^*b^*U_{12}]$.

Table S4. Bond lengths [Å] for *(en)*$_4$Pb$_2$Br$_9$·3Br$^-$ at 293 K with estimated standard deviations in parentheses.

Label	Distances
Pb(1)-Br(8)	2.9941(10)
Pb(1)-Br(9)	3.0569(3)
Pb(1)-Br(10)	2.9706(10)
Pb(1)-Br(11)#1	3.0571(10)
Pb(1)-Br(12)	2.9773(4)
Pb(1)-Br(13)	3.0990(12)
Pb(2)-Br(1)	2.9185(9)
Pb(2)-Br(2)#2	3.0869(10)
Pb(2)-Br(3)	2.9231(10)
Pb(2)-Br(5)	2.9363(11)
Br(1)-N(6)#3	3.384(9)
Br(1)-N(7)#4	3.413(8)
Br(2)-N(3)	3.348(8)
Br(2)-N(4)#5	3.281(8)
Br(2)-N(6)#1	3.419(8)
Br(3)-N(3)#4	3.377(7)
Br(3)-N(7)#4	3.369(9)
Br(3)-N(8)	3.503(16)
Br(4)-N(1)	3.392(7)
Br(4)-N(2)#1	3.353(8)
Br(4)-N(3)#1	3.493(8)
Br(4)-N(4)#6	3.288(7)
Br(4)-N(5)#6	3.476(8)
Br(4)-N(6)#1	3.465(8)
Br(5)-N(3)#2	3.367(8)
Br(5)-N(6)#2	3.510(7)
Br(6)-N(1)	3.306(8)
Br(6)-N(1)#5	3.353(8)
Br(6)-N(2)	3.570(9)
Br(6)-N(2)#4	3.317(8)
Br(6)-N(8)	3.390(17)
Br(7)-N(1)	3.464(8)
Br(7)-N(2)	3.229(8)
Br(7)-N(3)	3.398(7)

Br(7)-N(5)#6	3.247(7)
Br(7)-N(7)	3.253(10)
Br(8)-N(4)#5	3.273(7)
Br(8)-N(5)#7	3.342(8)
Br(10)-N(1)#6	3.439(7)
Br(10)-N(5)#8	3.419(8)
Br(11)-N(8)#9	3.410(15)
Br(13)-N(7)#10	3.522(9)
N(1)-C(1)	1.465(12)
N(1)-H(1n1)	0.87
N(1)-H(2n1)	0.87
N(1)-H(3n1)	0.87
N(2)-C(4)	1.474(14)
N(2)-H(1n2)	0.87
N(2)-H(2n2)	0.87
N(2)-H(3n2)	0.87
N(3)-C(3)	1.486(11)
N(3)-H(1n3)	0.87
N(3)-H(2n3)	0.87
N(3)-H(3n3)	0.87
N(4)-C(6)	1.479(12)
N(4)-H(1n4)	0.87
N(4)-H(2n4)	0.87
N(4)-H(3n4)	0.87
N(5)-C(5)	1.479(11)
N(5)-H(1n5)	0.87
N(5)-H(2n5)	0.87
N(5)-H(3n5)	0.87
N(6)-C(2)	1.467(13)
N(6)-H(1n6)	0.87
N(6)-H(2n6)	0.87
N(6)-H(3n6)	0.87
N(7)-C(7)	1.452(14)
N(7)-H(1n7)	0.87
N(7)-H(2n7)	0.87
N(7)-H(3n7)	0.87
C(1)-C(7)	1.497(13)

C(1)-H(1c1)	0.96
C(1)-H(2c1)	0.96
C(2)-C(3)	1.503(13)

Symmetry transformations used to generate equivalent atoms:

(1) x+1,y,z (2) -x+1/2,y+1/2,-z+1/2 (3) -x-1/2,y+1/2,-z+1/2 (4) -x,-y+1,-z (5) -x+1,-y+1,-z (6) -x+3/2,y-1/2,-z+1/2 (7) -x+2,-y+1,-z (8) x,y-1,z (9) -x+1/2,y-1/2,-z+1/2 (10) x+1/2,-y+1/2,z+1/2 (11) x-1,y,z (12) -x+3/2,y+1/2,-z+1/2 (13) x,y+1,z (14) -x-1/2,y-1/2,-z+1/2 (15) x-1/2,-y+1/2,z-1/2 (16) -x+1,-y,-z (17) -x+2,-y,-z

Table S5. Bond angles [°] for *(en)*$_4$Pb$_2$Br$_9$·3Br$^-$ at 293 K with estimated standard deviations in parentheses.

Label	Angles
Br(8)-Pb(1)-Br(9)	88.070(18)
Br(8)-Pb(1)-Br(10)	170.89(3)
Br(8)-Pb(1)-Br(11)#1	86.67(3)
Br(8)-Pb(1)-Br(12)	85.41(2)
Br(8)-Pb(1)-Br(13)	93.95(3)
Br(9)-Pb(1)-Br(10)	97.32(2)
Br(9)-Pb(1)-Br(11)#1	173.51(2)
Br(9)-Pb(1)-Br(12)	95.438(9)
Br(9)-Pb(1)-Br(13)	89.44(2)
Br(10)-Pb(1)-Br(11)#1	88.39(3)
Br(10)-Pb(1)-Br(12)	86.77(2)
Br(10)-Pb(1)-Br(13)	93.44(3)
Br(11)#1-Pb(1)-Br(12)	87.93(2)
Br(11)#1-Pb(1)-Br(13)	87.13(3)
Br(12)-Pb(1)-Br(13)	175.05(2)
Br(1)-Pb(2)-Br(2)#2	83.22(3)
Br(1)-Pb(2)-Br(3)	87.11(3)
Br(1)-Pb(2)-Br(5)	96.20(3)
Br(2)#2-Pb(2)-Br(3)	164.71(3)
Br(2)#2-Pb(2)-Br(5)	99.22(3)
Br(3)-Pb(2)-Br(5)	93.55(3)
Pb(2)-Br(1)-N(6)#3	90.28(13)
Pb(2)-Br(1)-N(7)#4	86.24(14)
N(6)#3-Br(1)-N(7)#4	87.7(2)
Pb(2)#9-Br(2)-N(3)	83.23(14)
Pb(2)#9-Br(2)-N(4)#5	115.26(13)
Pb(2)#9-Br(2)-N(6)#1	86.87(15)
N(3)-Br(2)-N(4)#5	116.96(17)
N(3)-Br(2)-N(6)#1	153.38(19)
N(4)#5-Br(2)-N(6)#1	89.61(19)
Pb(2)-Br(3)-N(3)#4	101.36(13)

Symmetry transformations used to generate equivalent atoms:

(1) x+1,y,z (2) -x+1/2,y+1/2,-z+1/2 (3) -x-1/2,y+1/2,-z+1/2 (4) -x,-y+1,-z (5) -x+1,-y+1,-z (6) -x+3/2,y-1/2,-z+1/2 (7) -x+2,-y+1,-z (8) x,y-1,z (9) -x+1/2,y-1/2,-z+1/2 (10) x+1/2,-

y+1/2,z+1/2 (11) x-1,y,z (12) -x+3/2,y+1/2,-z+1/2 (13) x,y+1,z (14) -x-1/2,y-1/2,-z+1/2 (15) x-1/2,-y+1/2,z-1/2 (16) -x+1,-y,-z (17) -x+2,-y,-z

2. Structure: α-$FAPbBr_3$

Table S6. Atomic coordinates ($x10^4$) and equivalent isotropic displacement parameters ($Å^2x10^3$) for α-$FAPbBr_3$ at 293 K with estimated standard deviations in parentheses.

Label	x	y	z	Occupancy	U_{eq}^*
Pb	5000	5000	5000	1	34(1)
Br	5000	5000	10000	1	80(1)
C	0	10000	10000	1	120(20)
N	0	7831(3)	10000	0.3336	130(20)

*U_{eq} is defined as one third of the trace of the orthogonalized U_{ij} tensor.

Table S7. Anisotropic displacement parameters ($Å^2x10^3$) for α-$FAPbBr_3$ at 293 K with estimated standard deviations in parentheses.

Label	U_{11}	U_{22}	U_{33}	U_{12}	U_{13}	U_{23}
Pb	34(1)	34(1)	34(1)	0	0	0
Br	106(2)	106(2)	30(1)	0	0	0

The anisotropic displacement factor exponent takes the form: $-2\pi^2[h^2a^{*2}U_{11} + ... + 2hka^*b^*U_{12}]$.

Table S8. Bond lengths [Å] for α-$FAPbBr_3$ at 293 K with estimated standard deviations in parentheses.

Label	Distances
Pb-Br#1	2.9963(3)
Pb-Br	2.9963(3)
Pb-Br#2	2.9963(3)
Pb-Br#3	2.9963(3)
Pb-Br#4	2.9963(3)
Pb-Br#5	2.9963(3)
Br-N#6	3.4432(8)
Br-N#7	3.4432(8)
Br-N#8	3.4432(8)
Br-N#9	3.4432(8)
Br-N#10	3.4432(8)
Br-N#11	3.4432(8)
Br-N#12	3.4432(8)
C-N#13	1.2998(15)
C-N#14	1.2998(15)
C-N#15	1.2998(15)
C-N#16	1.2998(15)
C-N#12	1.2998(15)

Symmetry transformations used to generate equivalent atoms:

(1) x,y,z-1 (2) z-1,x,y (3) z,x,y (4) y,z-1,x (5) y,z,x (6) x+1,y,z (7) -x,-y+1,z (8) -x+1,-y+1,z (9) y,z-1,x+1 (10) y,z,x+1 (11) -y+1,z-1,-x+1 (12) -y+1,z,-x+1 (13) -x,-y+2,z (14) z-1,x+1,y (15) z-1,-x+1,-y+2 (16) y-1,z,x+1 (17) x,y,z+1 (18) x-1,y,z (19) z-1,x,y+1

Table S9. Bond angles [°] for α-$FAPbBr_3$ at 293 K with estimated standard deviations in parentheses.

Label	Angles
Br#1-Pb-Br	180
Br#1-Pb-Br#2	90
Br#1-Pb-Br#3	90
Br#1-Pb-Br#4	90
Br#1-Pb-Br#5	90
Br-Pb-Br#2	90
Br-Pb-Br#3	90
Br-Pb-Br#4	90
Br-Pb-Br#5	90
Br#2-Pb-Br#3	180
Br#2-Pb-Br#4	90
Br#2-Pb-Br#5	90
Br#3-Pb-Br#4	90
Br#3-Pb-Br#5	90
Br#4-Pb-Br#5	180
Pb-Br-Pb#17	180
Pb-Br-N	90
Pb-Br-N#6	90
Pb-Br-N#7	90
Pb-Br-N#8	90
Pb-Br-N#9	90
Pb-Br-N#10	90
Pb-Br-N#11	90

Symmetry transformations used to generate equivalent atoms:

(1) x,y,z-1 (2) z-1,x,y (3) z,x,y (4) y,z-1,x (5) y,z,x (6) x+1,y,z (7) -x,-y+1,z (8) -x+1,-y+1,z (9) y,z-1,x+1 (10) y,z,x+1 (11) -y+1,z-1,-x+1 (12) -y+1,z,-x+1 (13) -x,-y+2,z (14) z-1,x+1,y (15) z-1,-x+1,-y+2 (16) y-1,z,x+1 (17) x,y,z+1 (18) x-1,y,z (19) z-1,x,y+1

3. Structure: 18% *en*/$FAPbBr_3$

Table S10. Atomic coordinates ($x10^4$) and equivalent isotropic displacement parameters ($Å^2x10^3$) for 18% *en*/$FAPbBr_3$ at 293 K with estimated standard deviations in parentheses.

Label	x	y	z	Occupancy	U_{eq}^*
Pb	5000	5000	5000	0.9194	47(1)
Br	5000	5000	0	1	100(1)
C	0	10000	10000	1	150(20)
N	0	7843(3)	10000	0.3336	160(20)

*U_{eq} is defined as one third of the trace of the orthogonalized U_{ij} tensor.

Table S11. Anisotropic displacement parameters ($Å^2x10^3$) for 18% *en*/$FAPbBr_3$ at 293 K with estimated standard deviations in parentheses.

Label	U_{11}	U_{22}	U_{33}	U_{12}	U_{13}	U_{23}
Pb	47(1)	47(1)	47(1)	0	0	0
Br	125(1)	125(1)	48(1)	0	0	0

The anisotropic displacement factor exponent takes the form: $-2\pi^2[h^2a^{*2}U_{11} + ... + 2hka^*b^*U_{12}]$.

Table S12. Bond lengths [Å] for 18% *en*/$FAPbBr_3$ at 293 K with estimated standard deviations in parentheses.

Label	Distances
Pb-Br	3.01160(10)
Pb-Br#1	3.01160(10)
Pb-Br#2	3.01160(10)
Pb-Br#3	3.01160(10)
Pb-Br#4	3.01160(10)
Pb-Br#5	3.01160(10)
Br-N#6	3.4643(10)
Br-N#7	3.4643(10)
Br-N#8	3.4643(10)
Br-N#9	3.4643(10)
Br-N#10	3.4643(10)
Br-N#4	3.4643(10)
Br-N#11	3.4643(10)
Br-N#12	3.4643(10)
C-N	1.299(2)
C-N#13	1.299(2)
C-N#14	1.299(2)
C-N#15	1.299(2)
C-N#16	1.299(2)
C-N#17	1.299(2)

Symmetry transformations used to generate equivalent atoms:
(1) x,y,z+1 (2) z,x,y (3) z+1,x,y (4) y,z,x (5) y,z+1,x (6) x,y,z-1 (7) x+1,y,z-1 (8) -x,-y+1,z-1 (9) -x+1,-y+1,z-1 (10) y,z-1,x (11) -y+1,z-1,-x (12) -y+1,z,-x (13) -x,-y+2,z (14) z-1,x+1,y (15) z-1,-x+1,-y+2 (16) y-1,z,x+1 (17) -y+1,z,-x+1 (18) x-1,y,z+1 (19) z,x,y+1

Table S13. Bond angles [°] for 18% *en*/$FAPbBr_3$ at 293 K with estimated standard deviations in parentheses.

Label	Angles
Br-Pb-Br#1	180
Br-Pb-Br#2	90
Br-Pb-Br#3	90
Br-Pb-Br#4	90
Br-Pb-Br#5	90
Br#1-Pb-Br#2	90
Br#1-Pb-Br#3	90
Br#1-Pb-Br#4	90
Br#1-Pb-Br#5	90
Br#2-Pb-Br#3	180
Br#2-Pb-Br#4	90
Br#2-Pb-Br#5	90
Br#3-Pb-Br#4	90
Br#3-Pb-Br#5	90
Br#4-Pb-Br#5	180
Pb#6-Br-Pb	180
Pb#6-Br-N#6	90
Pb#6-Br-N#7	90

Symmetry transformations used to generate equivalent atoms:
(1) x,y,z+1 (2) z,x,y (3) z+1,x,y (4) y,z,x (5) y,z+1,x (6) x,y,z-1 (7) x+1,y,z-1 (8) -x,-y+1,z-1 (9) -x+1,-y+1,z-1 (10) y,z-1,x (11) -y+1,z-1,-x (12) -y+1,z,-x (13) -x,-y+2,z (14) z-1,x+1,y (15) z-1,-x+1,-y+2 (16) y-1,z,x+1 (17) -y+1,z,-x+1 (18) x-1,y,z+1 (19) z,x,y+1

4. Structure: 29% *en*/$FAPbBr_3$

Table S14. Atomic coordinates ($x10^4$) and equivalent isotropic displacement parameters ($Å^2x10^3$) for 29% *en*/$FAPbBr_3$ at 293 K with estimated standard deviations in parentheses.

Label	x	y	z	Occupancy	U_{eq}^*
Pb(1)	5000	5000	5000	0.8256	57(1)
Br(1)	5000	5000	0	0.9986	120(1)
C(1)	0	10000	10000	1	210(30)
N(1)	0	7856(5)	10000	0.3336	180(30)

$^*U_{eq}$ is defined as one third of the trace of the orthogonalized U_{ij} tensor.

Table S15. Anisotropic displacement parameters ($Å^2x10^3$) for 29% *en*/$FAPbBr_3$ at 293 K with estimated standard deviations in parentheses.

Label	U_{11}	U_{22}	U_{33}	U_{12}	U_{13}	U_{23}
Pb(1)	57(1)	57(1)	57(1)	0	0	0
Br(1)	148(2)	148(2)	63(1)	0	0	0

The anisotropic displacement factor exponent takes the form: $-2\pi^2[h^2a^{*2}U_{11} + ... + 2hka^*b^*U_{12}]$.

Table S16. Bond lengths [Å] for 29% *en*/$FAPbBr_3$ at 293 K with estimated standard deviations in parentheses.

Label	Distances
Pb(1)-Br(1)	3.0297(2)
Pb(1)-Br(1)#1	3.0297(2)
Pb(1)-Br(1)#2	3.0297(2)
Pb(1)-Br(1)#3	3.0297(2)
Pb(1)-Br(1)#4	3.0297(2)
Pb(1)-Br(1)#5	3.0297(2)
Br(1)-N(1)#6	3.4890(15)
Br(1)-N(1)#7	3.4890(15)
Br(1)-N(1)#8	3.4890(15)
Br(1)-N(1)#9	3.4890(15)
Br(1)-N(1)#10	3.4890(15)
Br(1)-N(1)#4	3.4890(15)
Br(1)-N(1)#11	3.4890(15)
Br(1)-N(1)#12	3.4890(15)
C(1)-N(1)	1.299(3)
C(1)-N(1)#13	1.299(3)
C(1)-N(1)#14	1.299(3)
C(1)-N(1)#15	1.299(3)
C(1)-N(1)#16	1.299(3)
C(1)-N(1)#17	1.299(3)

Symmetry transformations used to generate equivalent atoms:

(1) x,y,z+1 (2) z,x,y (3) z+1,x,y (4) y,z,x (5) y,z+1,x (6) x,y,z-1 (7) x+1,y,z-1 (8) -x,-y+1,z-1 (9) -x+1,-y+1,z-1 (10) y,z-1,x (11) -y+1,z-1,-x (12) -y+1,z,-x (13) -x,-y+2,z (14) z-1,x+1,y (15) z-1,-x+1,-y+2 (16) y-1,z,x+1 (17) -y+1,z,-x+1 (18) x-1,y,z+1 (19) z,x,y+1

Table S17. Bond angles [°] for 29% *en*/$FAPbBr_3$ at 293 K with estimated standard deviations in parentheses.

Label	Angles
Br(1)-Pb(1)-Br(1)#1	180
Br(1)-Pb(1)-Br(1)#2	90
Br(1)-Pb(1)-Br(1)#3	90
Br(1)-Pb(1)-Br(1)#4	90
Br(1)-Pb(1)-Br(1)#5	90
Br(1)#1-Pb(1)-Br(1)#2	90
Br(1)#1-Pb(1)-Br(1)#3	90
Br(1)#1-Pb(1)-Br(1)#4	90
Br(1)#1-Pb(1)-Br(1)#5	90
Br(1)#2-Pb(1)-Br(1)#3	180
Br(1)#2-Pb(1)-Br(1)#4	90
Br(1)#2-Pb(1)-Br(1)#5	90
Br(1)#3-Pb(1)-Br(1)#4	90
Br(1)#3-Pb(1)-Br(1)#5	90
Br(1)#4-Pb(1)-Br(1)#5	180
Pb(1)#6-Br(1)-Pb(1)	180

Symmetry transformations used to generate equivalent atoms:

(1) x,y,z+1 (2) z,x,y (3) z+1,x,y (4) y,z,x (5) y,z+1,x (6) x,y,z-1 (7) x+1,y,z-1 (8) -x,-y+1,z-1 (9) -x+1,-y+1,z-1 (10) y,z-1,x (11) -y+1,z-1,-x (12) -y+1,z,-x (13) -x,-y+2,z (14) z-1,x+1,y (15) z-1,-x+1,-y+2 (16) y-1,z,x+1 (17) -y+1,z,-x+1 (18) x-1,y,z+1 (19) z,x,y+1

5. Structure: 42% *en*/$FAPbBr_3$

Table S18. Atomic coordinates ($x10^4$) and equivalent isotropic displacement parameters ($Å^2x10^3$) for 42% *en*/$FAPbBr_3$ at 293 K with estimated standard deviations in parentheses.

Label	x	y	z	Occupancy	U_{eq}^*
Pb	5000	5000	5000	0.8051	64(1)
Br	5000	5000	0	0.9956	132(1)
C	0	10000	10000	1	220(40)
N	0	7857(4)	10000	0.3336	210(40)

*U_{eq} is defined as one third of the trace of the orthogonalized U_{ij} tensor.

Table S19. Anisotropic displacement parameters ($Å^2x10^3$) for 42% *en*/$FAPbBr_3$ at 293 K with estimated standard deviations in parentheses.

Label	U_{11}	U_{22}	U_{33}	U_{12}	U_{13}	U_{23}
Pb	64(1)	64(1)	64(1)	0	0	0
Br	162(2)	162(2)	71(2)	0	0	0

The anisotropic displacement factor exponent takes the form: $-2\pi^2[h^2a^{*2}U_{11} + ... + 2hka^*b^*U_{12}]$.

Table S20. Bond lengths [Å] for 42% *en*/$FAPbBr_3$ at 293 K with estimated standard deviations in parentheses.

Label	Distances
Pb-Br	3.03200(10)
Pb-Br#1	3.03200(10)
Pb-Br#2	3.03200(10)
Pb-Br#3	3.03200(10)
Pb-Br#4	3.03200(10)
Pb-Br#5	3.03200(10)
Br-N#6	3.4921(13)
Br-N#7	3.4921(13)
Br-N#8	3.4921(13)
Br-N#9	3.4921(13)
Br-N#10	3.4921(13)
Br-N#4	3.4921(13)
Br-N#11	3.4921(13)
Br-N#12	3.4921(13)
C-N	1.299(3)
C-N#13	1.299(3)
C-N#14	1.299(3)
C-N#15	1.299(3)
C-N#16	1.299(3)
C-N#17	1.299(3)

Symmetry transformations used to generate equivalent atoms:

(1) x,y,z+1 (2) z,x,y (3) z+1,x,y (4) y,z,x (5) y,z+1,x (6) x,y,z-1 (7) x+1,y,z-1 (8) -x,-y+1,z-1 (9) -x+1,-y+1,z-1 (10) y,z-1,x (11) -y+1,z-1,-x (12) -y+1,z,-x (13) -x,-y+2,z (14) z-1,x+1,y (15) z-1,-x+1,-y+2 (16) y-1,z,x+1 (17) -y+1,z,-x+1 (18) x-1,y,z+1 (19) z,x,y+1

Table S21. Bond angles [°] for 42% *en*/$FAPbBr_3$ at 293 K with estimated standard deviations in parentheses.

Label	Angles
Br-Pb-Br#1	180
Br-Pb-Br#2	90
Br-Pb-Br#3	90
Br-Pb-Br#4	90
Br-Pb-Br#5	90
Br#1-Pb-Br#2	90
Br#1-Pb-Br#3	90
Br#1-Pb-Br#4	90
Br#1-Pb-Br#5	90
Br#2-Pb-Br#3	180
Br#2-Pb-Br#4	90
Br#2-Pb-Br#5	90
Br#3-Pb-Br#4	90
Br#3-Pb-Br#5	90
Br#4-Pb-Br#5	180
Pb#6-Br-Pb	180

Symmetry transformations used to generate equivalent atoms:

(1) x,y,z+1 (2) z,x,y (3) z+1,x,y (4) y,z,x (5) y,z+1,x (6) x,y,z-1 (7) x+1,y,z-1 (8) -x,-y+1,z-1 (9) -x+1,-y+1,z-1 (10) y,z-1,x (11) -y+1,z-1,-x (12) -y+1,z,-x (13) -x,-y+2,z (14) z-1,x+1,y (15) z-1,-x+1,-y+2 (16) y-1,z,x+1 (17) -y+1,z,-x+1 (18) x-1,y,z+1 (19) z,x,y+1

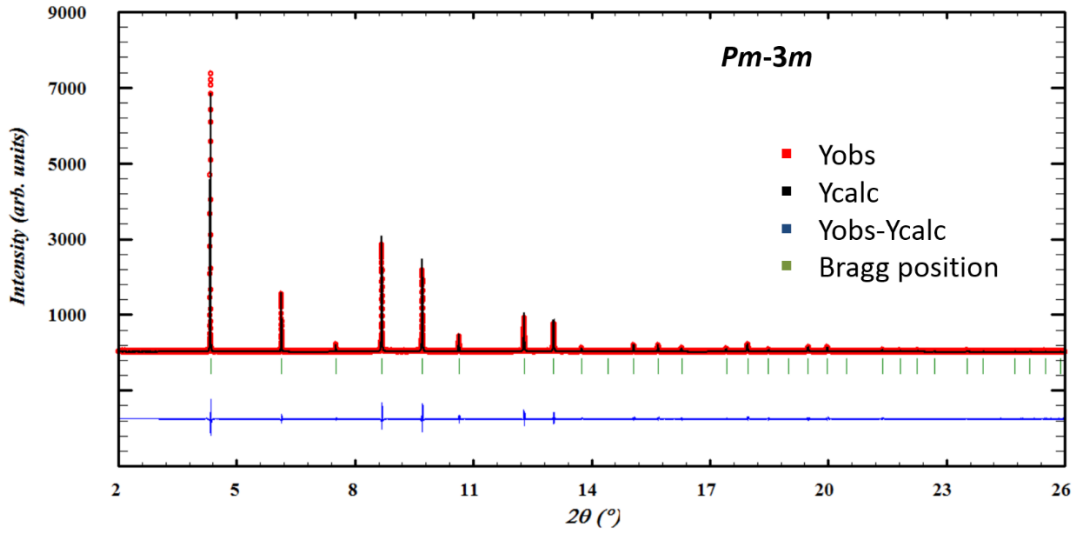

Figure S2. Observed and calculated diffraction profiles from the Le Bail fitting method of the RT diffraction pattern for the 29% *en*/$FAPbBr_3$ material, modeled with the cubic *Pm*-3*m* space group.

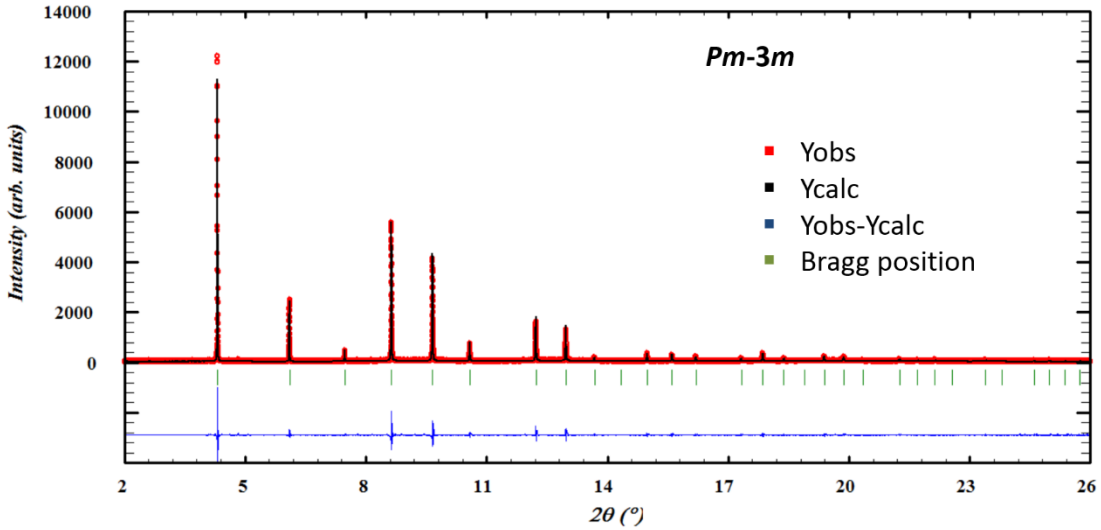

Figure S3. Observed and calculated diffraction profiles from the Le Bail fitting method of the RT diffraction pattern for the 44% *en*/$FAPbBr_3$ material, modeled with the cubic *Pm*-3*m* space group.

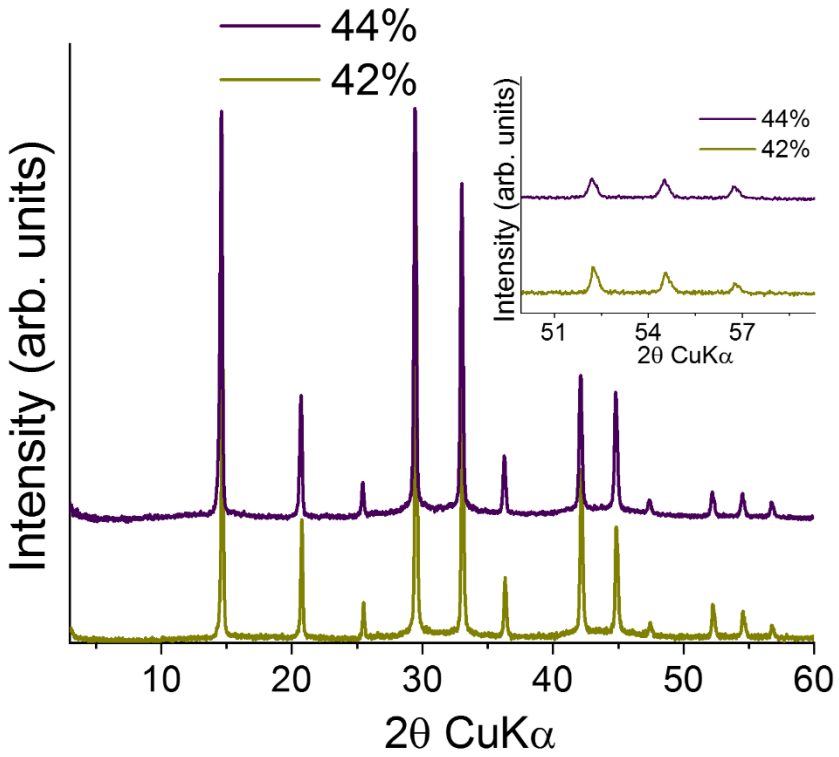

Figure S4. Comparison of the experimental PXRD patterns of compounds 42% *en*/$FAPbBr_3$ and 44% *en*/$FAPbBr_3$. The inset figure shows the small shift of the pattern to lower 2θ values for the 44% *en* sample.

Table S22. Correlation between refinement occupancy parameters for Pb and Br atoms for the single crystal structures of the hollow compounds.

$FAPbBr_3$ + *en*%	**Pb occupancy**	**Br occupancy**
0	1	1
18	0.9194	1
29	0.8256	0.9986
42	0.8051	0.9956

EDS measurements

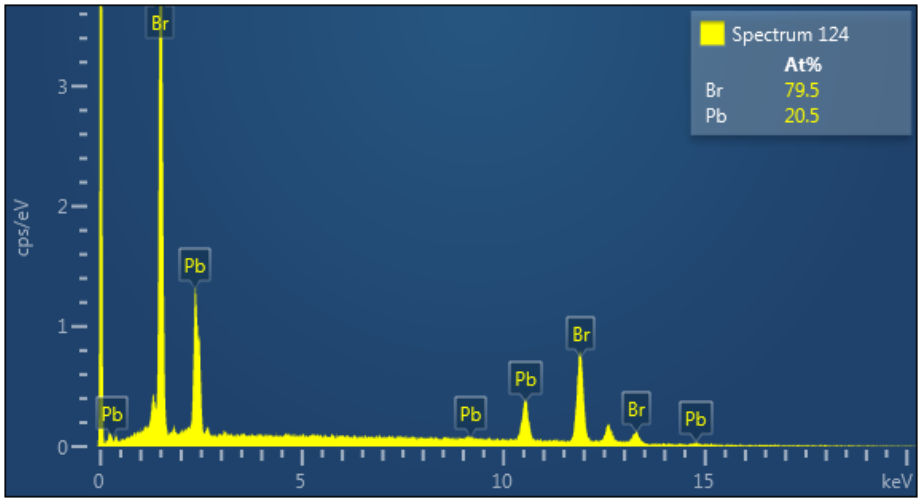

Figure S5. Representative EDS spectrum of 42% *en*/$FAPbBr_3$ compound. The Br:Pb ratio is 3.9:1, much higher than 3:1 which is the ratio for the pristine 3D $FAPbBr_3$.

Thermogravimetric analysis

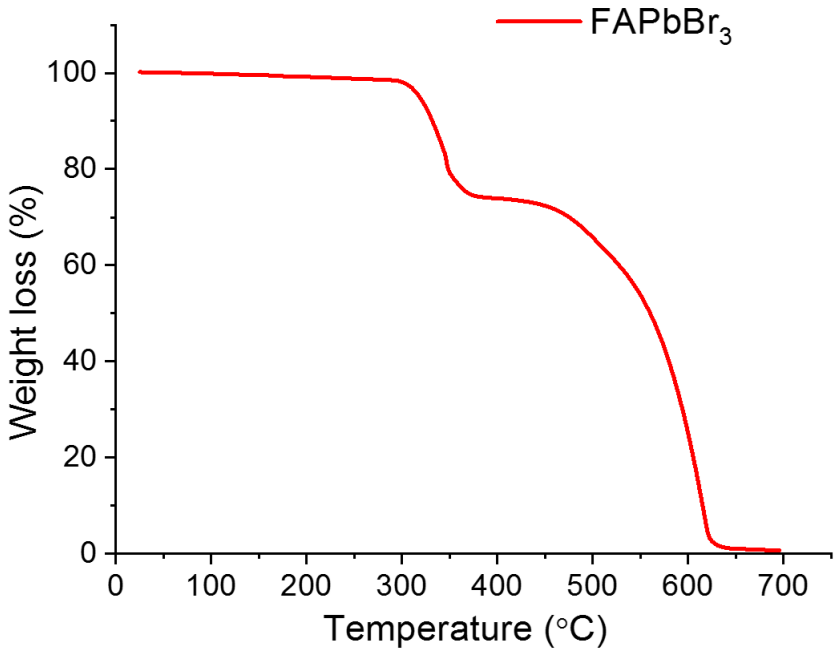

Figure S6. TGA curve for the pristine α-$FAPbBr_3$ compound recorded under helium flow with a heating rate of 8 deg/min.

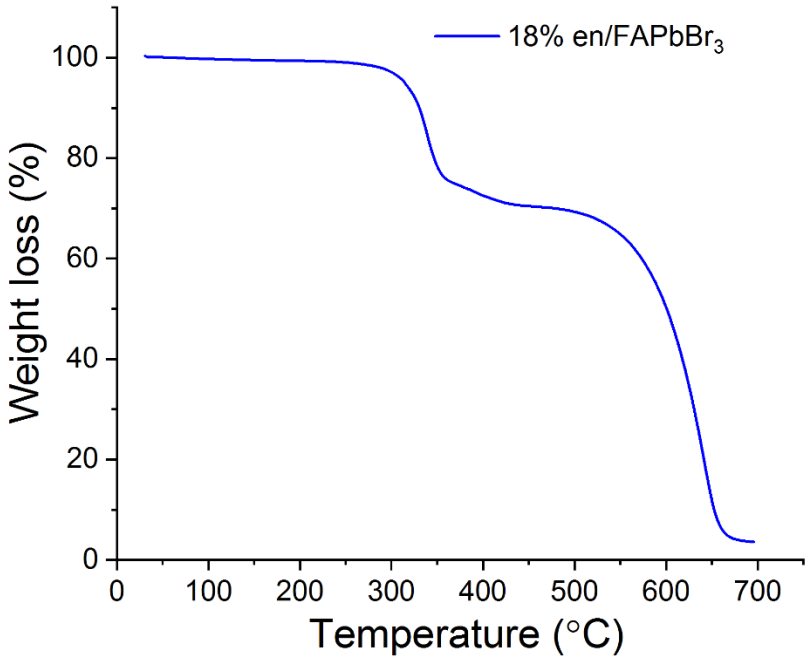

Figure S7. TGA curve for the 18% *en* compound recorded under helium flow with a heating rate of 8 deg/min.

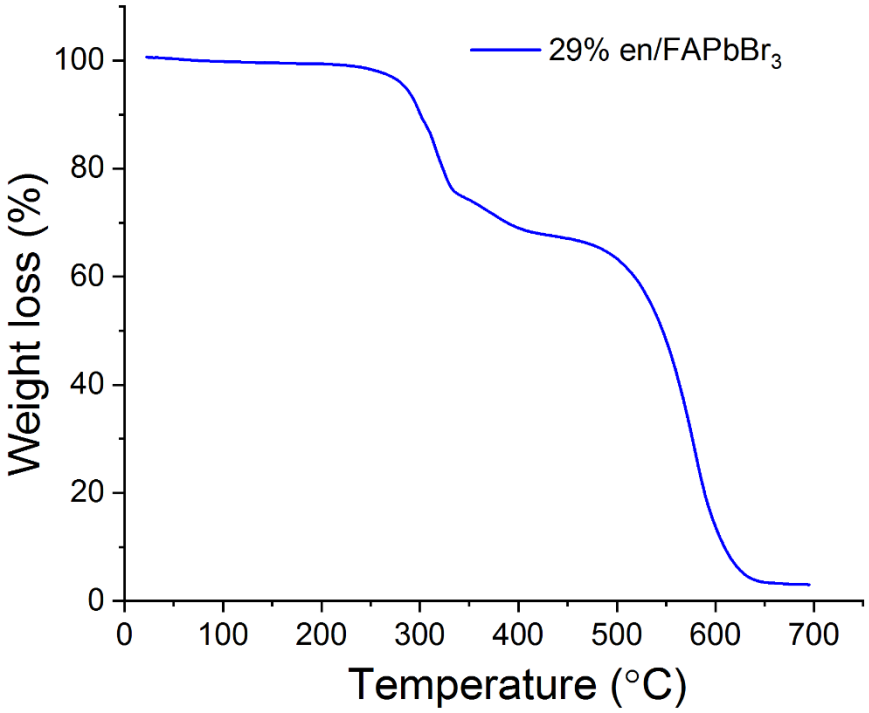

Figure S8. TGA curve for the 29% *en* compound recorded under helium flow with a heating rate of 8 deg/min.

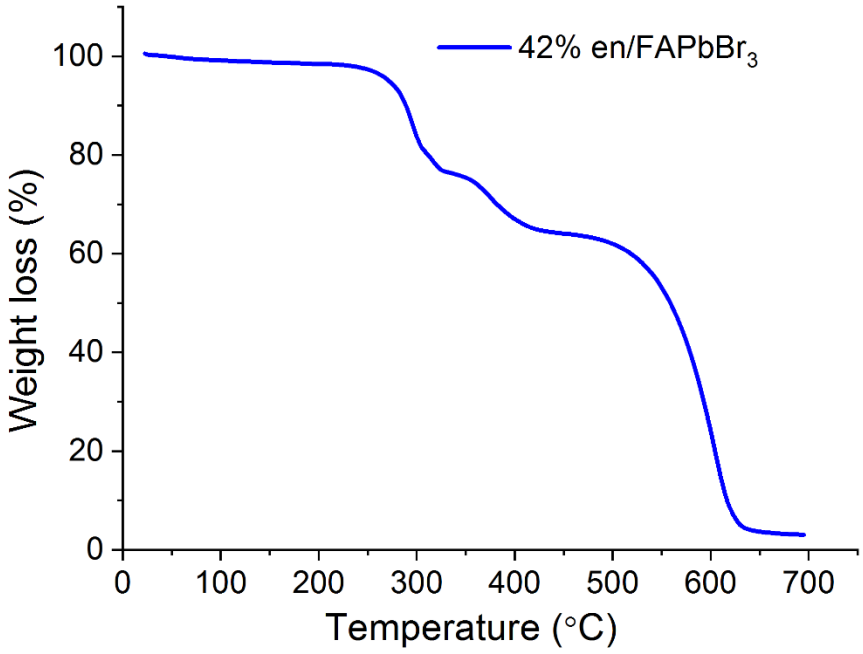

Figure S9. TGA curve for the 42% *en* compound recorded under helium flow with a heating rate of 8 deg/min.

Table S23. Correlation between the % weight loss of the organic and inorganic part of the $(FA)_{1-x}(en)_x(Pb)_{1-0.7x}(Br)_{3-0.4x}$ compounds.

$FAPbBr_3$ + *en*%	**$FABr+enBr_2$ loss%**	**$PbBr_2$ loss%**
0	25.1	73.4
18	29.1	66.3
29	31.6	64.4
42	36.2	60.5

^{1}H-NMR Spectroscopy

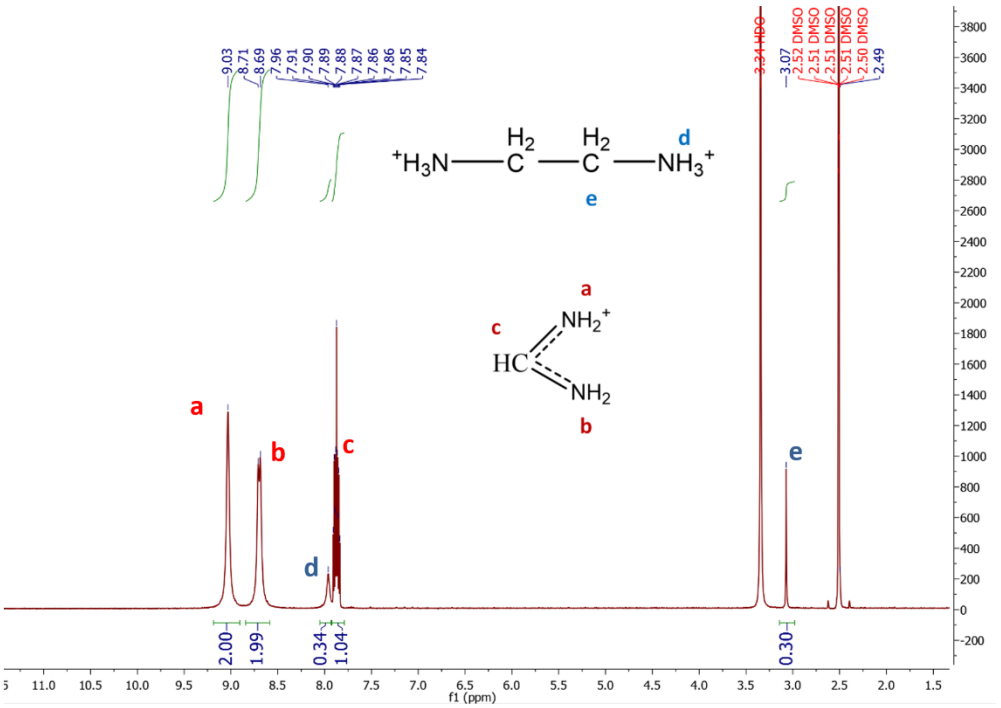

Figure S10. ^{1}H NMR spectrum of the 7% *en*/FAPbBr$_3$ compound in DMSO-d_6.

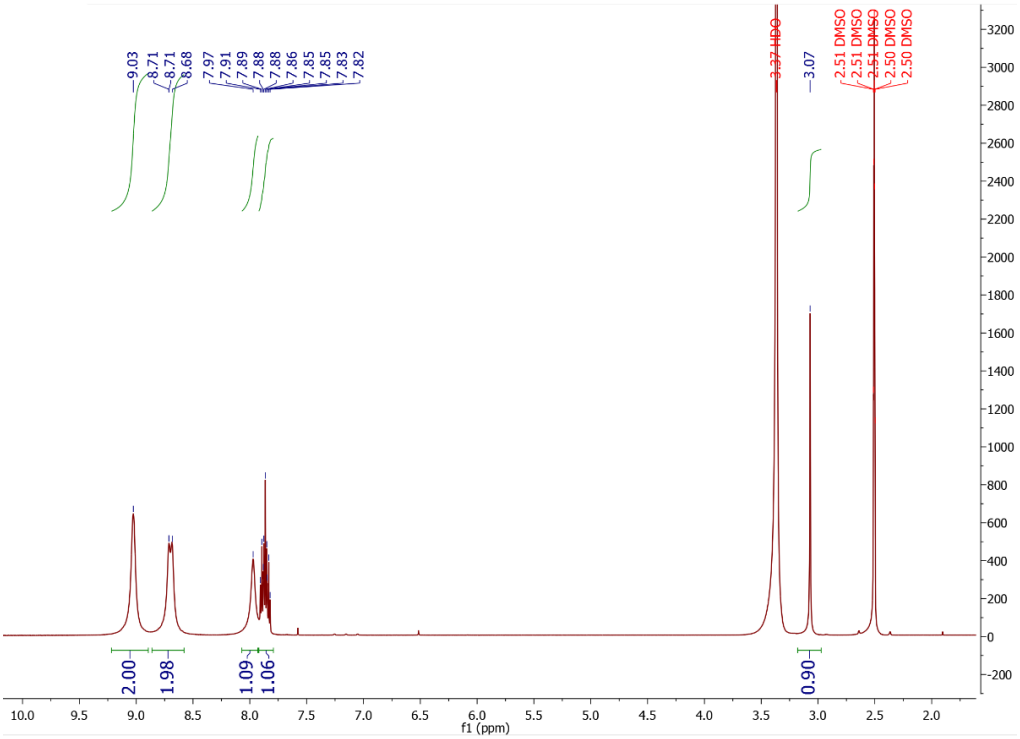

Figure S11. ^{1}H NMR spectrum of the 18% *en*/FAPbBr$_3$ compound in DMSO-d_6.

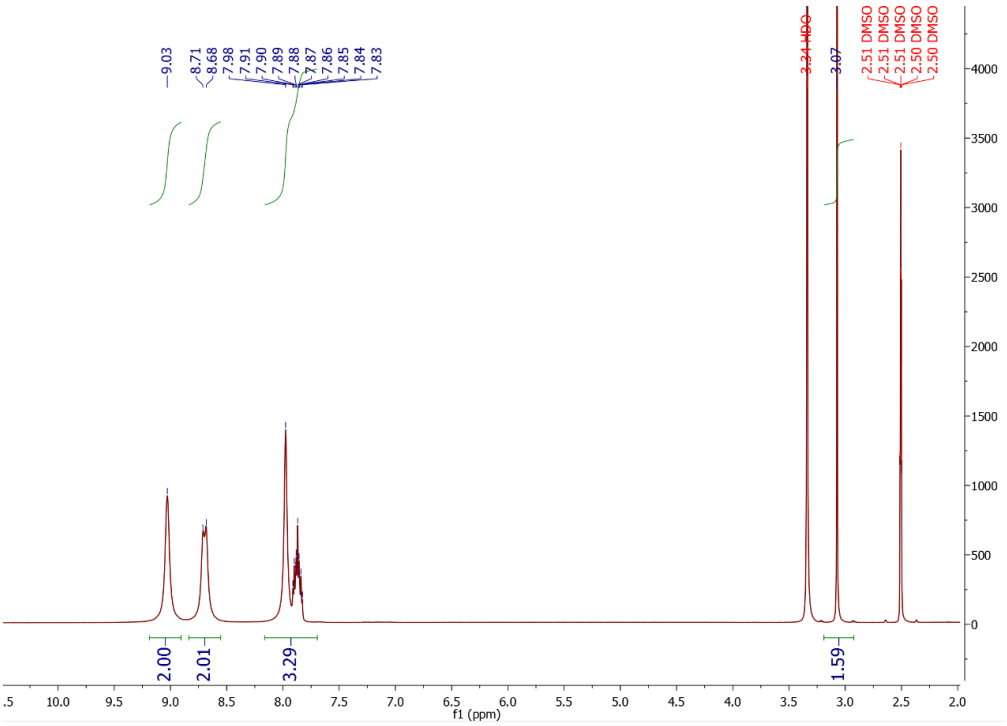

Figure S12. ^{1}H NMR spectrum of the 29% *en*/FAPbBr$_3$ compound in DMSO-d_6.

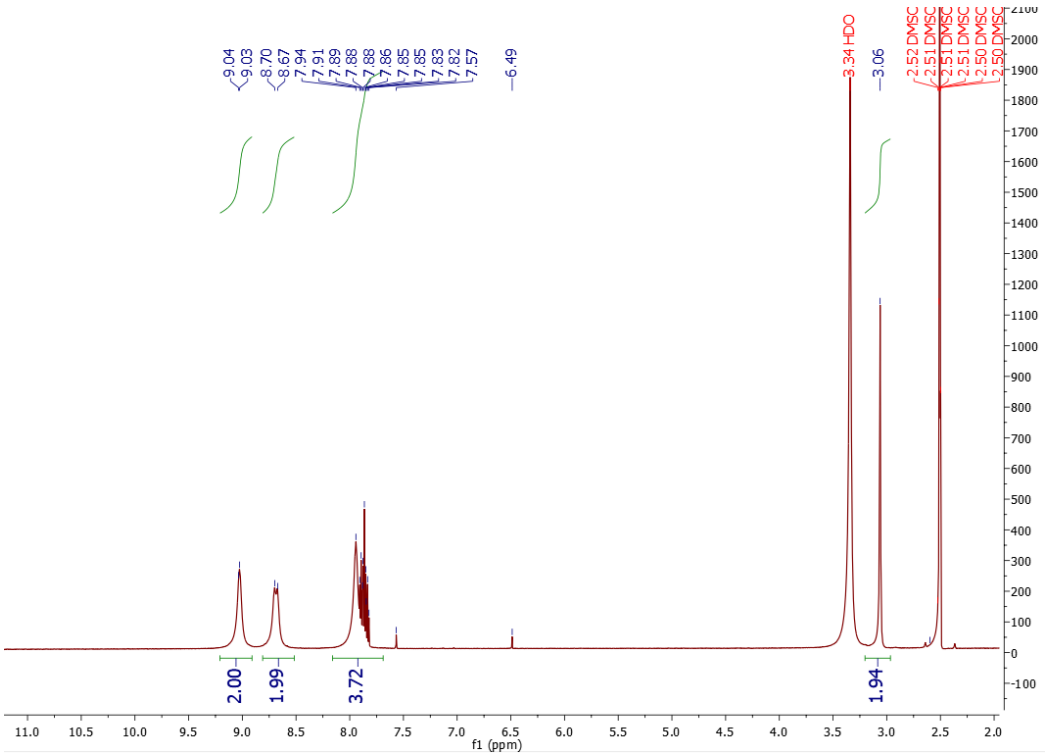

Figure S13. ^{1}H NMR spectrum of the 33% *en*/FAPbBr$_3$ compound in DMSO-d_6.

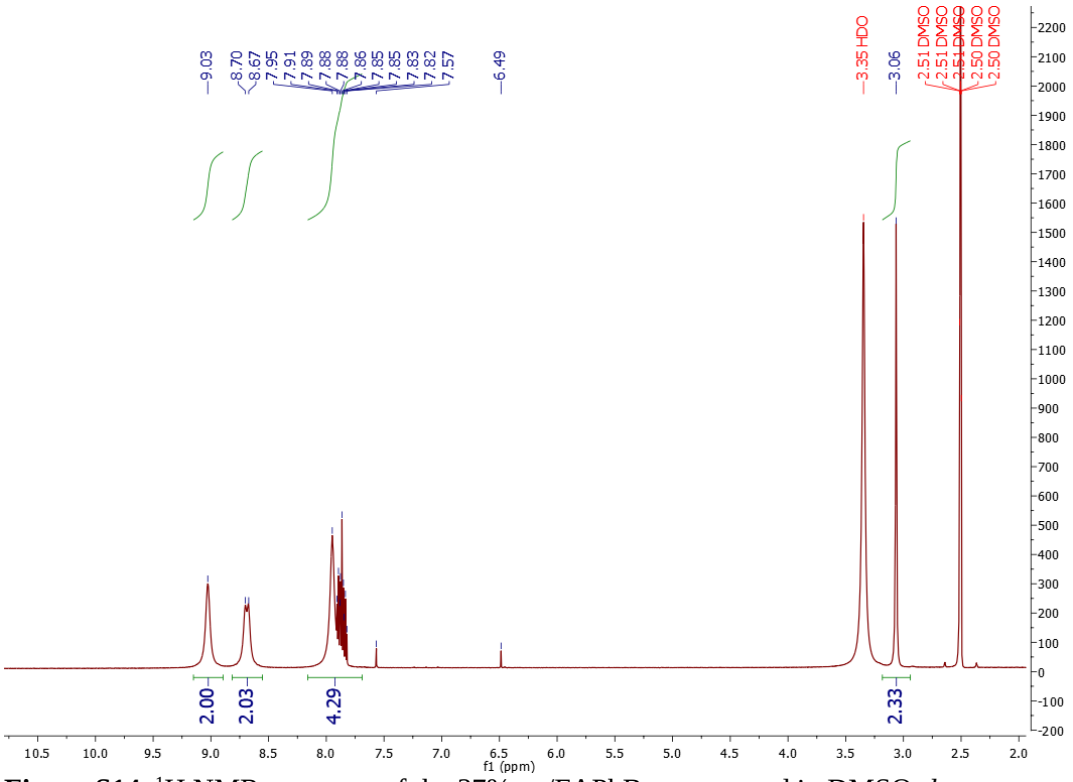

Figure S14. ^{1}H NMR spectrum of the 37% *en*/FAPbBr$_3$ compound in DMSO-d_6.

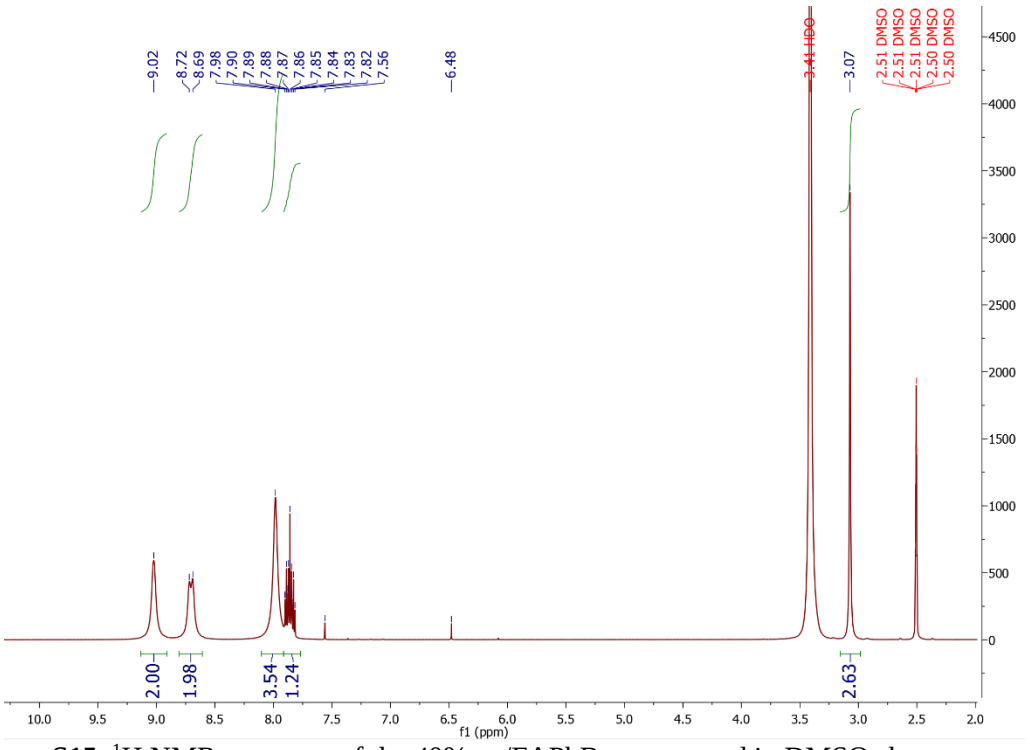

Figure S15. ^{1}H NMR spectrum of the 40% *en*/FAPbBr$_3$ compound in DMSO-d_6.

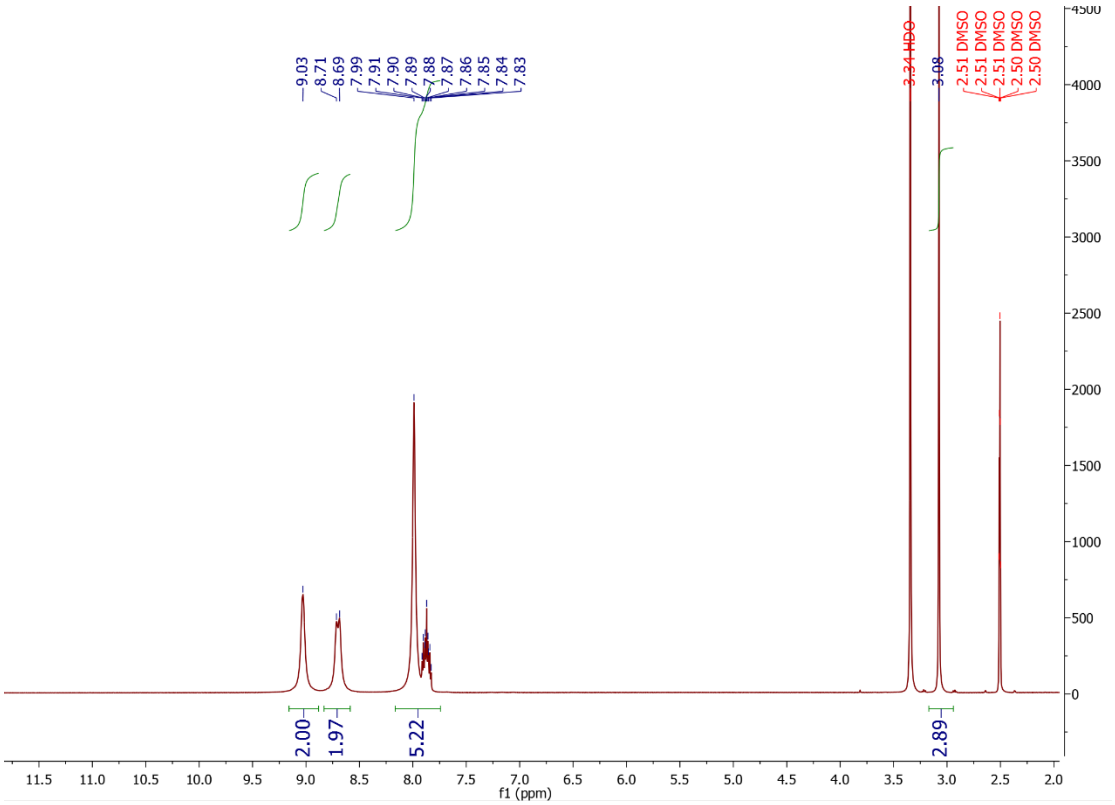

Figure S16. ^{1}H NMR spectrum of the 42% *en*/FAPbBr$_3$ compound in DMSO-d_6.

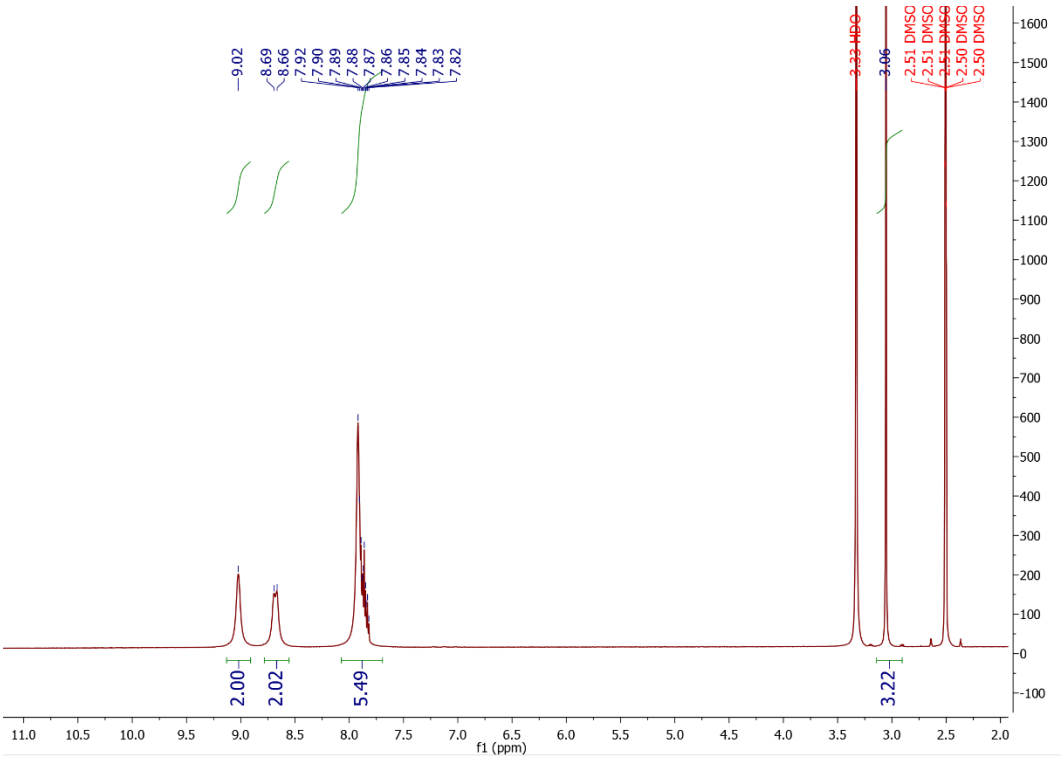

Figure S17. ^{1}H NMR spectrum of the 44% *en*/FAPbBr$_3$ compound in DMSO-d_6.

Crystal density measurements

Table S24. Comparison of calculated crystal density based on the prosposed crystal formula $(FA)_{1-x}(en)_x(Pb)_{1-0.7x}(Br)_{3-0.4x}$ and the experimentally recorded ones based on single crystal XRD studies and the ones determined usng a commercial pycnometer. The experimental crystal density values for the pristine material agree perfectly. The 1% difference among the XRD determined value and the theoritical based one is ascribed to the fact that the single crystal structure is refined without the addition of the 5 hydrogen atoms in the FA linker, which will increase the molecular weight.

$FAPbBr_3$ + *en*%	**Calcu. crystal density (g cm^{-3}) Based on formula**	**Exp. crystal density (g cm^{-3}) Based on pycnometry**	**Exp. crystal density (g cm^{-3}) Based on XRD studies**
0	3.8087	3.8116(2)	3.7574(2)
7	3.6967	3.7412(2)	-
18	3.5263	3.7185(2)	3.5729(6)
29	3.3762	3.5737(2)	3.3631(1)
42	3.1735	3.4657(2)	3.3177(6)

High resolution PXRD measurements

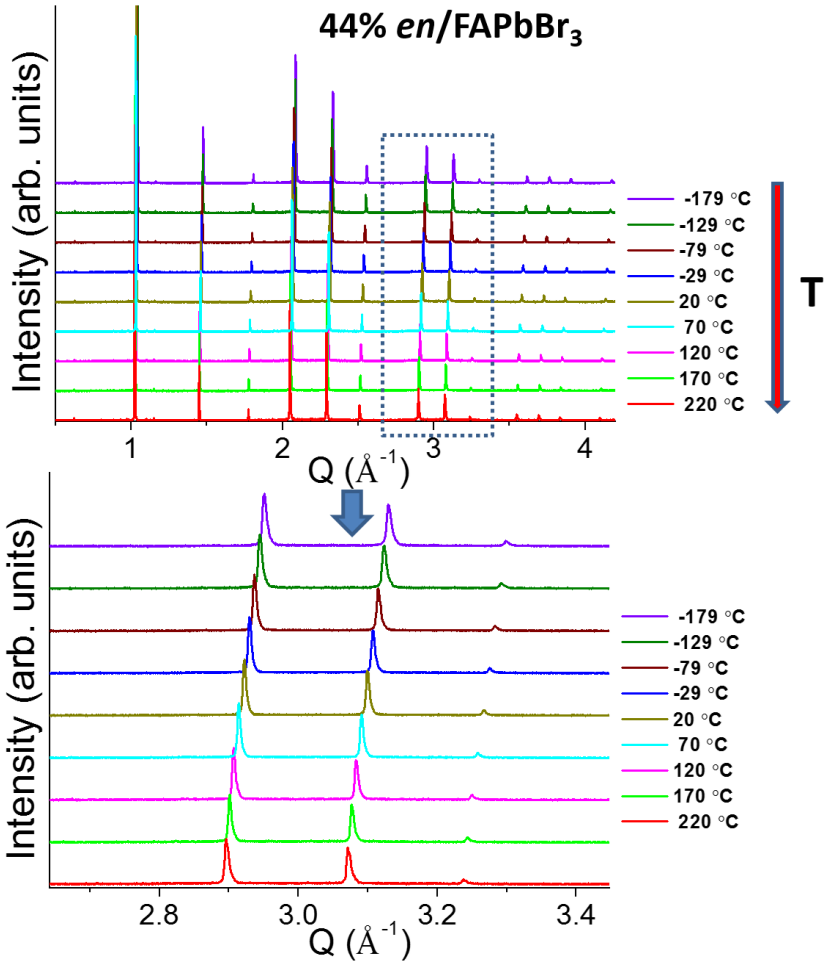

Figure S18. High resolution variable temperature PXRD patterns for the 44% *en*/$FAPbBr_3$, consisting of one heating cycle. The highlighted area is enlarged to show better the shift of the diffraction peaks to lower Q values with increasing temperature, indicative of lattice thermal expansion. There is no appearance of additional diffraction peaks, revealing the absence of temperature dependent structural phase transitions.

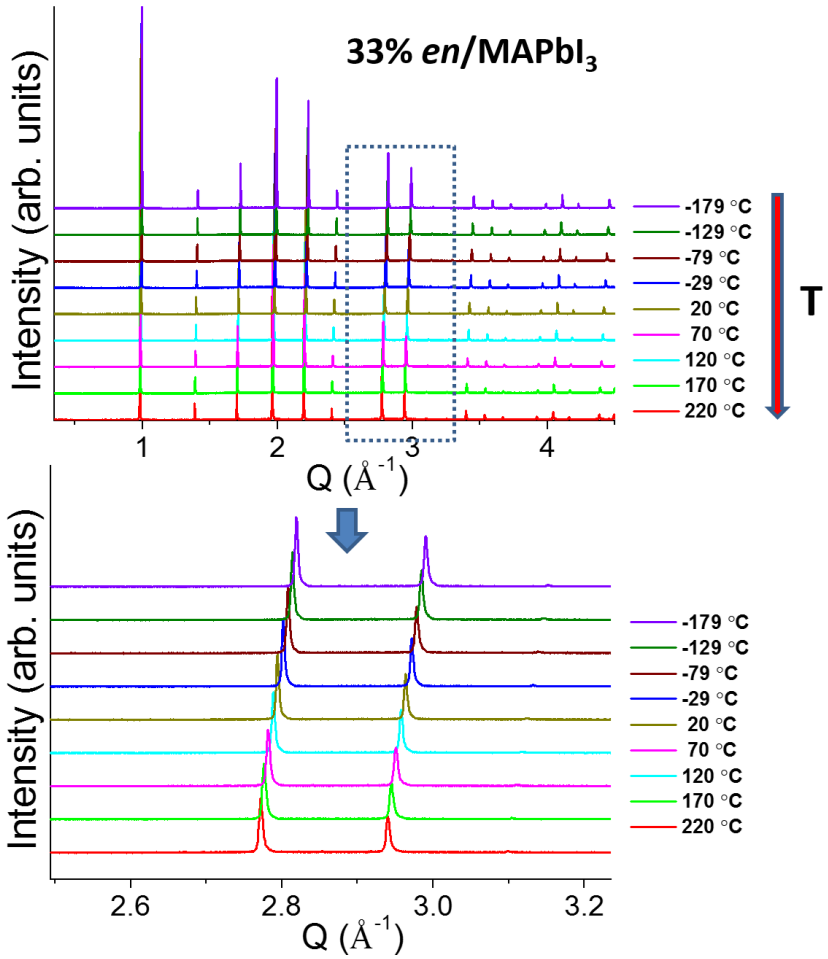

Figure S19. High resolution variable temperature PXRD patterns for the 33% *en*/$MAPbI_3$, consisting of one heating cycle. The highlighted area is enlarged to show better the shift of the diffraction peaks to lower Q values with increasing temperature, indicative of lattice thermal expansion. There is no appearance of additional diffraction peaks, revealing the absence of temperature dependent structural phase transitions.

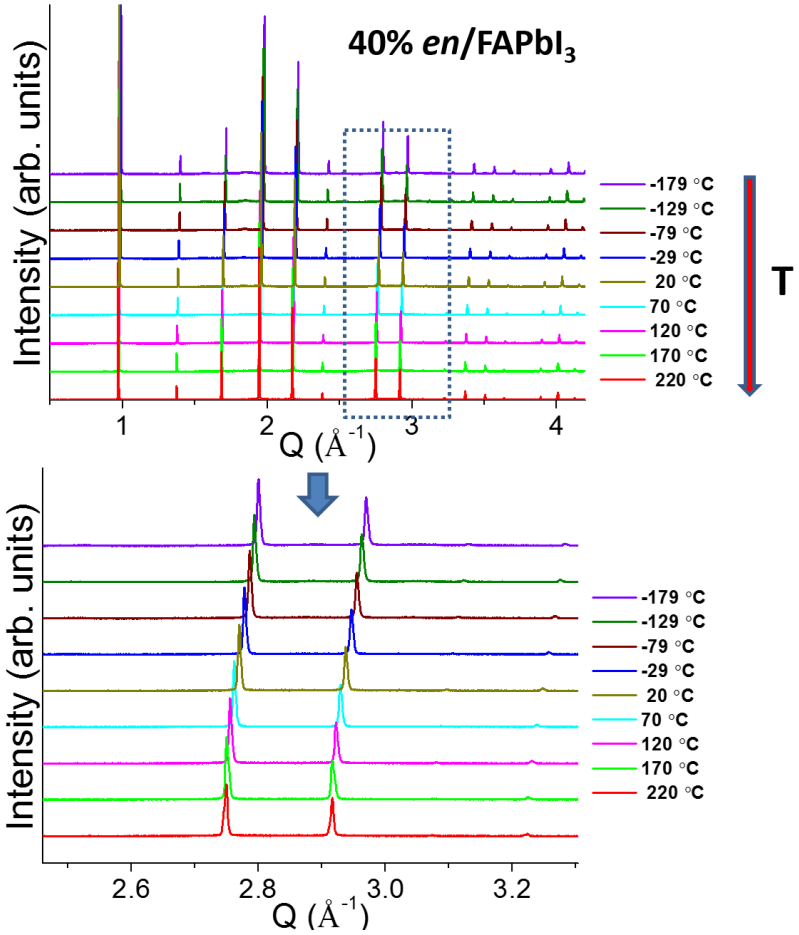

Figure S20. High resolution variable temperature PXRD patterns for the 40% *en*/$FAPbI_3$, consisting of one heating cycle. The highlighted area is enlarged to show better the shift of the diffraction peaks to lower Q values with increasing temperature, indicative of lattice thermal expansion. There is no appearance of additional diffraction peaks, revealing the absence of temperature dependent structural phase transitions.

ssNMR measurements

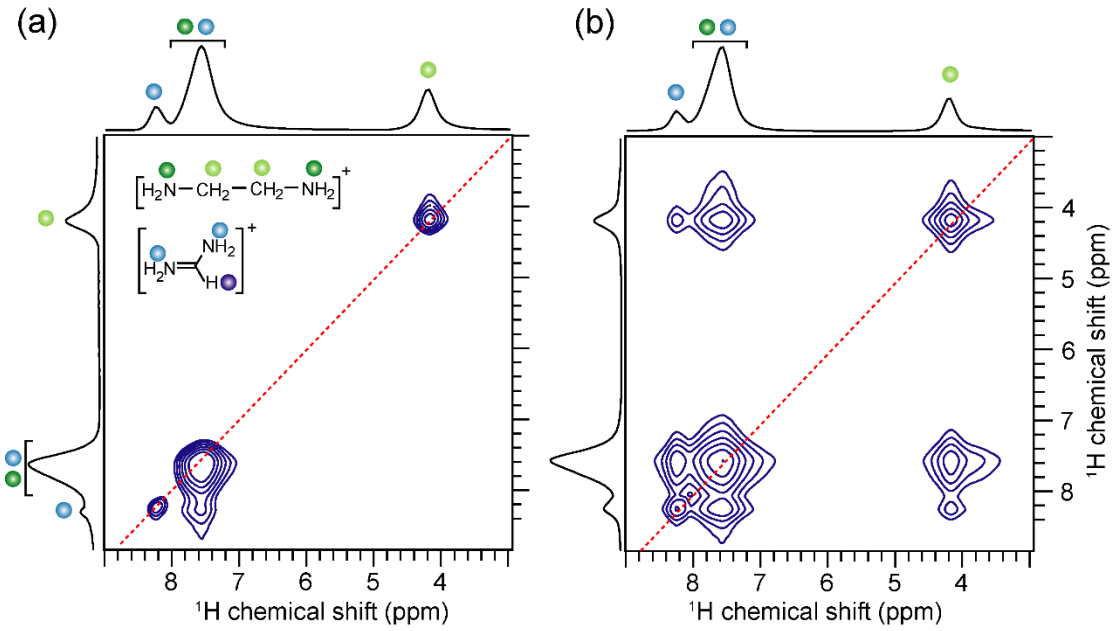

Figure S21. Solid-state 2D ^{1}H-^{1}H SQ-SQ correlation NMR spectra of 41% *en*/FAPbBr$_3$ using (a) 20 ms and (b) 100 ms spin diffusion mixing time.

Photoluminescence measurements

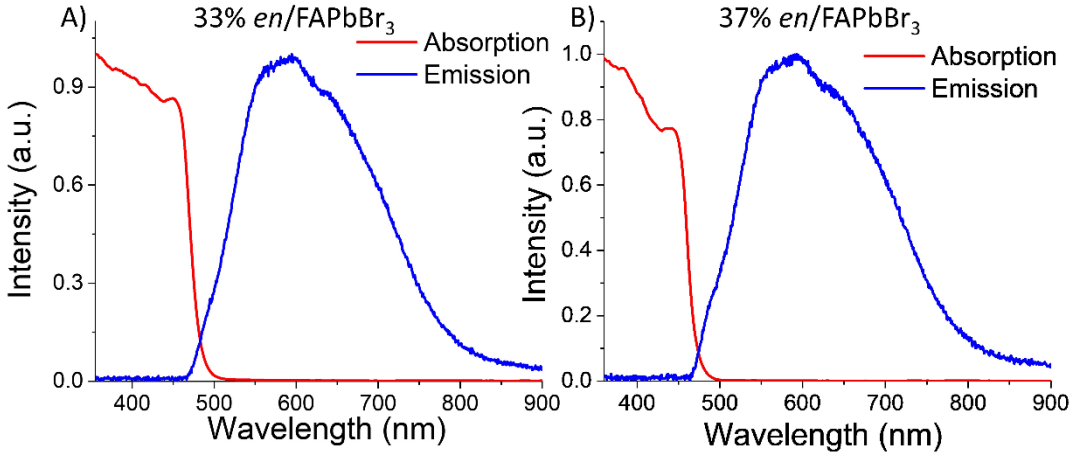

Figure S22. Recorded absorption and emission spectra of A) 33% and B) 37% en/FAPbBr$_3$ compounds at RT.

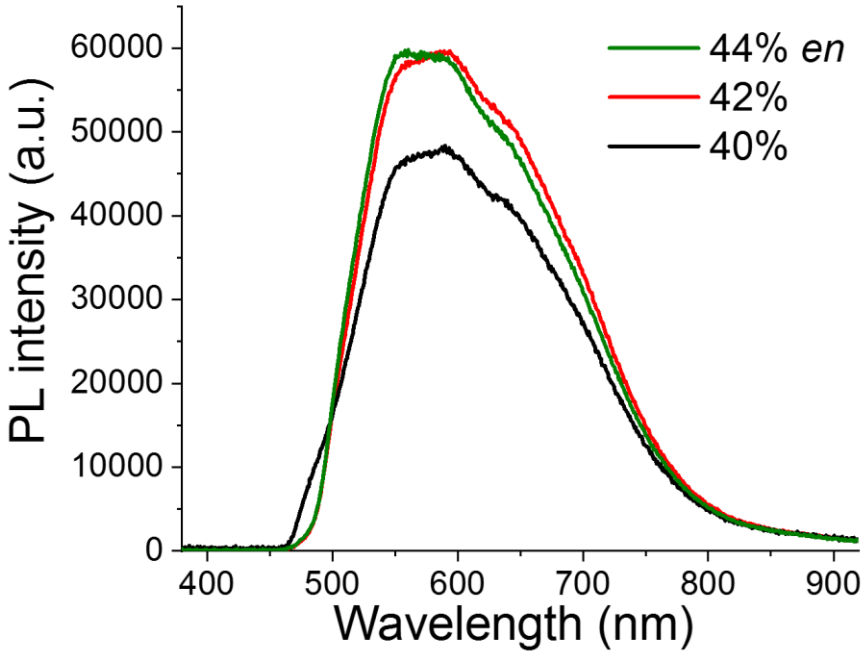

Figure S23. RT photoluminescence spectra of 40%, 42% and 44% *en*/$FAPbBr_3$ compounds.

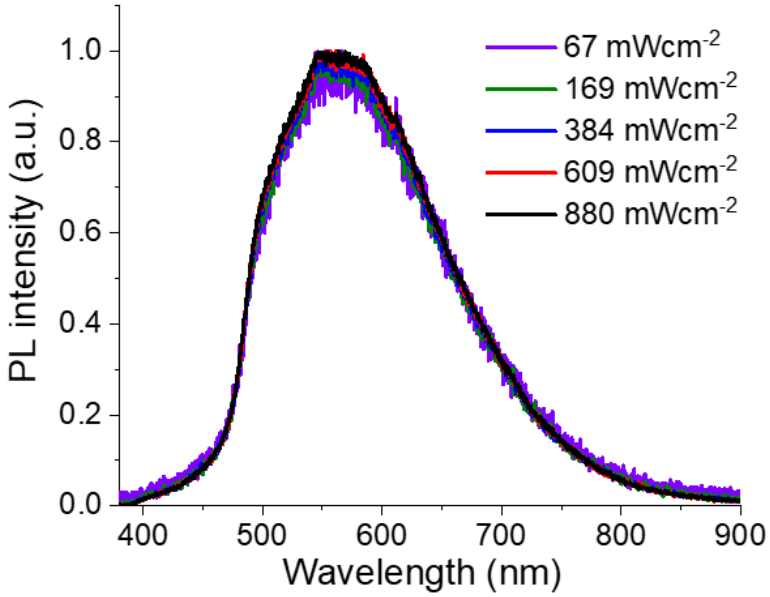

Figure S24. Normalized variable power PL emission spectra of 42% *en*/$FAPbBr_3$ at 295K. PL intensity at each excitation power is divided by the excitation flux.

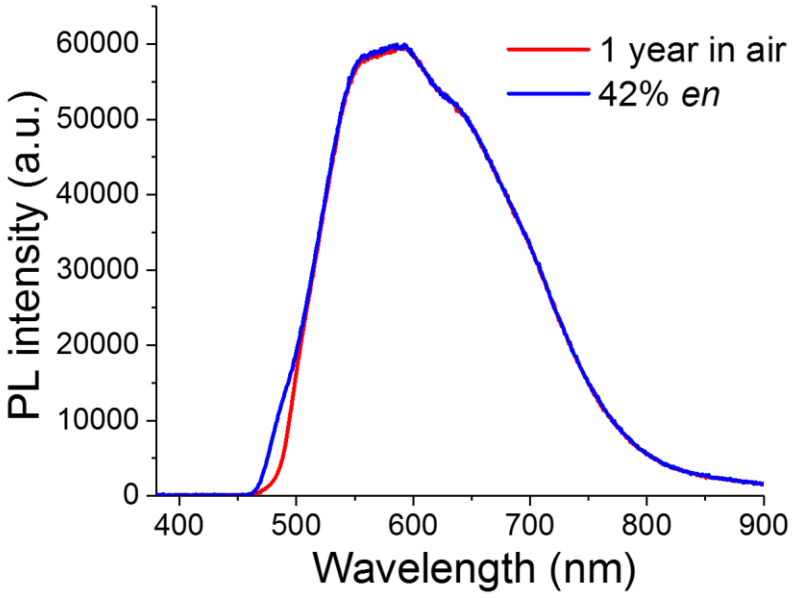

Figure S25. Comparison of the photoluminescence spectra of the fresh 42% *en*/$FAPbBr_3$ sample and after 1 year exposure to air.

PYSA measurements

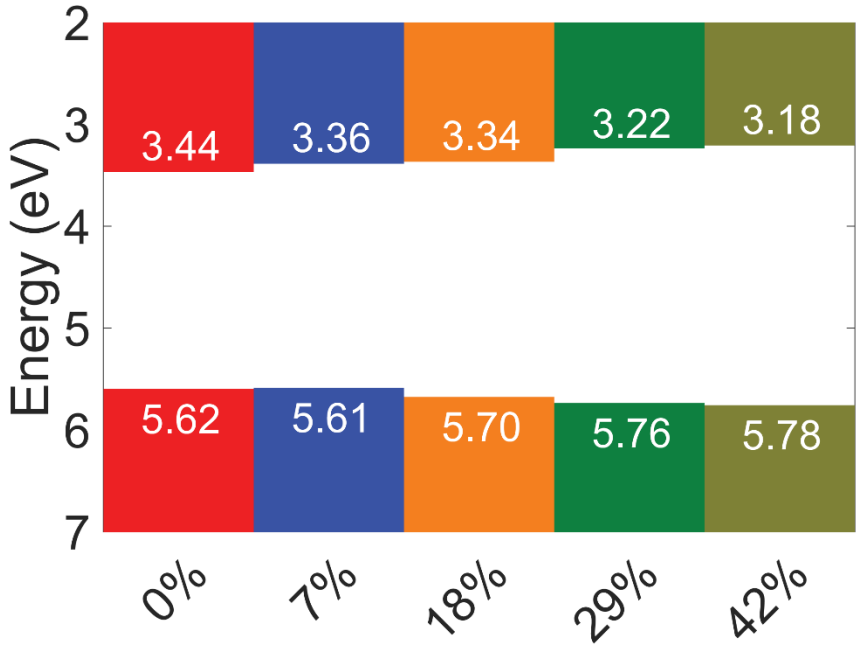

Figure S26. Comparative band energy diagram for the pristine $FAPbBr_3$ crystals, and the hollow ones for 7%, 18%, 29% and 42% *en* amount.

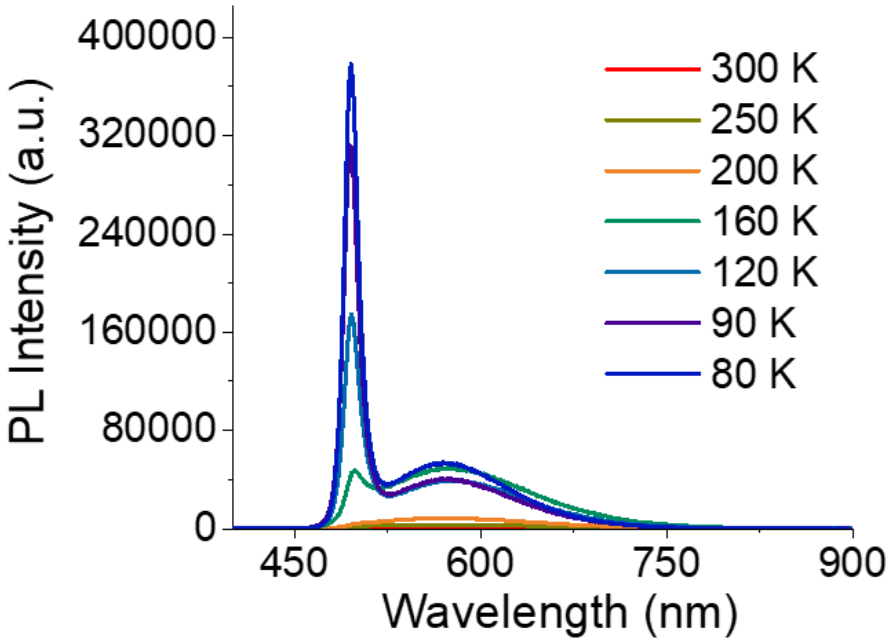

Figure S27. Low temperature PL emission spectra for compound 42% *en*/$FAPbBr_3$.

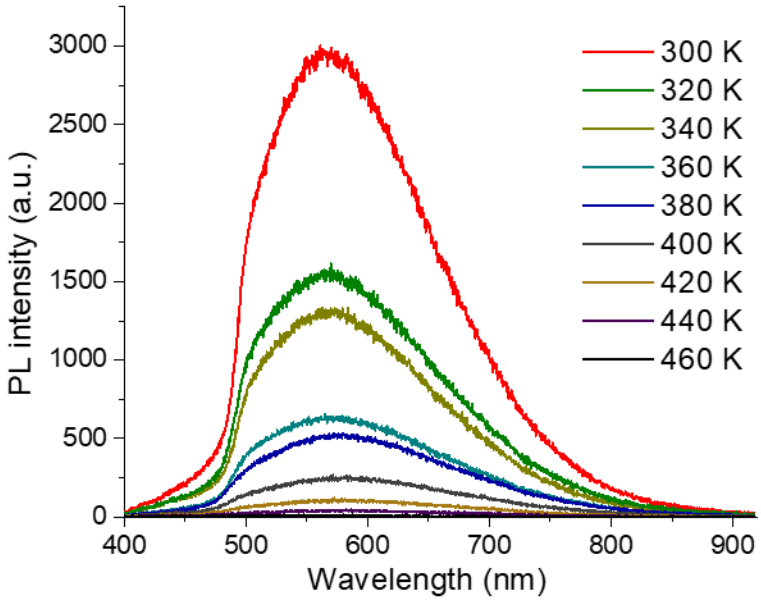

Figure S28. High temperature PL emission spectra for compound 42% *en*/$FAPbBr_3$.

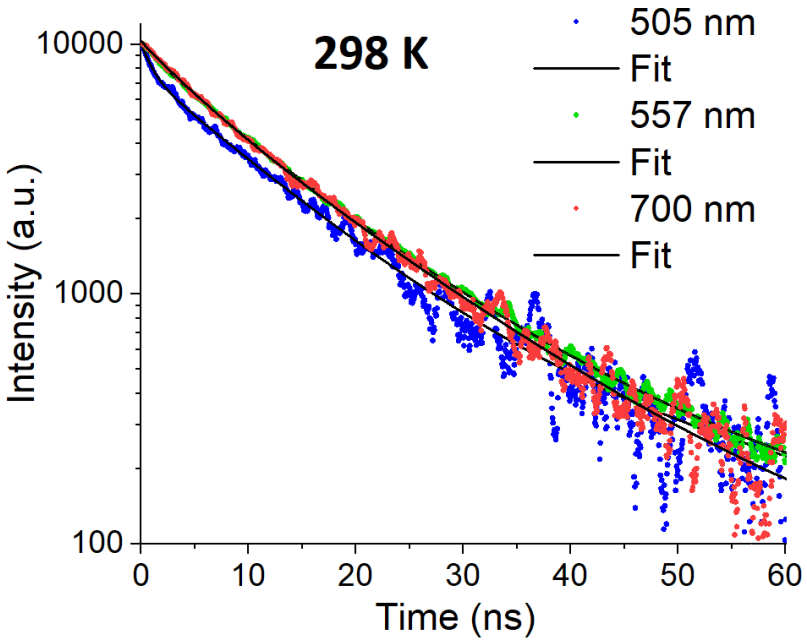

Figure S29. Time-resolved photoluminescence decay at 298K, comparing the lifetimes for the FE (505nm) and STE (557 nm and 700 nm (end of STE)).

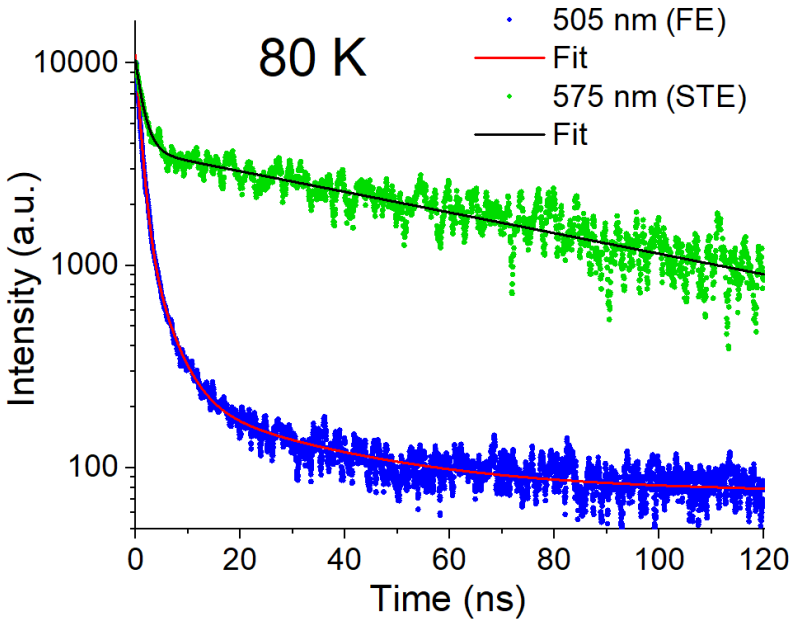

Figure S30. Time-resolved photoluminescence decay at 80K, comparing the lifetimes for the FE (505nm) and STE (575 nm).

XRF measurements

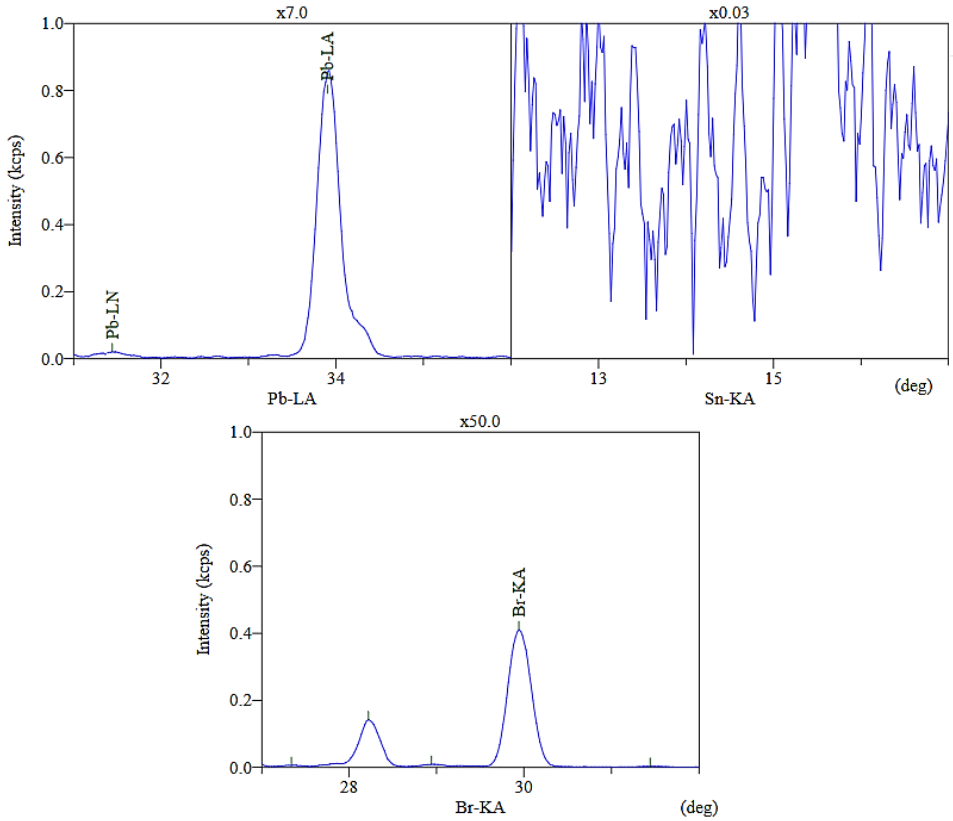

Figure S31. Pb, Sn, and Br XRF spectra of 42% *en*/FAPbBr$_3$ perovskite.

4. References

1. Spanopoulos, I.; Ke, W.; Stoumpos, C. C.; Schueller, E. C.; Kontsevoi, O. Y.; Seshadri, R.; Kanatzidis, M. G., Unraveling the Chemical Nature of the 3D "Hollow" Hybrid Halide Perovskites, *J. Am. Chem. Soc.* **2018,** *140*, 5728-5742.
2. Petrícek, V.; Dušek, M.; Palatinus, L., Crystallographic computing system JANA2006: General features, *Z. Kristallogr.* **2014,** *229*, 345-352.
3. Toby, B., CMPR - a powder diffraction toolkit, *J. Appl. Crystallogr.* **2005,** *38*, 1040-1041.
4. Toby, B., CMPR - a powder diffraction toolkit, *J. Appl. Crystallogr.* **2005,** *38*, 1040-1041.
5. Hammersley, A. P., FIT2D: An Introduction and Overview, *ESRF Internal Report* **1997**, ESRF97HA02T.
6. Hammersley, A. P.; Svensson, S. O.; Hanfland, M.; Fitch, A. N.; Hausermann, D., Two-dimensional detector software: From real detector to idealised image or two-theta scan, *High Pressure Res* **1996,** *14*, 235-248.
7. Juhas, P.; Davis, T.; Farrow, C. L.; Billinge, S. J. L., PDFgetX3: a rapid and highly automatable program for processing powder diffraction data into total scattering pair distribution functions, *J. Appl. Crystallogr.* **2013,** *46*, 560-566.

8. Farrow, C. L.; Juhas, P.; Liu, J. W.; Bryndin, D.; Božin, E. S.; Bloch, J.; Proffen, T.; Billinge, S. J. L., PDFfit2 and PDFgui: computer programs for studying nanostructure in crystals, *J. Phys.: Condens. Matter* **2007,** *19*, 335219.
9. Gate, L. F., Comparison of the Photon Diffusion Model and Kubelka-Munk Equation with the Exact Solution of the Radiative Transport Equation, *Appl. Opt.* **1974,** *13*, 236-238.
10. Prochowicz, D.; Franckevicius, M.; Cieslak, A. M.; Zakeeruddin, S. M.; Gratzel, M.; Lewinski, J., Mechanosynthesis of the hybrid perovskite CH3NH3PbI3: characterization and the corresponding solar cell efficiency, *J. Mater. Chem. A* **2015,** *3*, 20772-20777.
11. Stoumpos, C. C.; Malliakas, C. D.; Kanatzidis, M. G., Semiconducting Tin and Lead Iodide Perovskites with Organic Cations: Phase Transitions, High Mobilities, and Near-Infrared Photoluminescent Properties, *Inorg. Chem.* **2013,** *52*, 9019-9038.